NUMERICAL FLUID DYNAMICS AND COMBUSTION STUDY OF EMULSIFIED CANOLA OIL DROPLETS IN A SWIRL PROMOTED COMBUSTION CHAMBER

A Dissertation

by

QIBO LI

Submitted to the Office of Graduate and Professional Studies of
Texas A&M University
in partial fulfillment of the requirements for the degree of

DOCTOR OF PHILOSOPHY

Chair of Committee,	Jorge Alvarado
Committee Members,	Kalyan Annamalai
	Hamn-Ching Chen
	Othon Rediniotis
Head of Department,	Andreas Polycarpou

December 2015

Major Subject: Mechanical Engineering

ABSTRACT

Recently, straight vegetable oils (SVO) have been considered as combustion fuels due to their relatively high heating value and negligible content of sulfur and nitrogen, which is beneficial from the combustion point of view. However, the high viscosity of SVO has hindered their ability and applicability in combustion systems. In order to reduce the effect of high viscosity of SVO, methanol has been used as an additive to reduce its apparent viscosity. Furthermore, a twin-fluid atomizer has been used to form and dispense a fine spray of SVO to ensure complete combustion. To enhance the combustion characteristics of SVO, a multiple vane swirler has been adapted and used inside a conventional combustion chamber to enhance the mixing between the emulsified SVO fuel blend and the surrounding flowing air. However, the effects of vortex generation and droplet distribution on combustion emissions for SVO biofuels in a combustion chamber still are not well understood.

Recent studies have revealed that large eddy simulation (LES) as CFD technique is capable of capturing the unstable features of two-phase swirling flows. This technique provides an effective and economical approach to study the behavior of air and coupled with the other model to predict the fuel spray droplets and combustion characteristics in a conventional combustion chamber. In this study, blends of canola oil and methanol

have been selected as emulsified fuels for simulation purposes. To fully understand the effects of swirl number and equivalence ratio on the distribution of emulsified canola oil droplets, the discrete phase model (DPM), stochastic model and TAB model have been adopted to simulate SVO blend droplets. Furthermore, the Eddy-Dissipation model has been used to understand the effects of swirl number and equivalence ratio on combustion characteristics of SVO. A robust and stable numerical algorithm has been selected and validated. The interaction between the swirling air flow and fuel droplets have been simulated using LES by considering two swirl numbers. The effects of swirl number and equivalence ratio on droplet size distribution and combustion characteristics in the combustion chamber have been considered and evaluated correspondingly. Results reveal that turbulent flow, fuel blend droplet distribution, and combustion characteristics are affected by the swirl number significantly. Moreover, the simulation results have the same trend as the experimental work, but the error of simulation depends on the intensity of turbulence.

DEDICATION

This dissertation is dedicated to my family, Dr. Jiding Li, Mrs. Jing Han, Mr. Fu Han, Mr. Yimeng Hu, Mrs. Qiao Shu, and Mrs. Xiaodan Hu, for their love, guidance, encouragement and continuous support throughout my vital educational years. This work would not have been possible without their blessings.

ACKNOWLEDGEMENTS

I would like to offer my sincere gratitude to several people who made this dissertation possible. First, I wish to thank my committee chair, Dr. Jorge L. Alvarado, for his guidance and mentorship. He has always been extremely helpful, and has generously shared his knowledge with me throughout the numerous discussions we had during the course of this research work. I would also like to thank the committee members for their kind assistance: Dr. Kalyan Annamalai, Dr. Hamn-Ching Chen, Dr. Waruna Kulatilaka and Dr. Othon Rediniotis.

In addition, I would like to thank my fellow members of Dr. Alvarado's research team: Shreyas Bhimani, Gautam Sandesh, Hyunseok Nam, for all their contributions of combustion experiments; Chun-Wei Yao, Taolue Zhang, and Minsuk Kong, for their wholehearted support.

In closing, I would like to thank my parents for their encouragement and the unconditional love they have instilled in me right from the time when I was a little child. Furthermore, I wish to thank my lovely wife, Xiaodan Hu, for inspiring me to make the necessary effort to bring this dissertation to fruition.

TABLE OF CONTENTS

Page

LIST OF FIGURES

FIGURE Page

LIST OF TABLES

TABLE Page

1. INTRODUCTION

In the past several decades, the tremendous demand for energy has led to high costs of traditional or conventional fossil fuels, such as oil, coal, and natural gas. This has results in greater pollutant emissions generated during combustion process of fuels. In recent years, researchers have shown renewed interest in development and use of alternative fuels such a biodiesel and other fuels derived from biomass. According to the latest data of the International Energy Agency (IEA) as shown in Fig. 1 [1], the usage of biofuels and waste within the Organization for Economic Cooperation and Development countries (OECD) has increased from *86.02* Mtoe (Million Tonners of Oil Equivalent) in 1973 to *279.469* Mtoe in 2013, and the supply of nuclear energy has increased from *48.62* Mtoe in 1973 to *511.481* Mtoe in 2013.

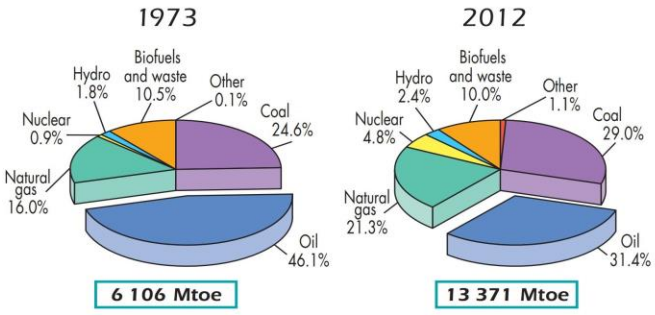

Fig. 1. 1973 and 2013 fuel shares of OECD [1]

However, the growing concern about the safety nuclear energy especially after the 2011 Tohoku Earthquake has impeded the development of nuclear energy around the

world. Consequently, biofuels and organic-based waste are now being considered to be among the best alternative fuels in the near future.

1.1. Motivation

Over the last 20 years, a significant emphasis has been given to the production and use of biofuels including straight vegetable oils as alternative options to fossil fuels. One of the advantages of biofuels is that they can be considered carbon-neutral and less polluting than conventional fuels since many of them possess very small amount of sulfur or nitrogen, which are essential ingredients in the formation of SO_x and NO_x. Recently, straight vegetable oils (SVO) have also been considered as liquid biofuels given their negligible content of sulfur and nitrogen, which is one of the primary reasons why they have great potential to replace conventional fuels [2]. However, the high viscosity of SVO has hindered their ability and applicability in combustion systems. Furthermore, most SVO are characterized by having complex molecular structures, which routinely lead to incomplete combustion under normal conditions. In order to reduce the effect of high viscosity of SVO, methanol has been used as additive to reduce its apparent viscosity. Blends of SVO and methanol have been burnt using a twin-fluid atomizer in a swirl-promoted combustion environment with moderate success [3, 4]. Although biofuel combustion has been studied and discussed by many researchers, most studies have only focused on the combustion of biofuels in engines, and few researchers have considered the combustion of SVO in boilers directly. Furthermore, little is known about the effects of SVO viscosity, SVO blend composition and swirl number on

combustion. Therefore, it is very important to understand the effects of SVO viscosity and swirl number on combustion emissions.

1.2. Objective

The purpose of this study is to understand the effects of induced vorticity (swirl number) and SVO fuel atomization on combustion by following a comprehensive numerical approach, which takes into account fluid dynamics, fluid atomization and combustion kinetics, flame stability simultaneously. To achieve this objective, a robust and stable numerical algorithm should be selected and validated. Firstly, the effects of swirl number on vortex generation should be investigated through numerical simulations when using swirler with flat vanes. The induced vorticity should be studied carefully in order to illustrate the relationship between fluid velocity and vortex structure in a combustion chamber. Furthermore, the effects of vortex generation on fuel droplet distribution should be elucidated. Once induced vorticity has been simulated and analyzed, combustion simulation of well-defined biofuels should be undertaken. This includes a comprehensive numerical effort where the chemical reactions of biofuel species coupled with pressure, velocity, and temperature fields are considered simultaneously. The simulation results should include vorticity strength, the fluid temperature profile inside the combustion chamber as well as the concentrations of combustion products for different swirl numbers and equivalence ratios.

In summary, the study should lead to a better understanding of the effects of vortex generation and droplet distribution on combustion emissions for SVO biofuels. It

is also hoped that this research would be used to identify better combustion strategies for biofuels with high viscosity.

1.3. Overview

This dissertation is divided into six chapters. Chapter II presents a review of literature in the area of numerical simulation of turbulence flow and fuel combustion. Chapter III describes the methodology used in the study, including the computational domain, boundary conditions, properties of fuel, and fundamental review of numerical schemes used in the study. Chapter IV includes the validation of the numerical approach used for turbulent cold flow and droplet spray, as well as numerical results for a swirl-promoted turbulent cold flow and the fuel droplets spray. Chapter V includes the validation of the numerical approach used for fuel droplets combustion, as well as the numerical results for turbulent flow with combustion. The chapter also includes numerical results such as temperature profile, and CO and NO_x emissions. In Chapter VI and Chapter VII, the conclusions and recommendations for future studies is presented, respectively.

2. LITERATURE REVIEW

2.1. Literature review of experimental studies on straight vegetable oil (SVO) combustion

The experimental combustion studies of vegetable oil have been investigated since the 1970s due to the oil crisis and other factors [5]. One of the first research studies that considered the use of vegetable oils as alternative fuels was for diesel engines. It was done in the early 1980's by Strayer et al. [6]. This work suggested that up to *13%* (vol.) anhydrous alcohol can be blended with canola oil in order to reduce and obtain lower viscosity and better flow properties from the oil, respectively. The tests conducted on a small diesel engine showed that *90%* canola oil – *10%* ethanol blend led to reduced power and higher fuel consumption. Krumdieck et al. [7] sprayed and combusted a blend of *90%* (vol.) pyrolysis oil from poplar wood and *10%* (vol.) ethanol in a laboratory scale boiler. They observed fewer visible burning droplets when *10%* ethanol was added to the oil as compared to the case of pure oil combustion. This indicated that ethanol addition improved the performance of the combustor and flame stability. Nettles-Anderson et al. [8] studied the emissions of straight vegetable oil in a direct injection IC engine, using sunflower, canola, camellia, and soybean oils, and concluded that higher levels of polyunsaturated fats (e.g. C18:1, C18:2, and C18:3) produce higher levels of NOx.

Emulsified biofuels have not only been thought as alternate fuels for boilers and diesel engines but also for turbines. Asea Brown Boveri (ABB) was the first company to

test emulsified fuels in turbines in 1985. The paper published by Chellini [9] illustrates the experimental work done on a GEC Alstom, MS9001B 100 MW gas turbine with water-in-diesel emulsion as the fuel. The authors monitored the performance of the turbine for different output levels including *20, 40, 60, 80* and *92.4* MW. The results of the experiments showed that NO_x emissions reduced constantly with increasing amount of water in the emulsion at all the power output levels. The combustion efficiency was same as in case of diesel fuel combustion. The authors suggest that fuel emulsification has proved itself as a new method for reducing emissions as compared to water/steam injection. Chiariello et al. [10] studied the gaseous and particulate emissions from a micro gas turbine that used straight vegetable oil - kerosene blends as energy fuels. The fuel droplets were injected into chamber using a plain-jet air-blast atomizer. Air was introduced into the chamber via a helical swirler. The authors reported that NO_x and *CO* emissions were practically insensitive to the composition of the fuel within the experimental uncertainty of the instrumentation. Al-Shudeifat et al. [11] reported on the combustion of waste trap grease oil in gas turbine generator. In their research, the fuel was injected into chamber using an atomizer, and the results showed that the trap grease led to less NO_x emission for high generator loads compared to diesel, whereas *CO* and CO_2 emissions were slightly higher than those of diesel as the load decreased.

Moreover, numerous experimental works have been done by using optical measurement equipment to understand combustion phenomena better. Those studies looked at the structure of turbulence and flame, and the interaction between turbulence and combustion. For example, Kaminiski et al. [12, 13] used a high speed PLIF

technique to record the evolution of turbulence in real time. Hult et al. [14] employed a time resolved PLIF and instantaneous PIV measurements to study the dynamics of turbulent/chemistry interaction in real time. Chen et al. [15] showed experimental results with Rayleigh scattering and laser-induced fluorescence simultaneously using a high speed premixed hydrocarbon flames. They found a linear relationship between the measured CH signal intensity and the calculated CH concentration within a maximum 30% uncertainty range.

However, there are few published papers which report on the study of swirl-promoted combustion of SVO from the experimental point of view. Cavarzere et al. [16] formulated and tested a variety of straight vegetable oils including rapeseed, sunflower, soybean, rapeseed-diesel blends, sunflower-diesel blends, and soybean–diesel blends in a gas turbine. The study reveals that rapeseed SVO is the most preferable since it cannot be used in the food industry, while soybean SVO is the least preferable. Bhimani et al. [4] studied the combustion characteristics of emulsified canola oil in a swirl-promoted environment. They found that increased vorticity at higher swirl angle led to better mixing and lower emissions, including lower NO_x, *CO* and unburned *HC* emissions than pure canola oil. Savant et al. [3] conducted combustion experiments using corn oil-based blends in a swirl-promoted combustion chamber. They concluded that NO_x emissions increases when used-corn oil is burnt at high swirl number. Furthermore, they found out that all corn oil-based blends showed a generally decreasing *CO* trend at different swirl numbers under very lean conditions.

2.2. Literature review of numerical studies on swirl-promoted turbulent flow in combustion chambers

The study of swirl-promoted turbulent combustion requires proper simulation of the turbulent flow field within the confines of a typical combustion chamber. There are three numerical approaches to simulate turbulent flow especially when a swirler is used, including Reynolds-averaged Navier-Stokes equations (RANS), Direct Numerical Simulation (DNS), and Large Eddy Simulation (LES) [17].

In RANS, a two-equation model is used to solve the continuity, momentum and energy equations using the k-ε approach, which takes into account the turbulent kinetic energy k and dissipation rate of kinetic energy ε [18, 19]. To validate the applicability of k-ε approach in the simulation of flows in combustion chambers, studies that used similar configurations should be considered. Amano [20] used the k-ε model to simulate the turbulent flow downstream of an abrupt pipe expansion, and compared it with experimental measurements. The simulation results showed generally encouraging agreement with the experimental measurements. Zin et al. [21] investigated the influence of length-to-diameter of a pipe expansion on the fluid flow characteristic inside a vortex tube. They concluded that the k-ε model needs to be improved due to the disagreement of the measured and simulated pressure values along the tube. Therefore, k-ε approach should be complemented with another numerical scheme. Furthermore, the k-ε model cannot precisely take into account flow instabilities.

DNS is probably the most advanced algorithm for flow simulations; however, it is computationally expensive. It involves solving the Navier-Stokes equations

numerically without the use of any turbulent model [22]. Luo et al. [23] analyzed the turbulent flow field of three-dimensional n-heptane premixed flame in a swirl combustor using DNS. The gas combustion kinetics were represented using an adaptive one-step irreversible reaction scheme. The variable-density, low-Mach number Navier–Stokes equations were solved using a fully conservative and kinetic energy using a finite difference scheme in cylindrical coordinates with Swirl Number (*SN*) of *1.0*. Tanaka et al. [24] applied DNS to study the gas dynamic behaviors, characteristics of flame structures and heat transfer properties of hydrogen–air turbulent premixed flame in swirling flows. To investigate swirling effects on the flow and combustion fields, DNS of both cold and reactive flow was carried out for two *SN*s of *0.6* and *1.2*. However, DNS requires a huge amount of computational resources especially for complicated geometry [25]. Therefore, a compromise between resolution and computational time is needed to make the best use of computational resources while coming out with sufficient information of the simulated flow field.

LES is another approach used to simulate large eddies found in turbulent flow. In LES, small eddies are filtered in the spectral space and taken into account through modeling. Huang et al. [26] published a review paper and concluded that although the RANS approach currently remains the main workhorse for combustor design analysis, LES is considered to be the next-generation analytical design tool for gas turbine combustors. Therefore, many researchers have reported their research on the flow characteristics of combustion chamber by LES, especially in swirl-promoted flow. Wang et al. [27] presented a comprehensive study on confined swirling flows in an operational

gas turbine injector. The calculated mean velocities and turbulence properties showed good agreement with experimental data. Wang et al. [28] employed LES to study a confined isothermal turbulent swirling flow in a model dump combustor, and reported that the large eddy simulation technique was able to depict the details of the turbulent structure. Kim et al. [29] investigated a swirl-stabilized flow in a gas turbine combustor using large eddy simulation. They observed a complex vortex shedding pattern with significant azimuthal structures in the chamber, and concluded that LES could be useful in the study of the characteristics of swirling flow. Grinstein et al. [30] employed a large eddy simulation to study the non-reacting and reacting-flow in a lean premixed gas turbine combustor with a swirler. The results showed a reasonable agreement with the experimental data. Lu et al. [31] conducted a large eddy simulation analysis with emphasis placed on flow development and its interaction with acoustic waves.

2.3. Literature review of large eddy simulation on swirl-promoted turbulent combustion

LES technique is not only applied to study the fluid dynamics characteristics of turbulent flow, but also used to study the characteristics of turbulent combustion on gaseous and liquid fuels. Huang et al. [32] conducted a numerical study in a gas-turbine combustor. The analysis took into account the finite rate chemical reactions and variable thermophysical properties of methane gas, and employed the LES technique to investigate the combustion dynamics. Wu et al. [33] studied the combustion of methane and propane in meso-scale vortex chambers, and explored flame stabilization mechanism

and chemical efficiency of non-premixed combustion by the LES technique. Stone and Menon [34, 35] investigated the effects of swirl and equivalence ratio on flame dynamics on a swirl-stabilized, lean-premixed gas turbine combustor using LES. The use of a premixed flamelet model, unsteady vortex flame and acoustic flame interactions were captured numerically. The response of the combustion process to explicit swirl modulation was investigated by using the acoustic approach [36].

Furthermore, many researchers have reported that large eddy simulation is capable to couple with the other models when liquid fuels are used. Liu et al. [37] predicted the droplet size distribution in sprays when using air-blast atomizers by using stochastic break-up models. They reported that the nonlinear relationship between the mean droplet diameter and droplet size distribution of the air-blast atomization process can be predicted exactly by this model. Xu et al. [38] employed LES to simulate the fluid flow while the Lagrangian method was used to simulate the motion of particles. They concluded that the LES model can definitely improve the accuracy of the prediction on the mean diameter of droplets. Apte et al. [39] applied the stochastic modeling of secondary breakup to simulate atomizing spray in large eddy simulations. They concluded that LES is computationally efficient and captures the complex fragmentary processes of liquid atomization and fuel droplet motion by coupling with stochastic break-up models.

Moreover, large eddy simulation has been used to capture the droplet distribution of liquid fuels in a swirl-promoted environment. Sankaran and Menon [40, 41] presented the velocity profiles and droplet distribution for General Electric DACRS combustor

using LES. They observed that increasing swirl number accelerated the breakdown of turbulent structures due to the stretch effect, which led to enhanced fuel–air mixing. Jones et al. [42, 43] studied the droplet laden turbulent mixing layer and the influence of shear force on transportation of dispersed phase using large eddy simulation. They also used a stochastic model to simulate the effects of continuous phase on particle motion with LES. Salewski et al. [44] studied the combustion of sprays in a swirl-stabilized gas turbine burner using LES. They found that the low density of droplets in the recirculation zone in the case of reacting flow allowed the fluid to push the recirculation zone downstream, and the low density of droplets resulted in a reduction of the spray dispersion.

Due to the capability of LES technique on coupling with other models to predict the behavior and distribution of droplets, many studies have used large eddy simulation to simulate the turbulent combustion on liquid fuels. Jones et al. [45] investigated swirling kerosene spray flames with LES, and applied the probability density function (PDF) methods to overcome closure problems in turbulent reacting flow simulation. Zhou et al. [46] studied the spray and combustion characteristics in diesel engine using improved LES technique. They concluded that LES technique was capable of predicting the velocity distribution, droplet and vapor phase distribution and combustion characteristics. Sankaran et al. [47] investigated the unsteady interactions between diesel spray dispersion, vaporization, fuel-air mixing and heat release in a realistic combustor using LES. They concluded that large-scale organized structures were subjected to

complex stretch effects due to a combination of streamwise and azimuthal vortex motions.

Compared with conventional gaseous and liquid fuels, straight vegetable oils have complex chemical compositions. In order to improve the simulation accuracy, thermophysical properties need to be studied carefully. Many researchers have used the Kay's mixing rule or group contribution methods to predict the physical properties of fuel blends for combustion modeling. Yuan et al. [48] applied the group contribution method to predict key physical properties of biodiesel, including critical properties, vapor pressure, latent heat of vaporization, density, surface tension, and liquid viscosity. They compared the predicted results with published data and obtained a good agreement. Ceriani et al. [49] proposed a group contribution method to estimate the heat capacities and heats of vaporization of biofuels. Benjumea et al. [50] studied basic properties of the blends of palm oil biodiesel and diesel. They used Kay's mixing rule to predict density, heating value, cloud point, and applied Arrhenius mixing rule to predict viscosity of blends. They reported that the mixing rules they used were suitable to calculate properties of fuel blends.

The formulating chemical reaction mechanisms for combustion is very complicated. Therefore, numerical models of combustors which consider two- or three-dimensional geometry cannot currently include all the kinetic mechanisms [51]. Many researchers use a simplified reaction mechanism in computational fluid dynamics (CFD) codes. Yuan et al. [52] applied a one-step irreversible Arrhenius kinetic model to investigate the spray, ignition and combustion of biodiesel in a diesel engine using a

numerical approach. They found the simulation results by the kinetic model are reasonably accurate. Westbrook and Dryer [53] studied the chemical kinetic modeling of n-butane, and proposed a two-steps reaction mechanism. Yasin et al. [54] used a two-steps heptane reaction mechanism to study the biodiesel spray combustion. Irannejad et al. [55] employed a global chemical kinetic mechanisms when they simulated the high speed evaporation and combustion of n-heptane sprays using LES. They claimed that the simulation results showed a good agreement with the experimental results in term of temperature profile.

As summarized above the combustion of straight vegetable oil has been studied by experimental approach mainly. The combustion of conventional fuel or biodiesel, which has a relatively low viscosity, has been discussed by numerical studies. Moreover, the Large Eddy Simulation technique has been proven to be able to simulate the interactions of turbulent flow and droplet spray as well as the turbulent combustion using a simplified chemical reaction mechanism. However, few researchers have studied swirl-promoted combustion of straight vegetable oil following a numerical approach, capable of providing adequate results which could be used to analyze the details of the turbulent flow field, and the profiles of temperature and emissions during the combustion process. Therefore, the objective of current research is to study the effects of swirl number and equivalence ratio on emulsified canola oil combustion by relying on the Large Eddy Simulation technique by considering applicable modeling schemes.

3. METHODOLOGY OF THE STUDY

A comprehensive and reliable numerical approach has been selected, and used to help understand the effects of combusting SVO with different swirler conditions when mixed with air at varying flowrates. As discussed in chapter II, LES is the most suitable numerical approach to simulate the swirl-promoted turbulent flow in a combustion chamber, as the one described below. The LES technique chosen for simulation was coupled with kinetic chemical reaction models to simulate the overall combustion process of biofuels taking into account the thermodynamics properties of multicomponent mixtures, which include straight vegetable oil. In this chapter, the geometrical structure of a combustion chamber is presented in terms of a computational domain including its boundary conditions. The thermophysical properties of emulsified canola oil are also introduced. Specific details about the numerical approach are explained which fully accounts for turbulent flow, the droplets spray, and the applicable chemical reactions.

3.1. Description of combustion chamber geometry with boundary conditions

The geometry of a relatively common combustion chamber is based on a small scale combustion chamber located in the Coal and Biomass Energy Laboratory (CBEL) at Texas A&M University. The combustion chamber is rated at *30* kW and was initially built by Dr. Annamalai's former students, and was modified by Dr. Alvarado's former student Shreyas Bhimani who used it for the combustion of vegetable oil fuels [56]. The

schematic representation of the combustion chamber is shown in Fig. 2, which was generated using CAD software (SolidWorks 2014, SolidWorks Corporation). It consists of a short guiding *50.8* mm pipe, a long *101.6* mm guiding pipe, a metal cone in the long guiding pipe, a swirl generator, a twin fluid atomizer, and a *152.4* mm combustion chamber. The total height of combustion chamber located in the CBEL is *2.4* meters. Figure 2 shows a section of the whole combustion chamber, or one quarter of the whole system.

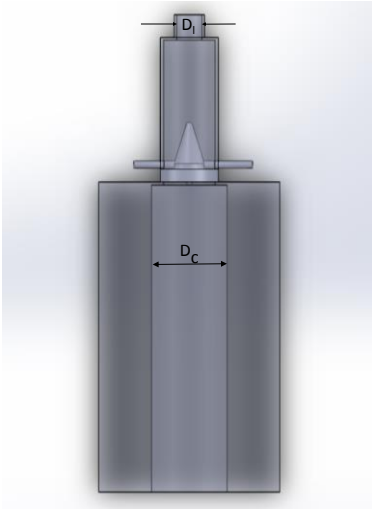

Fig. 2. Schematic of combustion chamber

The twin fluid atomizer is an air-blasted type, which has a *0.5* mm inner diameter orifice at its bottom-center. The atomizer is placed such that the tip of nozzle is positioned approximately *5* mm above the bottom edge of swirl generator. The swirl

generator consists of eight flat vanes with an inclination angle of *51°* or *60°* as shown in Fig. 3. The two different vane inclination angles were used to generate different levels of vorticity within the combustion chamber. It has a hub at the center of swirler, which has a diameter of *59.4* mm. The outer diameter of swirler is *100.4* mm, and the height of swirler is *25.4* mm. The vane inclination angle in combination with the diameters of the swirler are represented by the swirl number, and defined as the ratio of angular momentum to the axial momentum of air flow inside the combustion chamber [57].

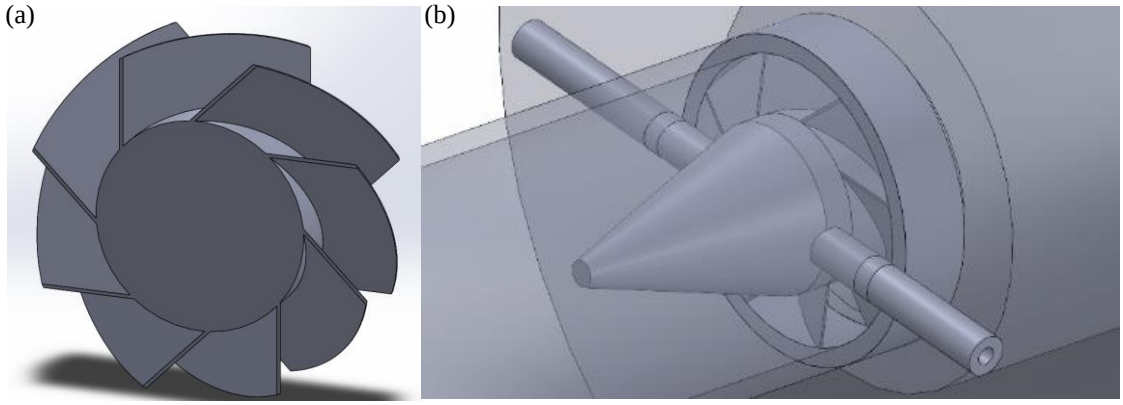

Fig. 3. (a) Front view of swirler, (b) Assembly drawing of swirler in guiding pipe

The swirl number of an annular swirler with constant vane angle is given by Equation 1:

$$SN = \left(\frac{2}{3}\right)\left[\frac{1-\left(\frac{R_h}{R}\right)^3}{1-\left(\frac{R_h}{R}\right)^2}\right]\left(Tan(\alpha)\right) \quad (1)$$

Where, *SN* is swirl number; R_h is the outer radius of the hub; *R* is the inner radius of the hub; α is the vane angle. In this study, two swirl numbers (*SN*) of *1.0* and *1.4* are considered during the simulation process.

Table 1. Flow Conditions for SN of 1.0 and 1.4

Cases	Equivalent Ratio	$\dot{V}$ (l/min)	D_l (mm)	D_c (mm)	Re_l	Re_c
SN = 1.0	0.81	403	101.6	152.4	11,484	3,840
	0.97	336	101.6	152.4	9,576	3,202
SN = 1.4	0.81	403	101.6	152.4	11,484	3,845
	0.97	336	101.6	152.4	9,576	3,202

Flow conditions for two *SN*s are shown in Table 1. Reynolds number is based on a volume flow rate and the corresponding local diameter D_l and D_c, where subscripts *l* and *c* represent the short gilding pipe and combustion chamber, respectively. The volume flow rate of air $\dot{V}$ is an adjustable parameter used to adjust the equivalence ratio (ϕ), during the combustion simulations, which was calculated by the following equation.

$$\phi = \left[\frac{\left(\frac{Fuel}{air} \right)_{Provided}}{\left(\frac{Fuel}{air} \right)_{Stoichiometic}} \right] \quad (2)$$

In this study, the flow rate of primary air, which is used to generate the fuel droplets in atomizer, is *10* l/min. The flow rates of secondary air, which flows through

the guiding pipe, is *393* l/min and *326* l/min, respectively. Therefore, the two corresponding equivalent ratios are *0.81* and *0.97*.

3.2. Description of fuel thermophysical properties

A *85-12.5* emulsion [*12.5*% methanol – in – *85*% canola oil (w/w) emulsion with *2.5*% surfactant] has been studied by Bhimani et al. [4] experimentally. The results of that study show that swirl number has a significant effect on emission levels. In order to understand the effect of swirl number on the overall combustion process, the chemical reactions should be simplified when conducting numerical simulations. During the combustion simulations, the effect of surfactant on combustion was neglected. Therefore, the mass ratio of emulsified biofuel blend was set to *87.2 – 12.8* emulsion [*12.8*% methanol – in – *87.2*% canola oil (w/w) emulsion].

Pure canola oil of Crisco brand [58] and *99.9*% concentrated methanol from EMD biosciences [59] was used for making the emulsions. The properties of pure canola oil are obtained by Bhimani's experimental work [4] and estimated by the group contribution method [60]. The thermophysical properties of pure canola oil at *25* °C are shown in Table 2.

The thermophysical properties of emulsified canola oil have been obtained from Bhimani's experimental work [4] and estimated by using the Kay's mixing rule [61]. The thermophysical properties of emusilfied canola oil at *25* °C are shown in Table 3.

Table 2. Thermophysical properties of pure canola oil at 25 °C (% mass)

Property	Pure Canola Oil
Fatty acid of pure canola oil (%)	
Palmitic acid (C 16:0)	4.93
Palmitoleic acid (C 16:1)	0.33
Stearic acid (C 18:0)	2.21
Oleic acid (C 18:1)	63.96
Linoleic acid (C 18:2)	19.17
Linolenic acid (C 18:3)	9.40
Dynamic viscosity* (cP)	55
Density* (kg/m^3)	962
Surface tension* (N/m)	0.0278
HHV* (kJ/kg)	40,173
Specific heat (kJ/(kg-K))	1.94
Latent heat (kJ/mol)	59.28
Flash point (K)	452
Boiling point (K)	621
Thermal conductivity (W/(m-K))	0.20
* Bhimani, S. [4]	

Table 3. Thermophysical properties of emulsified canola oil at 25 °C (% mass)

Property	Pure Canola Oil
SVO composition	
Pure canola oil (%)	87.2
Methanol (%)	12.8
Dynamic viscosity* (cP)	41.2
Density* (kg/m^3)	881.5
Surface tension* (N/m)	0.026
HHV* (kJ/kg)	37,506
Specific heat (kJ/(kg-K))	2.01
Latent heat (kJ/mol)	56.27
Flash point (K)	431
Boiling point (K)	585
Thermal conductivity (W/(m-K))	0.20
* Bhimani, S. [4]	

The chemical formula of emulsified canola oil has been obtained from Bhimani's experimental work [4]. Miscibility could have an effect on surface tension and droplet size; however, the mixing rule was used, which assumes complete miscibility or homogenous mixture without the use of surfactants. In fact, methanol is indeed miscible in canola oil up to 8% by volume as described by Bhimani [4]. Therefore, after

neglecting the components such as nitrogen and sulfur, the chemical formula of emulsified canola oil is $C_{6.65}H_{11.329}O_{0.8513}$, and the empirical formula is $CH_{1.704}O_{0.128}$.

3.3. Description of grid generation and numerical algorithm

The computation domain is based on the structure shown in Fig. 2. The computational mesh was generated by ICEM CFD (ANSYS, Inc.). The region of the metal cone and swirler was meshed using a tetrahedral grid, and the rest region of domain was meshed using a hexahedral grid, as shown in Fig. 4. The grid points are *4.8* million, and the resolution is *0.5* mm in the radial direction and *4* mm in the axial direction. The validation of mesh will be discussed in details in the next chapter.

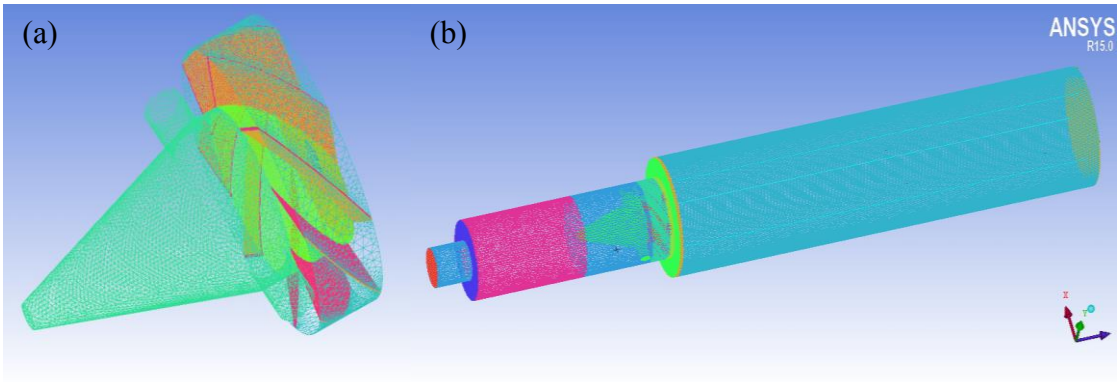

Fig. 4. Computational mesh of (a) Cone and Swirler, (b) Entire domain

In this study, commercial program ANSYS Fluent 15 was employed to study the turbulent flow, fuel droplet spray and combustion numerically. The pressure-based segregated solver was selected, which is the SIMPLE algorithm. RANS was used as

turbulence viscous model firstly, which was used to obtain an initial solution of velocity flow field. Then the LES technique was employed to obtain detailed vortex structures of air-fuel turbulent flow. The numerical algorithms of RANS, LES and pressure-based solver are discussed below.

In the computational domain, the theoretical formulation is based on the full conservation equations of mass momentum, energy and species concentration in Cartesian coordinates as follows [62]:

$$\frac{\partial \rho}{\partial t} + \frac{\partial \rho u_i}{\partial x_i} = 0 \tag{3}$$

$$\frac{\partial \rho u_i}{\partial t} + \frac{\partial \left(\rho u_i u_j\right)}{\partial x_j} = -\frac{\partial p}{\partial x_i} + \frac{\partial \tau_{ij}}{\partial x_j} \tag{4}$$

$$\frac{\partial \rho E}{\partial t} + \frac{\partial \left[\left(\rho E + p\right)u_j\right]}{\partial x_i} = -\frac{\partial q_i}{\partial x_i} + \frac{\partial \left(u_i \tau_{ij}\right)}{\partial x_j} \tag{5}$$

$$\frac{\partial \rho Y_k}{\partial t} + \nabla \cdot \left(\rho \vec{v} Y_k\right) = -\nabla \cdot \vec{J}_k + R_k \tag{6}$$

Where *i*, *j*, and *k* are the spatial coordinate index, the dummy index to spatial coordinate, and the species index, respectively. Y_k and $\vec{v}$ are mass fraction and diffusion velocities of species *k*, respectively. R_k is the net rate of production of species *k* by chemical reaction. J_k is the diffusion flux of species *k*. The viscous stress and heat flux vector are τ_{ij} and q_j, which are shown below.

$$\tau_{ij} = \mu\left(\frac{\partial u_i}{\partial x_j} + \frac{\partial u_j}{\partial x_i} - \frac{2}{3}\delta_{ij}\frac{\partial u_l}{\partial x_l}\right) \tag{7}$$

$$q_j = -\lambda \frac{\partial T}{\partial x_j} + \rho \sum_{k=1}^{N} h_k Y_k U_{k,j} \tag{8}$$

Where μ and λ are the coefficients of viscosity and heat conductivity, respectively.

The specific total E is given by

$$E = e + \frac{u_j u_j}{2} \tag{9}$$

e is the specific internal energy, which is obtained as:

$$e = h - \frac{p}{\rho} \tag{10}$$

h is the specific enthalpy of mixture, which is shown as following:

$$h = \sum_{k=1}^{N} Y_k h_k = \sum_{k=1}^{N} Y_k \left(\Delta h_{f,k}^{\circ} + \int_{T_{ref}}^{T} C_{p,k}(T')dT' \right) \tag{11}$$

Where $C_{p,k}$ is the species specific heat at constant pressure.

In turbulent flow, the diffusion flux of species *k* is computed in the following form:

$$\vec{J}_k = \left(\rho D_{k,m} + \frac{\mu_t}{Sc_t} \right) \nabla Y_k - D_{T,k} \frac{\nabla T}{T} \tag{12}$$

Where Sc_t is the turbulent Schmidt number ($\frac{\mu_t}{\rho D_t}$ where μ_t is the turbulent viscosity and D_T is the turbulent diffusivity). The default Sc_t is *0.7*.

In the simulation of turbulent flow, the continuity, momentum and energy equations are solved using the k-ε model of the RANS approach, which takes into account the turbulent kinetic energy *k* and dissipation rate of kinetic energy *ε*. In ANSYS

Fluent, the standard k-ε model is a model based on transport equation for the turbulence kinetic energy (k) and its dissipation rate (ε) as shown below [62].

$$\frac{\partial}{\partial t}(\rho k)+\frac{\partial}{\partial x_i}(\rho k u_i)=\frac{\partial}{\partial x_j}\left[\left(\mu+\frac{\mu_t}{\sigma_k}\right)\frac{\partial k}{\partial x_j}\right]+G_k+G_b-\rho\varepsilon-Y_M+S_k \tag{13}$$

$$\frac{\partial}{\partial t}(\rho \varepsilon)+\frac{\partial}{\partial x_i}(\rho \varepsilon u_i)=\frac{\partial}{\partial x_j}\left[\left(\mu+\frac{\mu_t}{\sigma_\varepsilon}\right)\frac{\partial \varepsilon}{\partial x_j}\right]+C_{1\varepsilon}\frac{\varepsilon}{k}(G_k+C_{3\varepsilon}G_b)-C_{2\varepsilon}\rho\frac{\varepsilon^2}{k}+S_\varepsilon \tag{14}$$

Where, G_k represents the generation of turbulence kinetic energy due to the mean velocity gradients; G_b is the generation of turbulence kinetic energy due to buoyancy; Y_m represents the contribution of the fluctuating dilatation in compressible turbulence to the overall dissipation rate; $C_{1\varepsilon}$, $C_{2\varepsilon}$, and $C_{3\varepsilon}$ are constant; σ_k and σ_ε are the turbulent Prandtl numbers for k and ε, respectively; S_k and S_ε are user-defined source terms. In Fluent, the default values of constant $C_{1\varepsilon}$, $C_{2\varepsilon}$, σ_k and σ_ε are *1.44*, *1.92*, *1.0* and *1.3*, respectively [62].

The RANS approach was applied firstly to initialize the flow field of the computational domain and to speed up the convergence of simulation. Then LES was then applied to obtain the detailed vortex structure of turbulent flow in the domain. In ANSYS Fluent, large eddies, which are larger than the subgrid-scale, are resolved directly, while small eddies are modeled numerically [62]. Therefore, the subgrid-scale stresses, which correspond to small eddies are filtered and modeled accordingly. When applying the Large Eddy Simulation (LES) technique during the simulation process, the following filtered Navier-Stokes equation is obtained:

$$\frac{\partial \rho \bar{u}_i}{\partial t}+\frac{\partial\left(\rho \bar{u}_i \bar{u}_j\right)}{\partial x_j}=-\frac{\partial \bar{p}}{\partial x_i}+\frac{\partial}{\partial x_j}\left(\mu\frac{\partial \sigma_{ij}}{\partial x_j}\right)-\frac{\partial \tau_{ij}}{\partial x_j} \tag{15}$$

Where σ_{ij} is the stress tensor due to molecular viscosity of μ. τ_{ij} is the subgrid-turbulent stress component, which is based on the Boussinesq hypothesis which is used by ANSYS Fluent. It can be calculated as follows [62]:

$$\tau_{ij} = \frac{1}{3}\tau_{kk}\delta_{ij} - 2\mu_t \bar{S}_{ij} \tag{16}$$

Where μ_t is the subgrid-scale turbulent viscosity. The isotropic part of the subgrid-scale stresses τ_{kk} is not modeled, but added to the filtered static pressure term of $\bar{p}$. δ_{ij} is the Kronecker delta. $\bar{S}_{ij}$ is the rate-of-strain tensor for the resolved scale defined by

$$\bar{S}_{ij} = \frac{1}{2}\left(\frac{\partial \bar{u}_i}{\partial x_j} + \frac{\partial \bar{u}_j}{\partial x_i}\right) \tag{17}$$

In ANSYS Fluent, the basic approach used to solve the subgrid-scale turbulent viscosity μ_t is based on the Smagorinsky-Lilly model, as follows:

$$\mu_t = \rho L_s^2 \left|\bar{S}\right| \tag{18}$$

where $|\bar{S}| = \sqrt{2\bar{S}_{ij}\bar{S}_{ij}}$. L_s is the mixing length for subgrid scales and is computed using $L_s = \min(\kappa d, C_s\Delta)$, where κ is the von Karman constant of *0.41*, and *d* is the distance to the closest wall. C_s is the Smagorinsky constant, which has the default value of *0.1* in Fluent. Δ is computed according to the volume of the computational cell using $\Delta = V^{1/3}$. The Smagorinsky-Lilly model assumes that the energy production and dissipation of the small scale are in equilibrium.

For liquid fuel droplet modeling, the Discrete Phase Model (DPM) [62] was used to generate the fuel droplets. The physical model for simulating the behavior of the

discrete phase was based on the stochastic collision model, which has been used in the past with liquid fuels [62]. The breakup of fuel droplets was considered by using the Taylor Analogy Breakup model (TAB) [62], which is based on the analogy between an oscillating and distorting droplet as a spring-mass system commonly used for fuel droplet break up [62]. The detailed numerical algorithms to generate the fuel droplets and to simulate the fuel droplet-gas interactions using ANSYS Fluent are explained below.

In ANSYS Fluent, the discrete phase model is based on the Lagrangian discrete phase model [62]. The fluid phase is treated as a continuum by solving the Navier-Stokes equation, while the dispersed phase is solved by tracking a large number of particles, bubbles, or droplets through the calculated flow field. The dispersed phase can exchange momentum, mass, and energy with the fluid phase, and the interactions between particles are neglected [62]. The trajectory of a discrete phase particle is predicted by integrating the force balance on each particle, and the force balance equation can be written as [62]

$$\frac{d\vec{u}_p}{dt} = F_D\left(\vec{u} - \vec{u}_p\right) + \frac{\vec{g}\left(\rho_p - \rho\right)}{\rho_p} + \vec{F} \tag{19}$$

Where, $\vec{u}$ is the fluid phase velocity. $\vec{u}_p$ is the particle velocity, ρ is the fluid density, and ρ_p is the density of the particle. $\vec{F}$ is an additional acceleration (force/unit particle mass) term (inertia-based). $F_D\left(\vec{u} - \vec{u}_p\right)$ is the drag force per unit particle mass and

$$F_D = \frac{18\mu}{\rho_p d_p^2}\frac{C_D \,\mathrm{Re}}{24} \tag{20}$$

Where, μ is the molecular viscosity of the fluid, d_p is the particle diameter, and C_D is the drag coefficient for a spherical droplet. *Re* is the relative Reynolds number, which is defined as

$$\mathrm{Re} = \frac{\rho d_p \left| \vec{u}_p - \vec{u} \right|}{\mu} \tag{21}$$

In ANSYS Fluent, the drag coefficient C_D for smooth particles or spherical droplets can be obtained as follows:

$$C_D = a_1 + \frac{a_2}{\mathrm{Re}} + \frac{a_3}{\mathrm{Re}^2} \tag{22}$$

Where a_1, a_2, and a_3 are constants that apply over several ranges of *Re* as shown in the study of Morsi et al. [63].

As explained above, a twin-fluid atomizer was used to inject fuel droplets into the combustion chamber as a spray of emusified canola oil [4]. The atomizer is supplied with two fluids, with liquid fuel on one side and high pressure air on the other. The atomizer has a mixing chamber within it, where the air stream impinges on the liquid jet and forms a good quality liquid-gas mixture which is then sprayed as a very fine mist. The size of fuel droplest is determined by the pressure of air and liquid fuel in the atomizer.

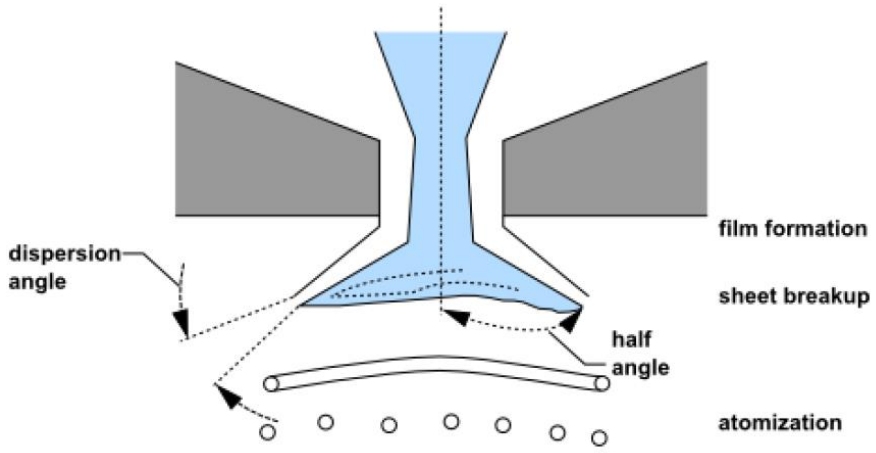

Fig. 5. Schemetic diagram for fuel sprays generation

In the numerical method, the air-blast atomization model or the discrete phase model has been selected, where a fuel liquid is formed into a sheet by the nozzle, and air is then directed against the sheet to promote atomization as shown in Fig. 5 [62]. The operating principles of atomizer model (i.e. discrete phase model) are the same as the atomizer used in the experiments.

According to ANSYS Fluent [62], the sheet breakup in the air-blast model is based on the formation of short waves around the fuel nozzle. The diameter of the ligament that leads to the formation of fuel droplets is assumed to be linearly proportional to the wavelength that breaks up the sheet, as follows:

$$d_L = \frac{2\pi C_L}{K_s} \tag{23}$$

Where C_L is the ligament constant of *0.5*. K_s is the wave number, which can be calculated as follows:

$$K_s = \frac{\rho_l U^2}{2\sigma} \tag{24}$$

Where ρ_l is density of fuel, U is local relative velocity between fuel and air in the nozzle, and σ is the surface tension of fuel droplet.

The diameter of fuel droplets can be obtained as follows:

$$d_0 = 1.88 d_L (1 + 3Oh)^{1/6} \tag{25}$$

Where Oh is the Ohnesorge number, which is a combination of the Reynolds number and the Weber number.

Based on the explanation above, the size of the fuel droplets depends on the relative velocity between fuel and air in the simulated fuel nozzle. It is known that the relative velocity between both streams depends on the pressure of air and liquid fuel in the atomizer, which induces the necessary shear flow to form a thin liquid ring and eventually a fine dispersion of droplets.

In turbulent flow, ANSYS Fluent uses the mean fluid phase velocity $\bar{u}$ to predict the trajectories of particles [62]. In the stochastic tracking approach, ANSYS Fluent predicts the turbulent dispersion of particles by integrating the trajectory equations of individual particles, using the instantaneous fluid velocity of $u = \bar{u} + u'(t)$ along the particle path. By computing the trajectory of particles, the random effects of turbulence on the particle dispersion can be taken into account [62].

In order to take into account the effect of droplet breakup on sprays, the Taylor Analogy Breakup (TAB) model has been applied. In ANSYS Fluent, the TAB model is based on Taylor's analogy between an oscillating and distorting droplet and a spring-

mass system. When the droplet oscillations reach a critical value, the "parent" droplet will break up into a number of smaller "child" droplets. The results of the TAB model equation can be used to determine the droplet oscillation and distortion at any time [62]. The equation governing a damped, forced oscillator is given by:

$$F - kx - d\frac{dx}{dt} = m\frac{d^2x}{dt^2} \tag{26}$$

Where x is the displacement of the droplet from its spherical position. The coefficients in the equation, $\frac{F}{m}$, $\frac{k}{m}$, $\frac{d}{m}$, are taken from Taylor's analogy [62]:

$$\frac{F}{m} = C_F\frac{\rho_g u^2}{\rho_l r} \tag{27}$$

$$\frac{k}{m} = C_k\frac{\sigma}{\rho_l r^3} \tag{28}$$

$$\frac{d}{m} = C_d\frac{\mu_l}{\rho_l r^2} \tag{29}$$

Where ρ_l and ρ_g are the discrete phase and continuous phase densities, respectively. u is the relative velocity of the droplet, r is the undisturbed droplet radius, σ is the droplet surface tension, and μ_l is the droplet viscosity. The values of C_F, C_k and C_d are *1/3*, *8* and *5*, which represents the constant values of droplet drag force, surface tension forces, and droplet viscosity forces, respectively.

When the distortion reaches half of the droplet radius, the droplet is assumed to break up, as shown in Fig. 6.

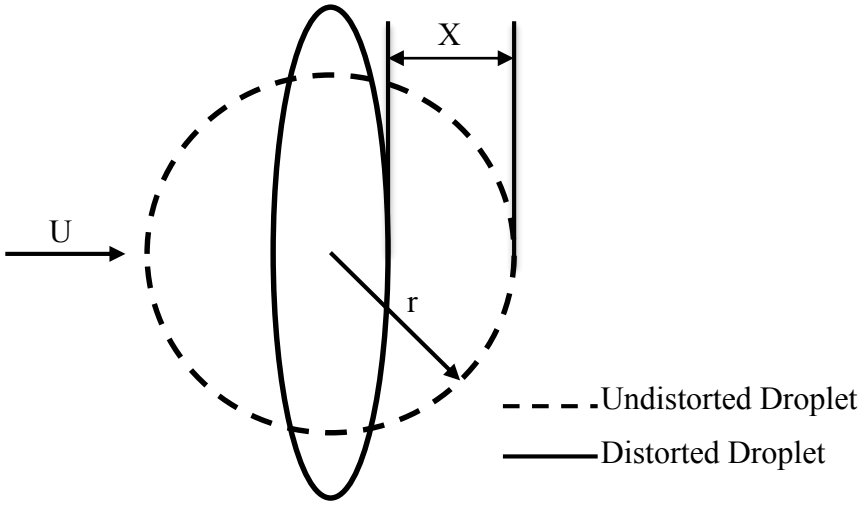

Fig. 6. Particle distortion for the TAB model

The breakup requirement is given as follows [62]:

$$x > C_b r \tag{30}$$

Where C_b is a constant with a value of *0.5*.

By setting $y = \frac{x}{C_b r}$ and substituting the relationships in Equations 27-29 in Equation 26, the new nondimensionalized control equation is given as

$$\frac{d^2 y}{dt^2} = \frac{C_F}{C_b}\frac{\rho_g}{\rho_l}\frac{u^2}{r^2} - \frac{C_k \sigma}{\rho_l r^3} y - \frac{C_d \mu_l}{\rho_l r^2}\frac{dy}{dt} \tag{31}$$

The solution of equation is shown as follows:

$$y(t) = We_c + e^{-\left(t/t_d\right)}\left[\left(y_0 - We_c\right)\cos\left(\omega t\right) + \frac{1}{\omega}\left(\frac{dy_0}{dt} + \frac{y_0 - We_c}{t_d}\right)\sin\left(\omega t\right)\right] \tag{32}$$

Where

$$We = \frac{\rho_g u^2 r}{\sigma} \tag{33}$$

$$We_c = \frac{C_F}{C_k C_b} We \tag{34}$$

$$y_0 = y(0) \tag{35}$$

$$\frac{dy_0}{dt} = \frac{dy}{dt}(0) \tag{36}$$

$$\frac{1}{t_d} = \frac{C_d}{2} \frac{\mu_l}{\rho_l r^2} \tag{37}$$

$$\omega^2 = C_k \frac{\sigma}{\rho_l r^3} - \frac{1}{t_d^{\,2}} \tag{38}$$

If equation is solved for all droplets, those with $y > 1$ are assumed to break up. In order to simulate the turbulent combustion process, the Eddy-Dissipation model [62] was applied. It takes into account the effects of chemical reaction and turbulent flow simultaneously. In ANSYS Fluent, the Eddy-dissipation model assumes reaction rates are controlled by the turbulent mixing. The model is based on the work of Magnussen and Hjertager [64]. The net rate of production of species *i* due to reaction *r* is given by the following equations

$$R_{i,r} = v'_{i,r} M_{w,i} A \rho \frac{\varepsilon}{k} \min_R \left(\frac{Y_R}{v'_{R,r} M_{w,R}} \right) \tag{39}$$

$$R_{i,r} = v'_{i,r} M_{w,i} AB \rho \frac{\varepsilon}{k} \frac{\sum_P Y_P}{\sum_j^N v''_{j,r} M_{w,j}} \tag{40}$$

Where,

$v'_{i,r}$ = stoichiometric coefficient for reactant *i* in reaction *r*

$v'_{R,r}$ = stoichiometric coefficient for reactant *R* in reaction *r*

$v''_{j,r}$ = stoichiometric coefficient for product *j* in reaction *r*

$M_{w,i}$ = the molecular weight of species *i*

$M_{w,j}$ = the molecular weight of species *j*

$M_{w,R}$ = the molecular weight of species *R*

Y_P = the mass fraction of any product species, *P*

Y_R = the mass fraction of a particular reactant, *R*

A = an empirical constant of *4.0*

B = an empirical constant of *0.5*

When the LES turbulence model is used, the turbulent mixing rate, *ε/k*, in Equation 39 and 40, is replaced by the subgrid-scale mixing rate, which is calculated as [62]

$$\tau_{sgs}^{-1} = \sqrt{2S_{ij}S_{ij}} \tag{41}$$

Where,

τ_{sgs}^{-1} is subgrid-scale mixing rate (s^{-1})

$S_{ij} = \frac{1}{2}\left(\frac{\partial u_i}{\partial x_j} + \frac{\partial u_j}{\partial x_i}\right)$ is strain rate tensor (s^{-1})

When considering a r_{th} reaction, the general form of the reaction can be written as follows:

$$\sum_{i=1}^{N} v'_{i,r}\chi_i \underset{k_{b,r}}{\overset{k_{f,r}}{\Leftrightarrow}} \sum_{i=1}^{N} v''_{i,r}\chi_i \tag{42}$$

Where, χ_i is the chemical formula of species *i*. $k_{f,r}$ and $k_{b,r}$ is the reaction rate constants of the forward and backward reactions, respectively. The reaction rate constant of forward reaction can be obtained as follows:

$$k_{f,r} = Ae^{-E/RT} \tag{43}$$

Where, A is the pre-exponential factor. E is the activation energy for the reaction (J/kmol). R is the universal gas constant (J/kmol-K).

The reaction rate constant of forward reaction is calculated as follows:

$$k_{b,r} = \frac{k_{f,r}}{K_r} \tag{44}$$

Where K_r is the equilibrium constant for the r_{th} reaction, which is shown as follows:

$$K_r = \exp\left(\frac{\Delta S_r}{R} - \frac{\Delta H_r}{RT}\right)\left(\frac{P_{atm}}{RT}\right)^{\sum_{i=1}^{N}\left(\nu''_{i,r} - \nu'_{i,r}\right)} \tag{45}$$

Where P_{atm} is the atmospheric pressure. The terms within the exponential function can be calculated as follows:

$$\frac{\Delta S_r}{R} = \sum_{i=1}^{N}\left(\nu''_{i,r} - \nu'_{i,r}\right)\frac{S_i}{R} \tag{46}$$

$$\frac{\Delta H_r}{RT} = \sum_{i=1}^{N}\left(\nu''_{i,r} - \nu'_{i,r}\right)\frac{h_i}{RT} \tag{47}$$

Where S_i and h_i are the entropy and enthalpy of the i^{th} species evaluated at temperature T and atmospheric pressure.

According to the studies of Westbrook and Dryer [53] and Yasina [54], a two-step reaction mechanism is selected as the chemical kinetic reaction mechanism. The stoichiometric combustion equations for the two-step mechanism is shown in Table 4.

Table 4. Two steps chemical reaction mechanism of emulsified canola oil

Reaction	Pre-Exponential Factor (A)	Activation Energy (E) (J/kg-mol)
$CH_{1.6305}O_{0.0806} + 0.867O_2 \rightarrow CO + 0.81525H_2O$	5×10^5	6.6×10^7
$CO + 0.5O_2 + H_2O \Leftrightarrow CO_2 + H_2O$	3.98×10^{11}	1.6736×10^8

During the combustion process, the formation of thermal NO_x is determined by a set of highly temperature-dependent chemical reactions known as the Zeldovich mechanism. The principal reactions governing the formation of the thermal NO_x are shown as follows [62]:

$$O + N_2 \Leftrightarrow N + NO$$

$$N + O_2 \Leftrightarrow O + NO$$

A third reaction has been shown to contribute to the formation of thermal NO_x, particularly at near conditions and in fuel-rich mixtures [62]:

$$N + OH \Leftrightarrow N + NO$$

The rate for these reactions can be expressed as follows [62]:

$$k_{f,1} = 1.8\times10^8 e^{-38370/T} \quad k_{r,1} = 3.8\times10^7 e^{-425/T}$$

$$k_{f,2} = 1.8\times10^4 e^{-4680/T} \quad k_{r,2} = 3.81\times10^3 e^{-20820/T}$$

$$k_{f,3} = 7.1\times10^7 e^{-450/T} \quad k_{r,3} = 1.7\times10^8 e^{-24560/T}$$

The net rate of formation of *NO* is calculated as follows:

$$\frac{d[NO]}{dt} = 2k_{f,1}[O][N_2]\frac{\left(1-\frac{k_{r,1}k_{r,2}[NO]^2}{k_{f,1}[N_2]k_{f,2}[O_2]}\right)}{\left(1-\frac{k_{r,1}[NO]}{k_{f,2}[O_2]+k_{f,3}[OH]}\right)} \left(\text{mol/m}^3\text{-s}\right) \quad (48)$$

Table 5 shows all the models used during the simulations including their applicability and limitations.

Table 5. Description of Simulation Models

Model	Applicability	Limitation
Large Eddy Simulation	Turbulent Flow	Should not be used for complex geometry and very high Reynolds number because of the need for high computational resources
Discrete Phase Model	Discrete phase trajectory using a Lagrangian formulation for both steady and unsteady flows	Cannot be used for high volume fraction of discrete phase, usually larger than 12%.
Stochastics Model	The dispersion of particles due to turbulence in the fluid phase	Cannot be included if the Spalart-Allmaras turbulence model is used
Taylor Analogy Breakup (TAB) Model	Used to determine the droplet drag coefficient for low-speed sprays into a standard atmosphere	Cannot be used for high-Weber-number sprays
Eddy-Dissipation Model	Turbulence-chemistry interaction reaction	Requires products to initiate reaction (LFR model)

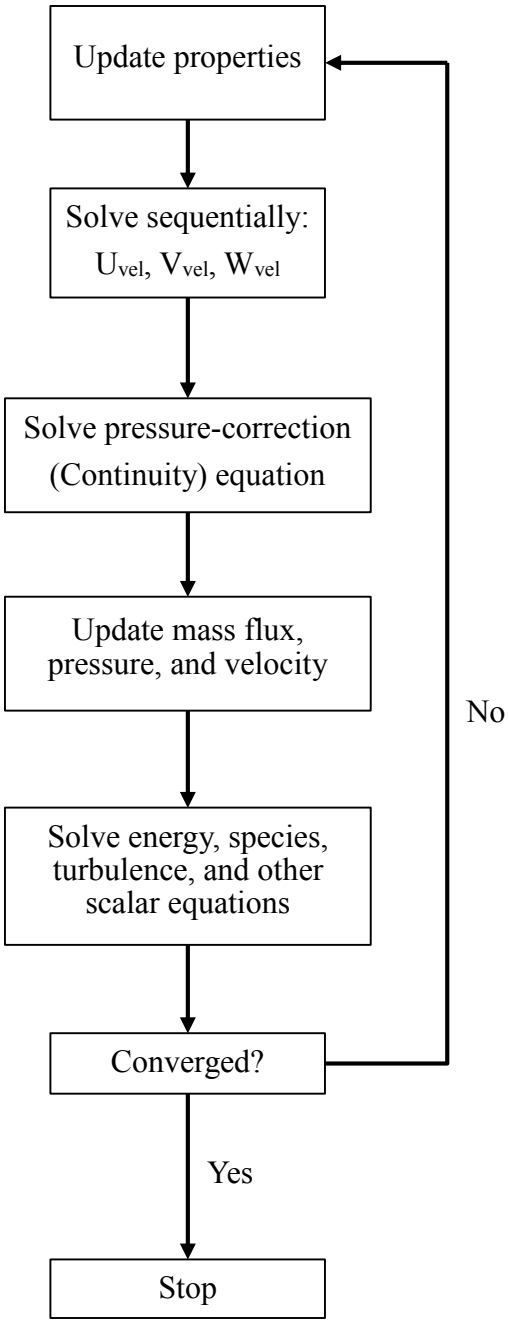

Fig. 7. Overview of the pressure-based solver

In term of the computational algorithm, Semi-Implicit Method for Pressure-Linked Equations (SIMPLE) algorithm was selected to solve the pressure-velocity coupling. According to ANASYS Fluent [62], the SIMPLE algorithm uses a relationship between velocity and pressure correlations to enforce mass conservation and to obtain the pressure field. The overview of this algorithm is shown in Fig. 7 [62].

The spatial discretization method used has a second-order accuracy based on a central-differencing scheme for the momentum, energy and species equations. A control-volume-based technique was used to convert the general scalar transport equation to an algebraic system [62]. The control volume technique consists of integrating the transport equation about each control volume, yielding a discrete equation that expresses the conservation law on a control-volume basis. The discretization of the governing equations are illustrated by considering the unsteady conservation equation for transport of a scalar quantity ϕ. The following equation written in integral form for an arbitrary control volume V as follows:

$$\int_V \frac{\partial \rho \phi}{\partial t} dV + \oint \rho \phi \vec{v} \cdot d\vec{A} = \oint \Gamma_\phi \nabla \phi \cdot d\vec{A} + \int_V S_\phi dV \tag{49}$$

Where

P is the density

$\vec{v}$ is the velocity vector

$\vec{A}$ is the surface area vector

Γ_ϕ is the diffusion coefficient for ϕ

$\nabla\phi$ is the gradient of ϕ

S_ϕ is the source of ϕ per unit volume

Equation 41 can be applied to a control volume or cell in the computation domain. For a give cell, equation 41 can be shown as follows:

$$\frac{\partial \rho \phi}{\partial t} V + \sum_{f}^{N_{faces}} \rho_f \vec{v}_f \phi_f \cdot \vec{A}_f = \sum_{f}^{N_{faces}} \Gamma_\phi \nabla \phi_f \cdot \vec{A}_f + S_\phi V \tag{50}$$

Where

N_{faces} is the number of faces enclosing cell

ϕ_f is the value of ϕ converted through face f

$\rho_f \vec{v}_f \cdot \vec{A}_f$ is mass flux through the face

$\vec{A}_f$ is area of face f

$\nabla \phi_f$ is the gradient of ϕ at face f

V is the cell volume

For the second-order discretization, $\frac{\partial \rho \phi}{\partial t} V$ in Equation 42 is defined as follows:

$$\frac{\partial \phi}{\partial t} = F(\phi) = \frac{3\phi^{n+1} - 4\phi^{n} + \phi^{n-1}}{2\Delta t} \tag{51}$$

Where

ϕ is a scalar quantity

n+1 is the value at the next time level, $t + \Delta t$

n is the value at the current time level, t

n-1 is the value at the previuos time level, $t - \Delta t$

In ANSYS Fluent [62], a second-order-accurate central-differencing discretization scheme is available for the momentum equations when the LES turbulence

model is used. This scheme provides improved accuracy for LES calculations. The central-differencing scheme calculates the face value for a variable (ϕ_f), as follows:

$$\phi_f = \frac{1}{2}(\phi_0 + \phi_1) + \frac{1}{2}\left(\nabla\phi_0 \cdot \vec{r}_0 + \nabla\phi_1 \cdot \vec{r}_1\right) \tag{52}$$

Where the indices *0* and *1* refer to the cells that share face *f*. $\nabla\phi_{r,0}$ and $\nabla\phi_{r,1}$ are the reconstructed gradients at cells *0* and *1*, respectively, and $\vec{r}$ is the vector directed from the cell centroid toward the face centroid.

The PREssure STaggering Option (PRESTO!) scheme was used for pressure interpolation. In ANSYS Fluent [62], the PRESTO! Scheme uses the discrete continuity equation to calculate the pressure field on a mesh that is geometrically shifted so that the new cell centers are where the faces of the ordinary mesh are located. This means that the pressures on the faces can be determined [62]. Fig. 8 shows a structured grid for the PRESTO! Scheme, where the shade area illustrates the staggered grids.

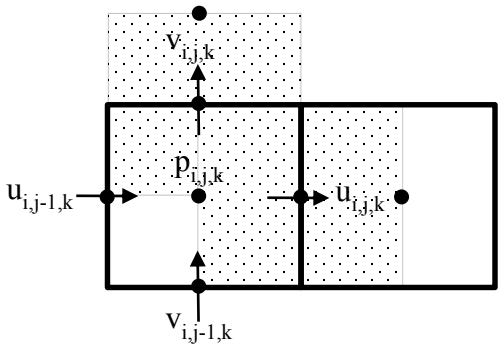

Fig. 8. Schematic diagram of the PRESTO! Scheme

In order to analyze the size distribution of vortices, the Fast Fourier Transform (FFT) method was used using MATLAB. FFT is a mathematical algorithm which is used to calculate the Discrete Fourier Transform (DFT) [65]. DFT is based on a mathematical operation such as the Fourier transform, which converts a signal into its constituent frequencies. Once Fourier transform is done, all the signals on the time-domain are computed into signals on the frequency domain. According to the study by Cooley and Tukey [65], a given vectors of length N can be transformed by FFT as follows:

$$\mathrm{X(k)} = \sum_{j=1}^{N} x(j)\omega_N^{(j-1)(k-1)} \tag{53}$$

Where, $\omega_N = e^{(-2\pi i)/N}$, which is an N_{th} root of unity.

Once the frequency spectrum of each flow structure has been determined, it is used to understand the effect of Swirl number and flowrate on the distribution of eddy size in the flow, as shown in Chapter 5.

4. LARGE EDDY SIMULATION OF SWIRL PROMOTED TURBULENT COLD FLOW IN A COMBUSTION CHAMBER

The distribution and combustion of fuel droplets is highly dependent on the flow field in in any combustion chamber. For droplets entrained in a gas stream, understanding the evolution of turbulent flow is the key in the study of combustion processes and emission generation in a combustion chamber. In this chapter, the simulation of turbulent flow field without combustion is validated using the chosen numerical approach, as outlined in the previous chapter. The velocity profile, streamlines and vorticity distribution of cold flow in a combustion chamber are shown and discussed. Furthermore, the simulation of fuel droplets distribution is validated by comparing with Jones' experimental results [66]. The effects of flow field on fuel droplets distribution have been studied as described below.

4.1. Validation of numerical approach on turbulent flow field

To validate the numerical approach for simulating swirling flow in the prescribed combustion chamber, the first step is to simulate and study the turbulent flow without the swirler. The simulation of a sudden expanding flow is based on the work by Wessman [67], which was used to validate the current simulation results in terms of velocity profile and experimental data shown in Wessman [67].

The experimental setup used by Wessman [67] is shown in Fig. 9(a). It consists of a long guiding pipe, and a sudden expansion chamber. The inlet bulk velocity was set

to *1.59* m/s. Coarse and fine meshed grids with *2.1* million and *4.6* million cells, respectively, were generated using ANSYS ICEM CFD as shown in Fig. 9 (a) and (b), respectively.

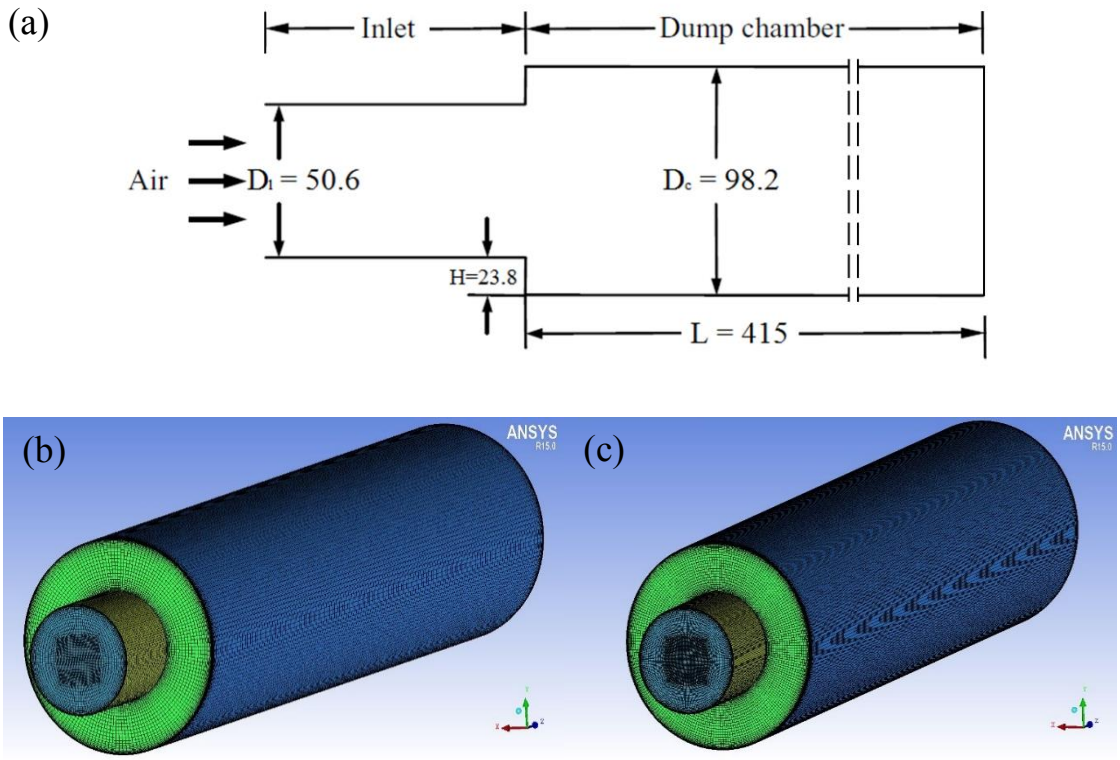

Fig. 9. (a) Schematic of a chamber with an inlet duct. Dimensions are in mm, (b) a coarse grid mesh of sudden expansion chamber used for validation, (c) a fine grid mesh of sudden expansion chamber used for validation

The numerical simulation was performed using ANSYS Fluent 15.0. The simulation was based on the Reynolds Averaged Navier Stokes (RANS) equation with the k-ε turbulence model first. The Large Eddy Simulation (LES) technique was used when the solution of RANS converged. The Semi-Implicit Method for Pressure-Linked

Equations (SIMPLE) algorithm was used for pressure-velocity coupling scheme, and the second order wind was used for the spatial discretization of pressure, momentum, and the other parameters. The time interval was set to 10^{-5} s.

The simulation results of two cases compared with the analytical solution of pressure drop, which was calculated using the Bernoulli's Equation as shown below.

$$\frac{\mathrm{P}_1}{\rho \mathrm{g}} + \frac{V_1^2}{2g} + z_1 - h_{loss1} - h_{expan} - h_{loss2} = \frac{\mathrm{P}_2}{\rho \mathrm{g}} + \frac{V_2^2}{2g} + z_2 \tag{54}$$

Where,

$$h_{lossi} = f\,\frac{L_i}{D_i}\frac{V_i^2}{2g}\,(\mathrm{f} = 0.0176 \ \text{from Moody chart}) \tag{55}$$

$$h_{\text{expansion}} = \left(1 - \frac{A_1}{A_2}\right)^2 \frac{V_1^2}{2g} \tag{56}$$

$$z_1 = z_2 = 0 \tag{57}$$

The comparison between the two cases and their simulation results with analytical solution are shown in Table 6.

According to Table 6, the fine grid case gives a small error when compared to the analytical solution. The fine grid with a resolution is *0.5* mm in the radial direction and *4* mm in the axial direction was chosen for simulation purposes. Fig. 10 shows the comparison of experiment data [67] with simulation results obtained using the grid shown in Fig. 9(b) and (c), at three axial locations. Time averaged axial velocity, $\langle u \rangle$, and bulk velocity at inlet of guiding pipe, U_b; the radial position, r, and the radial of guiding pipe, R; were used as physical variables during the simulation process. The non-

dimensional axial location shown in Fig. 10 is the ratio of axial position, *z*, to the step height, *H*.

Table 6. Comparison of simulation results with analytical solution for the chamber without swirler

Cases	Number of grids	Type of grid	simulation value of pressure drop (Pa)	Analytical value of pressure drop (Pa)	Error (%)
Coarse Grid	2.1 million	Hexahedron	35.2	38.3	8.1
Fine Grid	4.6 million	Hexahedron	37.1	38.3	3.1

In Fig. 10, the solid line depicts the simulation result, which is based on the fine grid and the numerical algorithm explained above. The data points represent the experimental results shown in Wessman [67]. As Fig. 10 shows, the implemented approach can accurately simulate turbulence flow for the case described above. The other simulations were based on the same resolution of mesh and numerical algorithm.

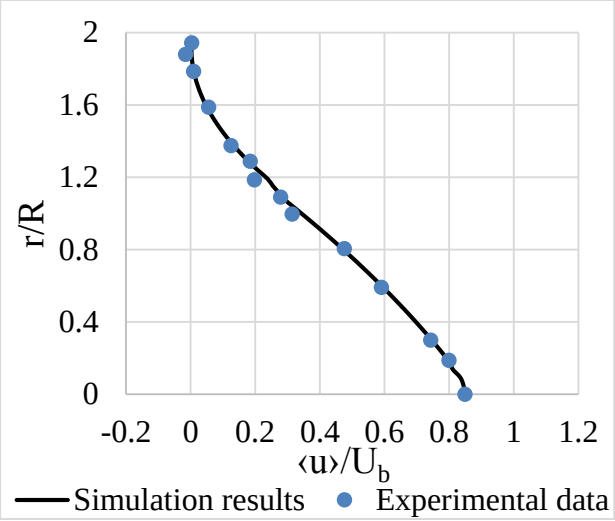

Fig. 10. Comparison of simulation and experimental results for turbulent flow without swirler at axial location of *z/H=10.5*

In order to validate the numerical methods used for simulating turbulent flow with a swirler, the simulation with the swirler was compared first with the experimental tests conducted by Favaloro [68]. The experimental setup is shown in Fig. 11. It consists of a long guiding pipe, a swirl generator, and a sudden expansion chamber. The inlet bulk velocity is *19.2* m/s. The swirler with *12* circular inlet guide vanes is located at *50.8* mm upstream of the dump plane. The swirl number is *0.5*.

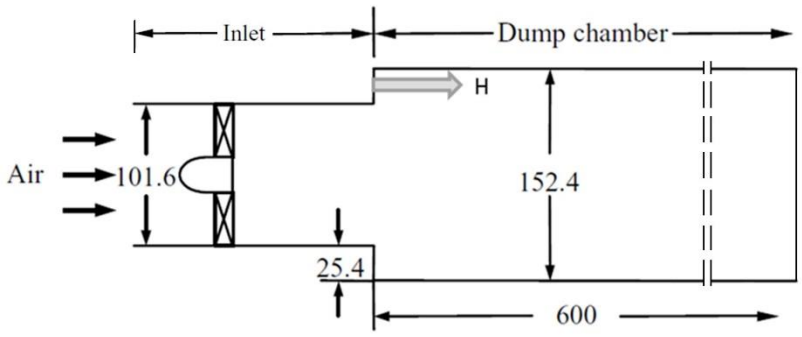

Fig. 11. Schematic of a sudden expansion chamber with swirler. Dimensions area in mm.

Computational meshes were generated using ANSYS ICEM CFD. Three meshes were generated, including a coarse mesh with tetrahedron grid elements (*1.9* million), a fine mesh with tetrahedron grid elements (*3* million), and a fine mesh with a combination grid (*4.1* million), which is made of tetrahedron grid elements for the region around the swirler and hexahedron grid elements for the rest of region of domain, respectively. All three meshes are based on the same approach and resolution used for the validation of turbulent flow without swirler. The three meshes are shown in Fig. 12 (a), (b), and (c), respectively.

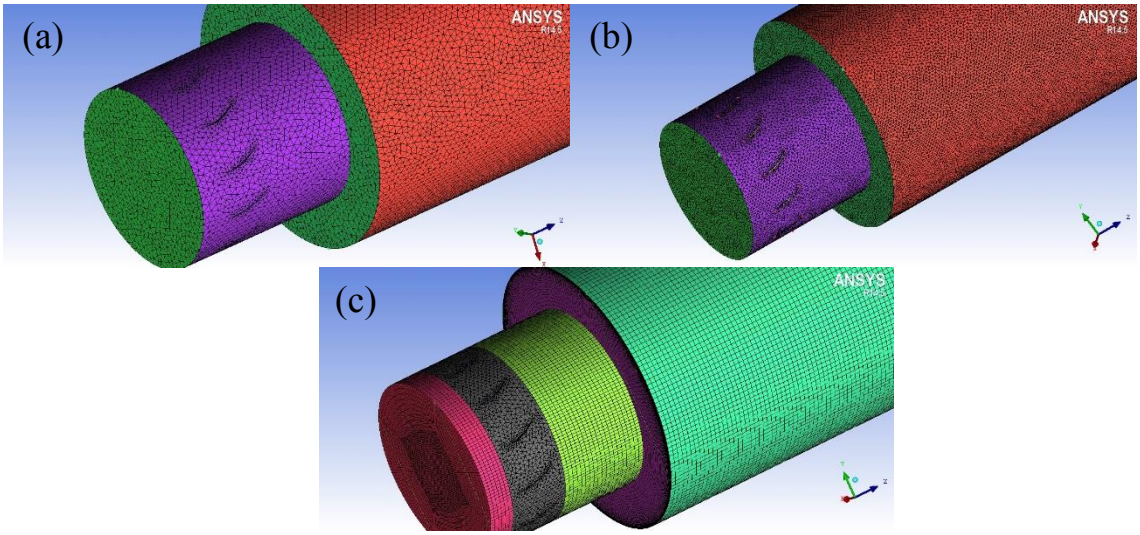

Fig. 12. (a) Coarse mesh with tetrahedron grid elements; (b) Fine mesh with tetrahedron grid elements; (c) Fine mesh with a combination grid

The numerical algorithm is the same as the one used for the validation cases without a swirler. The simulation was based on the Reynolds Averaged Navier Stokes (RANS) equation and the k-ε turbulence. LES was used when the solution of RANS converged. The time interval was set to 10^{-5} s. Simulation data are collected for about *3* flow-through times (*66* ms) to obtain statistically meaningful turbulent properties. The simulation results were compared using radial distributions of time-mean normalized velocity profile at a location (z/H) of as shown in Fig. 13.

Fig. 13 shows that the combination grid gives the best agreement with experimental data when compared with the other two meshes. Therefore, the simulation of turbulent flow for the combustion chamber in the CBEL is based on the combination mesh, Fig 12c. Fig 14 shows the radial distribution of the time-mean axial, radial and azimuthal normalized velocity components at three locations (z/H) of *0.38* and *4.0*,

respectively. The combination mesh was used, and the simulations were compared with the experimental data of Favaloro [68]. After completing the validation process, the CBEL swirler was meshed and used accordingly, as described below.

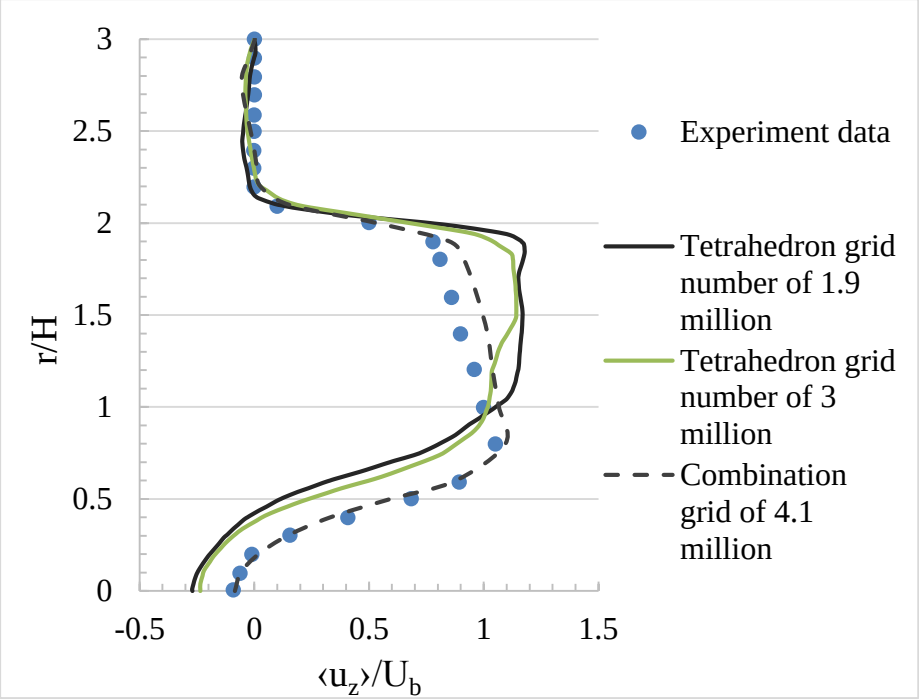

Fig. 13. Comparison of three simulation cases and experimental data for the chamber with swirler at axial location (z/H) of *0.38*

According to Fig. 14, the simulation results agree reasonable well with the experimental data in the three directions of velocity. Therefore, the approach used for mesh generation and the numerical algorithm can be used for the simulation of turbulent flow in the combustion chamber described above.

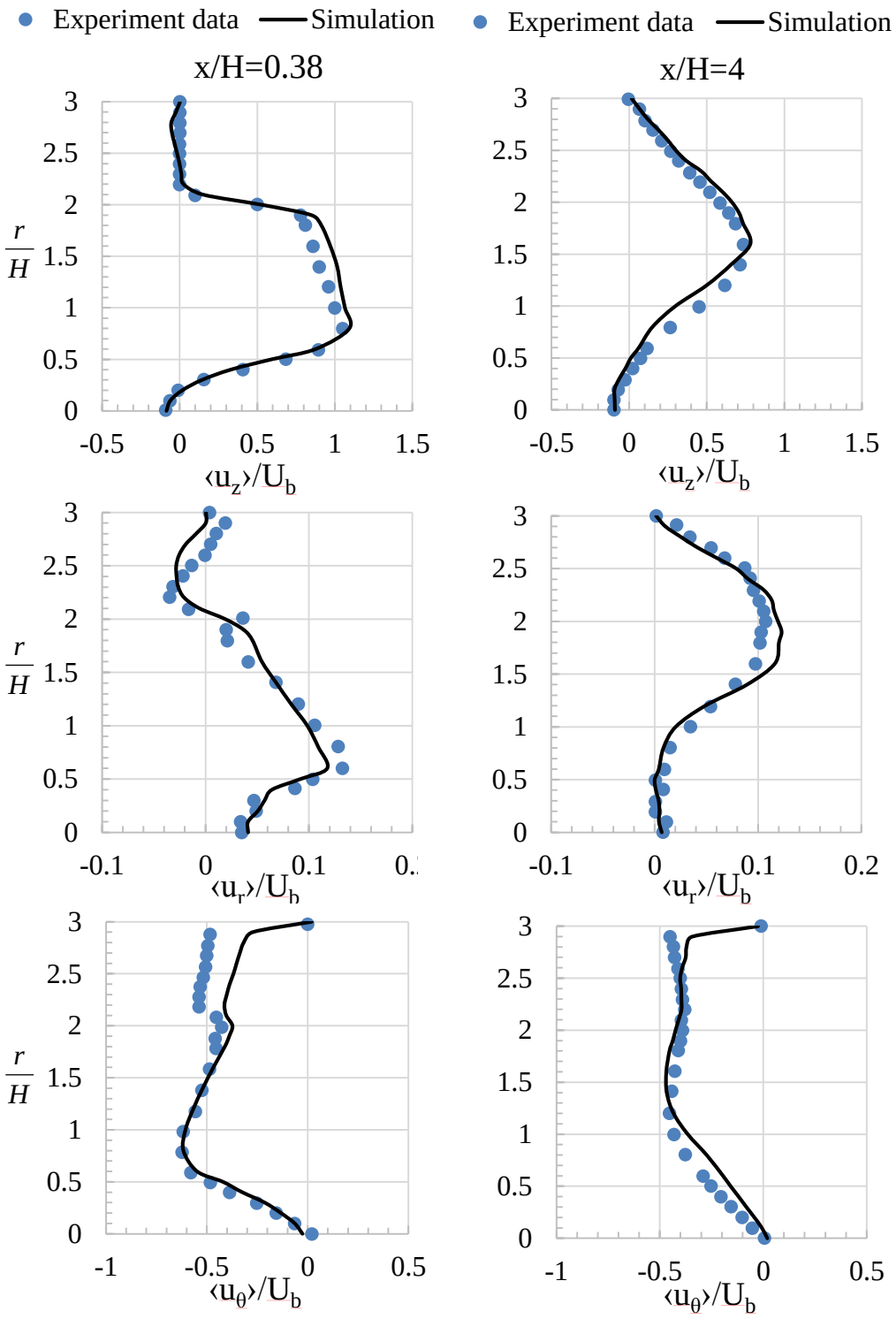

Fig. 14. Radial distribution of mean velocity components at two axial locations

4.2. Large eddy simulations of swirl-promoted turbulent cold low in combustion chamber.

In order to understand the combustion processes and corresponding emissions in swirl promoted flows, obtaining realistic turbulent flow field is the key to be able to analyze the effects of swirl number and fuel properties on combustion. This section discusses the effects of swirl number on turbulent flow field without combustion by analyzing velocity profiles and turbulent kinetic energy in the combustion chamber. It also presents the evolution of flow vortices in the combustion chamber, which have been analyzed using streamlines and the Q-criterion of vortices.

For the combustion studies, the simulation domain and schematic of the geometry of the CBEL swirler are shown in Fig. 2 and Fig. 15, respectively. The flow conditions are in Table 1 including a flow rate of *393* l/min with *SN* of *1.0* and *1.4*. The computational mesh as shown in Fig. 16 was generated using ANSYS ICEM CFD following the same approach as explained above. ANSYS Fluent was used as the mathematical solver to obtain the corresponding numerical solutions. The initial time interval was set to be 10^{-5} s, and then increased to 5×10^{-5} s in order to reduce the simulation time. The Courant number of *0.6* is based on the time interval of 5×10^{-5} s.

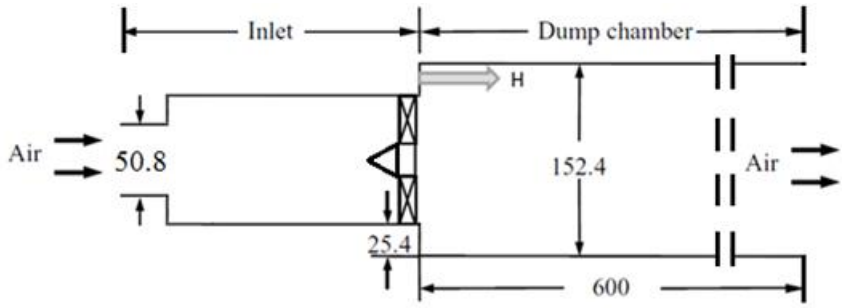

Fig. 15. Schematic of domain for swirl promoted turbulent simulation. Dimensions is in mm.

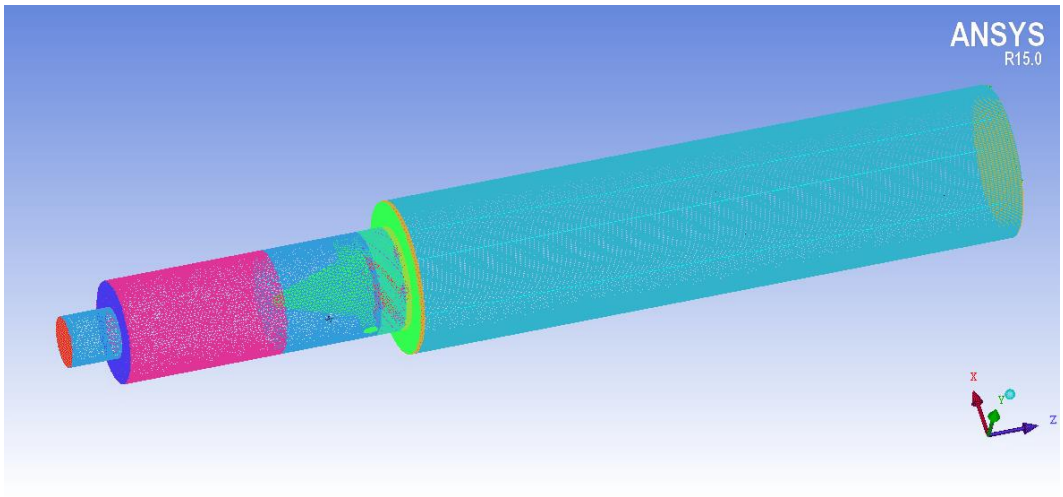

Fig. 16. Combination mesh for swirl promoted turbulent simulation

4.2.1. Effects of swirl number on recirculation zones within the combustion chamber

Swirlers are used in combustion chambers [69] to produce Central toroidal Recirculation Zones (*CRZ*) to enhance the mixing of fuel and oxygen. The characteristic of *CRZ* is affected by swirl number notably. In this section, the profiles of normalized

time mean velocity and turbulent kinetic energy are discussed in terms of three axial locations. The shape of recirculation zone is shown using iso-surface of mean axial velocity on $<u_z> = 0$. The types of recirculation zone and the corresponding evolution process are considered.

Fig. 17(a) – (c) shows radial distributions of the normalized time averaged axial, tangential, and radial velocity components at three measurement locations (z/H) of *0.38*, *1.0*, and *4.0* for swirl number (*SN*) of *1.0* and *1.4*, respectively. Fig. 17(a) shows that the axial velocity is negative between the inner wall of the swirler and the wall of the chamber. It implies that reverse flow is produced in the chamber, which is part of the recirculation zone. Comparing the cases of *SN* of *1.0* and *1.4*, it is observed that the range of the negative normalized velocity is larger for *SN* of *1.4* than for *SN* of *1.0*. This implies that a high swirl number there is an overall expansion of the recirculation zone. This is due to the centrifugal effect, which spreads the flow in the radial direction gradually. The location of the peak positive axial velocity is close to the wall, when a high swirl number is used. The effect of swirl number diminishes along the axial direction and converges to a similar axial velocity profile at the location (z/H) of *4*. The tangential velocity profile is shown in Fig. 17(b). The swirler with a high swirl number produces greater tangential velocity, and the largest tangential velocity is created near the outlet region of the swirler, where the radial position (r/R) varies from *0.39* to *0.67*. The tangential velocity decreases along the axial direction; however, its average value decreases faster with low swirl number.

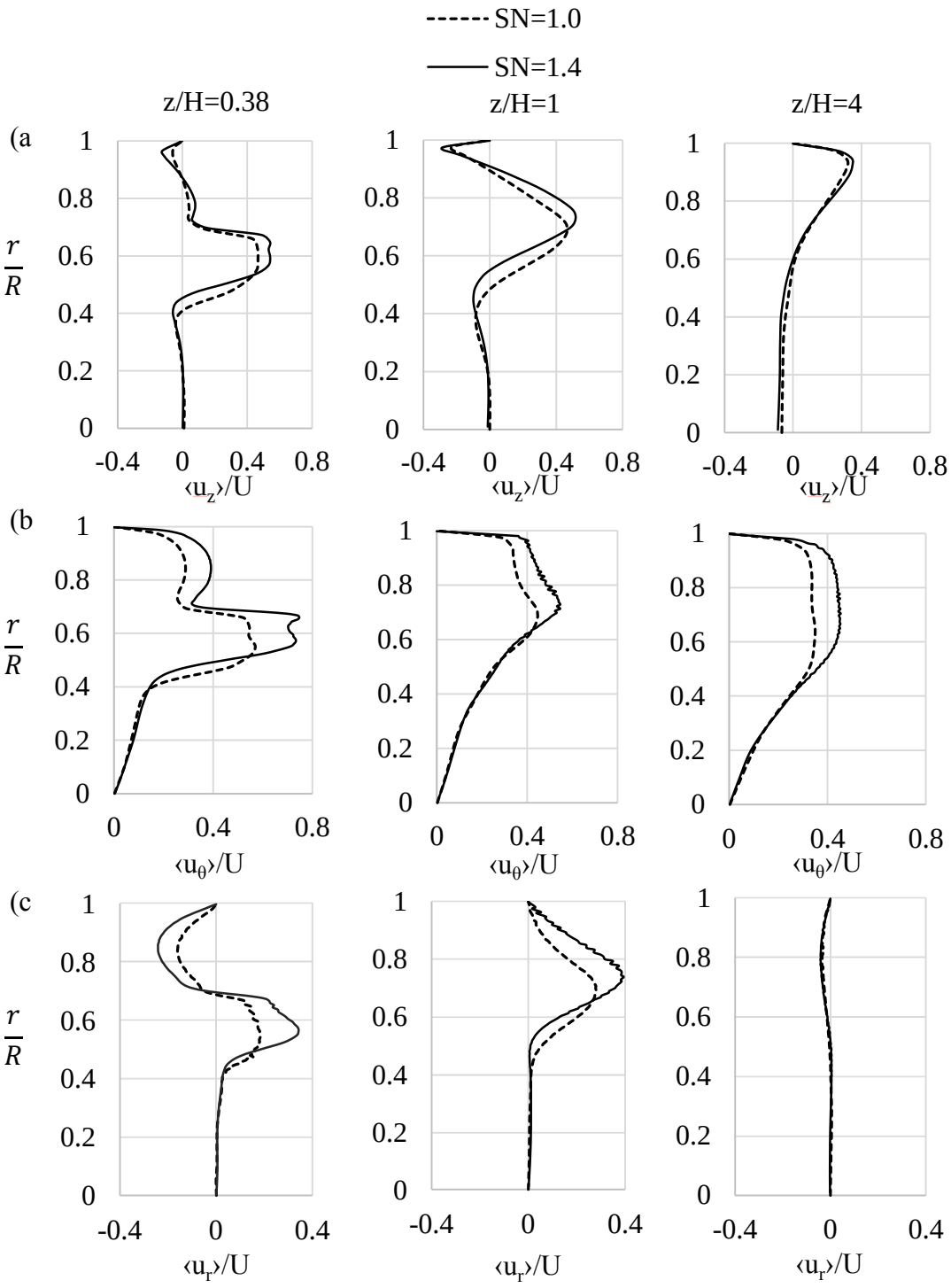

Fig. 17. Radial distribution of time-averaged normalized velocity components at (a) axial direction, (b) radial direction, (c) tangential direction, respectively

Both axial and tangential velocity reduce along the axial direction; however, the radial velocity increases in the downstream region as shown in Fig. 17(c). Within the outlet region of the swirler, the energy and momentum remain almost the same, and neither dissipate by turbulent diffusion or viscous dissipation. Therefore, the momentum which is generated by the axial and tangential velocities is converted to radial momentum, which leads to an increase in radial velocity. In addition, the radial velocity magnitude for *SN* of *1.4* is also greater than for *SN* of *1.0* due to greater centrifugal effect.

Fig. 18 shows the turbulent kinetic energy at three locations. It is observed that it reaches a peak at the location (z/H) of *0.38*. It implies that the shear layer which is a result of the Kelvin-Helmholtz instability, dominates the flow at this location. A shear layer is induced by the helical vortex flow and recirculation taking place within the zone between the swirler and the radial plane located (z/H) at *0.38*. This layer can be categorized as a buffer zone between the core of the recirculation zone and the helical vortex flow that goes around it. Fig. 18 also shows that at a *SN* of *1.4* leads to a wider center recirculation zone than for a *SN* of *1.0*. Additionally, the development of the flow structure expands radially and becomes more uniform in the downstream region. The smooth distribution of turbulent kinetic energy in the downstream region shows that turbulence tends to become isotropic under the effects of turbulent dispersion and viscous dissipation.

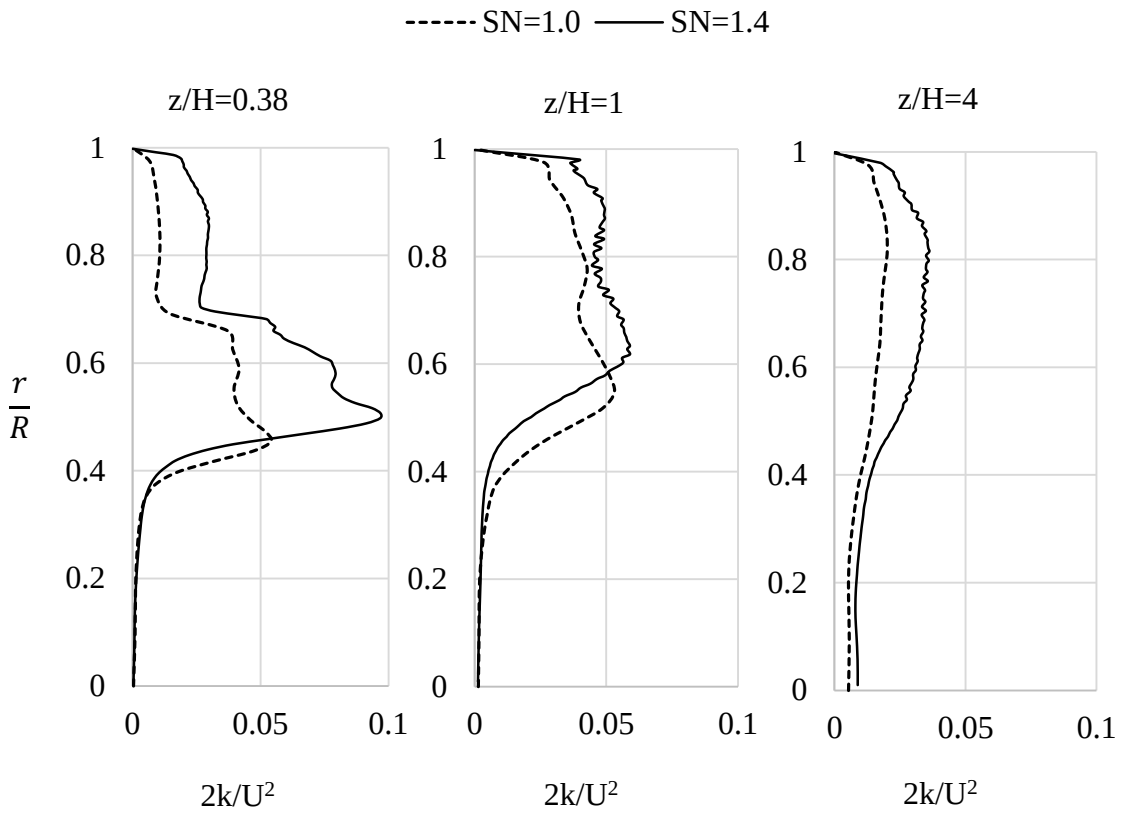

Fig. 18. Radial distribution of normalized turbulent kinetic energy

Fig. 19(a) and (b) show the shape of recirculation zones using iso-surface of time-averaged axial velocity on $\langle u_z \rangle = 0$ for *SN* of *1.0* and *1.4*, respectively. The black solid lines are two reference lines to identify the size of the center of recirculation zone in the spanwise direction. In Fig. 19, the green surface shows a time-averaged axial velocity of zero. The region, where the axial velocity is less than zero, is inside the green surface. Hence, the green surface in the center of chamber represents the shape of center recirculation zone, and the green surface, which is near the inlet of combustion chamber, is the corner of the recirculation zone. As shown in Fig. 19, for a *SN* of *1.4* not only

leads to a wider center of recirculation zone than for a *SN* of *1.0* in the spanwise direction near the swirler, but also produces a longer center of recirculation zone in the streamwise direction, which validates the findings seen in Fig. 17 and 18. Therefore, the center recirculation zone for high swirl number is much greater than that of a low swirl number.

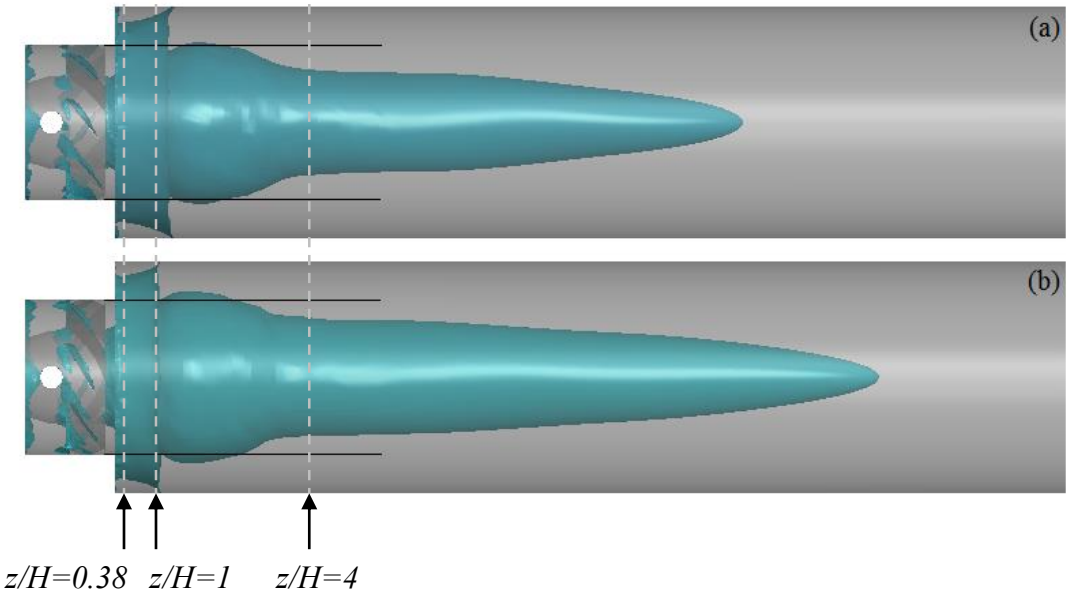

Fig. 19. Iso-Surface of time-averaged axial velocity on $\langle u_z \rangle = 0$ for (a) *SN* of *1.0* and (b) *SN* of *1.4*

4.2.2. Effects of swirl number on flow structure within the combustion chamber

The flow structure is relevant to this study because of its dominant influence in determining the fuel droplet distribution and the mixing of fuel and oxygen, which is relevant in combustion kinetics. In this section, a *sn*apshot of a vorticity profile on the *z*-

r plane and the streamline on the *z-r* and *r-θ* plane are presented and analyzed to understand the flow structure in the chamber. The effects of swirl number on flow structure are discussed as well.

Fig. 20 is a snapshot of vorticity profile at the z-r plane for *SN* of *1.0* and *SN* of *1.4* at flow time of *500* ms. It shows that the greatest size of vortices, represented by the colors on the scale, are generated near the outlet region of the swirler for both *SN* of *1.0* and *1.4* due to the dump plane and the wake and helical flow induced by vane. The vortices break down along the axial direction due to the presence of counter-rotating vortices within the buffer zone next to the core recirculation zone as it is shown below. In terms of the effects of swirl number, *SN* of *1.4* generates larger sizes of vortices based on the strength of the vortices depicted in color in Fig. 20. In the next chapter, Fast Fourier Transfer analysis indicate that the size of the vortices are greater for *SN* of 1.4. It can also be inferred that the speed of turbulent diffusion and dissipation is slower than for a *SN* of *1.0* since it has greater angular momentum.

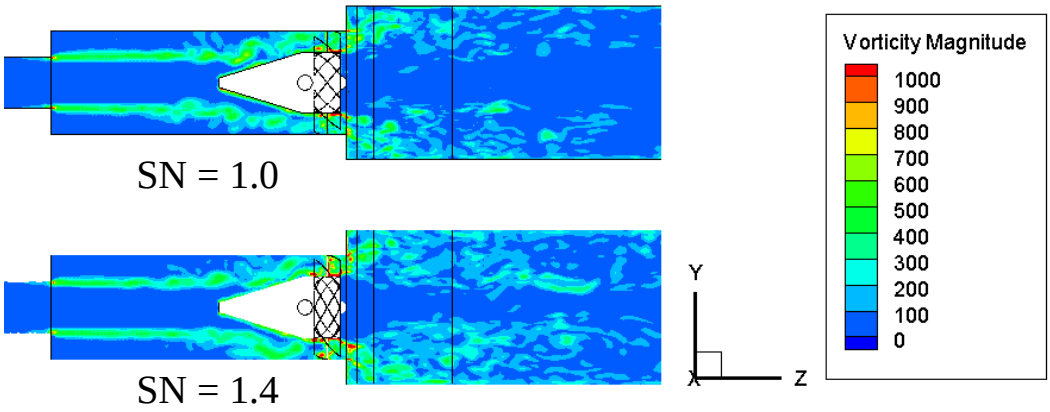

Fig. 20. Snapshot of vorticity profile at the *z-r* plane on *SN* of *1.0* and *SN* of *1.4* at flow time of *500* ms

To facilitate the visualization of the vortices, the streamlines at the r-θ planes at axial locations (z/H) of *0.38*, *1*, and *4* for *SN* of *1.0* and *1.4* are presented in Fig. 21(a) - (b), respectively. The three solid vertical lines shown in Fig. 20 represent the locations of the r-θ planes.

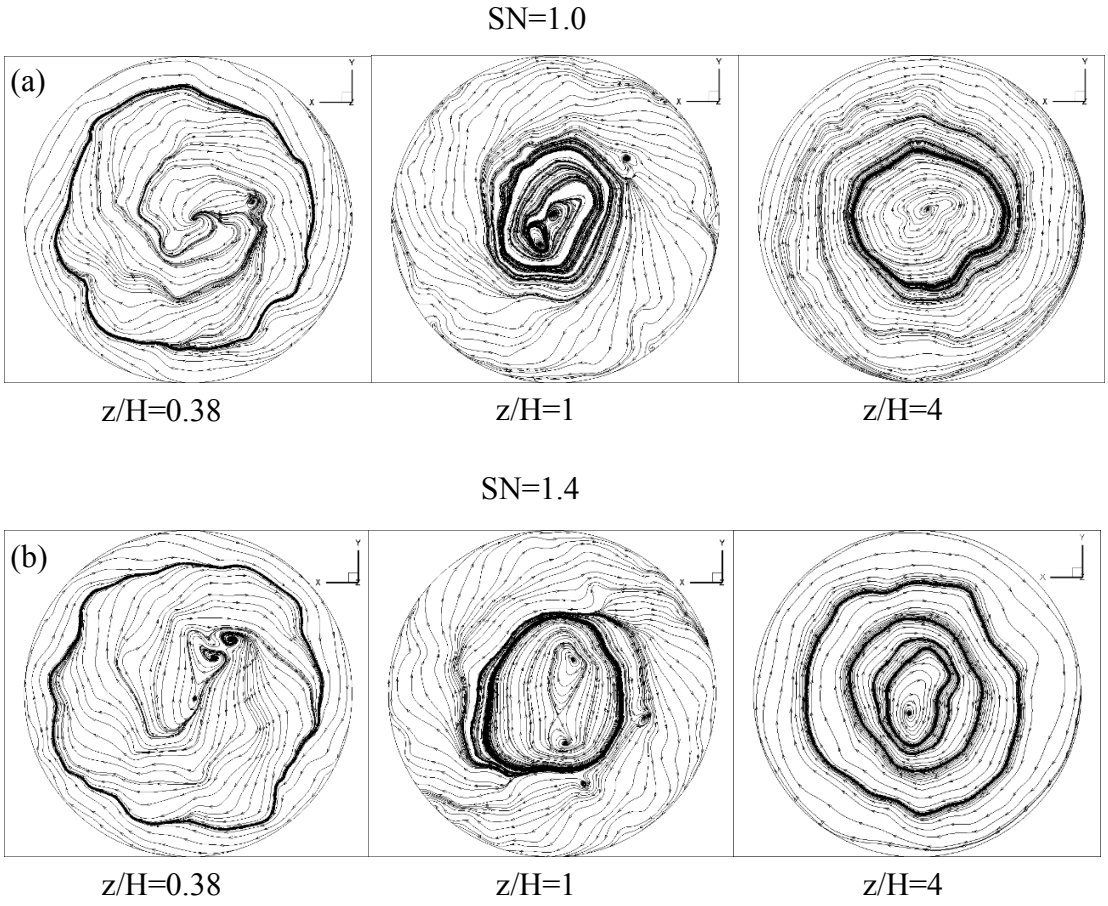

Fig. 21. Streamlines at the *r-θ* planes of *z/H= 0.38*, *z/H=1*, and *z/H=4* on (a) *SN* of *1.0* (b) *SN* of *1.4*

In turbulent flow, the vortices are convected downstream where their strength diminishes and directionally converged within the core region [17]. This leads to the generations of the processing vortex core. In Fig. 21(a) - (b), two kinds of processing vortex cores are observed, which are the spiral mode and double-helix mode. At the location (z/H) of *0.38*, two vortex cores are generated for both *SN* of *1.0* and *1.4* due to the combined effect of the induced helical flow and wake flow. At the location (z/H) of *1*, two vortex cores are found spiraling around the centerline, which means the helical

flow and wake flow can still be found in the fluid flow, but the effect of wake flow starts to reduce due to the shear friction between the two vortex cores. Because the swirler on a high swirl number generates greater angular momentum, the two cores for *SN* of *1.0* are closer to each other than at a *SN* of *1.4*. At the location (z/H) of *4*, the two vortex cores disappear, and a single vortex core appears as a single spiral around the center line due to the diminished effect of the wake flow. The same behavior can be seen in Fig. 19, which shows that the diameter of the center of recirculation zone suddenly reduces near *z/H* of *4*. The next section provides additional visual representation of the vortices by using the Q-criterion approach.

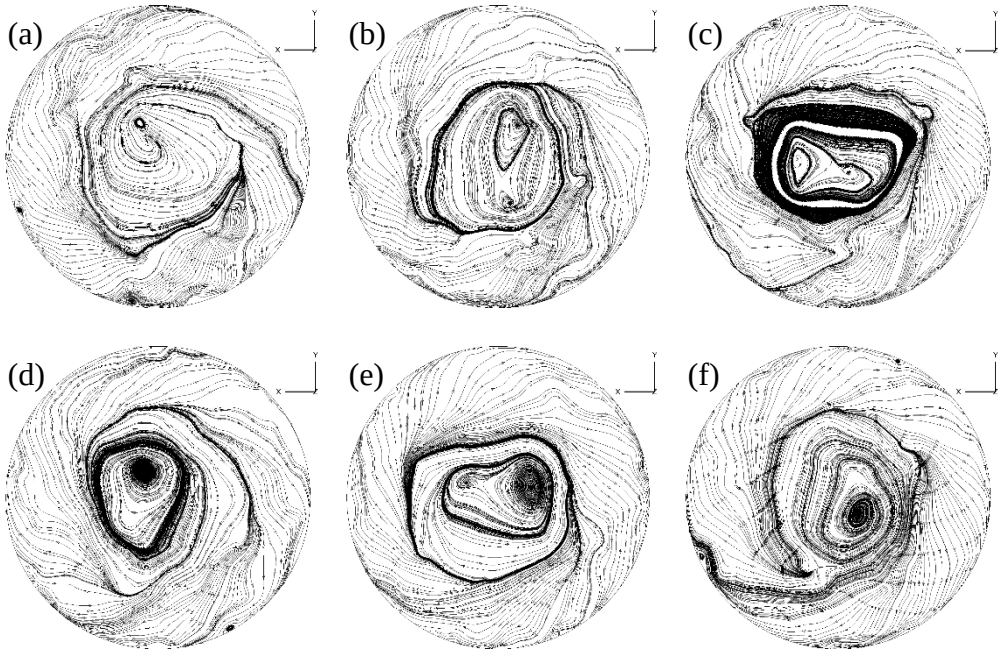

Fig. 22. Instantaneous streamlines at the *r-θ* planes (*z/H)* of *1* when *SN* is *1.4* at time of (a) *450* ms, (b) *500* ms, (c) *550* ms, (d) *600* ms, (e) *650* ms, (f) *700* ms

Fig. 22(a)-(f) show the instantaneous streamlines when *SN* is *1.4* at the *r-θ* planes (*z/H*) of *1* at times of *450* ms to *700* ms. The double-helix mode can be observed at time of 500 ms, 550 ms, and 650 ms. It shows that the wake flow affects the *r-θ* planes (*z/H*) of *1* alternatively. Fig. 23(a)-(f) show the instantaneous streamlines when *SN* is *1.4* at the *r-θ* planes (*z/H*) of *4* at times of *450* ms to *700* ms. Only spiral mode vortex can be observed due to the diminished effect of the wake flow. The results are consistent with the findings seen in Fig. 21.

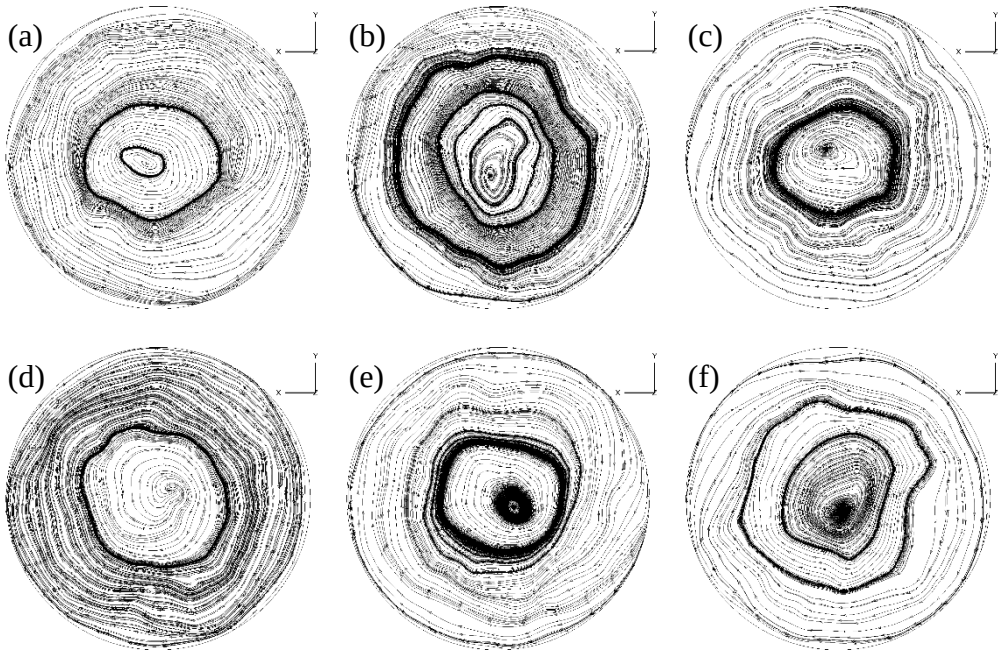

Fig. 23. Instantaneous streamlines at the *r-θ* planes (*z/H)* of *4* when *SN* is *1.4* at time of (a) *450* ms, (b) *500* ms, (c) *550* ms, (d) *600* ms, (e) *650* ms, (f) *700* ms

4.2.3. Effects of swirl number on vorticity profile

Turbulent flow is very complicated because it includes momentum diffusion and convection, rapid variation of pressure and velocity in space and time. All of these factors generate very complex vortices. Vorticity has a direct effect on the flow field of air and the fuel droplet distribution. Therefore, it is very important to understand the induced vorticity profile to understand its effects on combustion.

In general, there is no universal threshold to fully identify vorticity. Several criteria have been developed to identify vorticity within turbulent flow. These include *Q*, λ_2 and Δ criteria. Compared to others, Q-criterion is used to identify vortices within the flow regions by using the positive second invariant of ∇v, as follows [70]:

$$Q = \frac{1}{2}\left(\|\Omega\|^2 - \|S\|^2\right) \tag{58}$$

Where

$$\|\Omega\| = tr\left[\Omega\Omega^t\right]^{1/2} \tag{59}$$

$$\|S\| = tr\left[SS^t\right]^{1/2} \tag{60}$$

$$\Omega = \frac{1}{2}\left(\nabla\upsilon - (\nabla\upsilon)^t\right) \tag{61}$$

$$S = \frac{1}{2}\left(\nabla\upsilon + (\nabla\upsilon)^t\right) \tag{62}$$

The Q-criterion is a local measure of the excess rotation rate relative to the strain rate [70]. It provides an approach to visualize vortices by extracting specific information from the flow field.

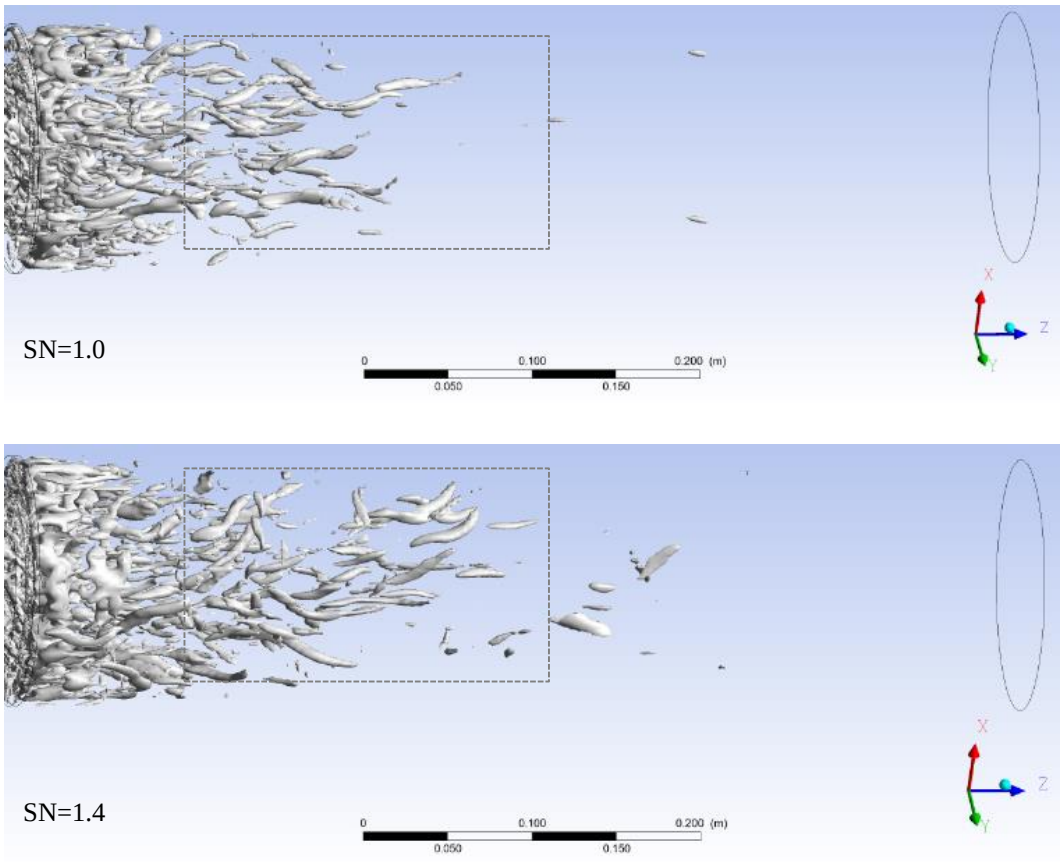

Fig. 24. Snapshot of the iso-surface based on Q-criterion (Q= *10000* s^{-2}) at flow time of *500* ms

Fig. 24 shows a snapshot of the iso-surface based on the Q-criterion at *10000* s^{-2} at flow time of *500* ms. It can be seen that there is a greater number of vortices with high intensity (Q= *10000* s^{-2}) downstream from the swirler when *SN* is set at *1.4* than when *SN* is *1.0*, especially in the upper layer of the downstream region. According to the velocity and turbulent kinetic energy profiles, the values of velocity and turbulent kinetic energy for *SN* of *1.4* are greater than for *SN* of *1.0*. This implies that the intensity of the vortices for *SN* of *1.4* is greater than for *SN* of *1.0*. As shown in Fig. 24, the distribution

of vortices with high intensity is wider when *SN* is *1.4*. Furthermore, the vortices in the downstream appear to have greater curvature when *SN* is set at *1.4*. This is a reflection of the reverse flow present within the region of interest. The direction and intensity of vortices also have an effect the distribution of fuel droplets. This will be discussed in the next section.

Fig. 25(a)-(d) shows a snapshot of the iso-surface based on the Q-criterion at *10000* s^{-2} when *SN* is *1.4* at flow time of *300* ms to *600* ms. It shows that the vortices with high intensity develop on the downstream with time. It also shows that the vortices in the downstream region appear to have greater curvature at different flow times.

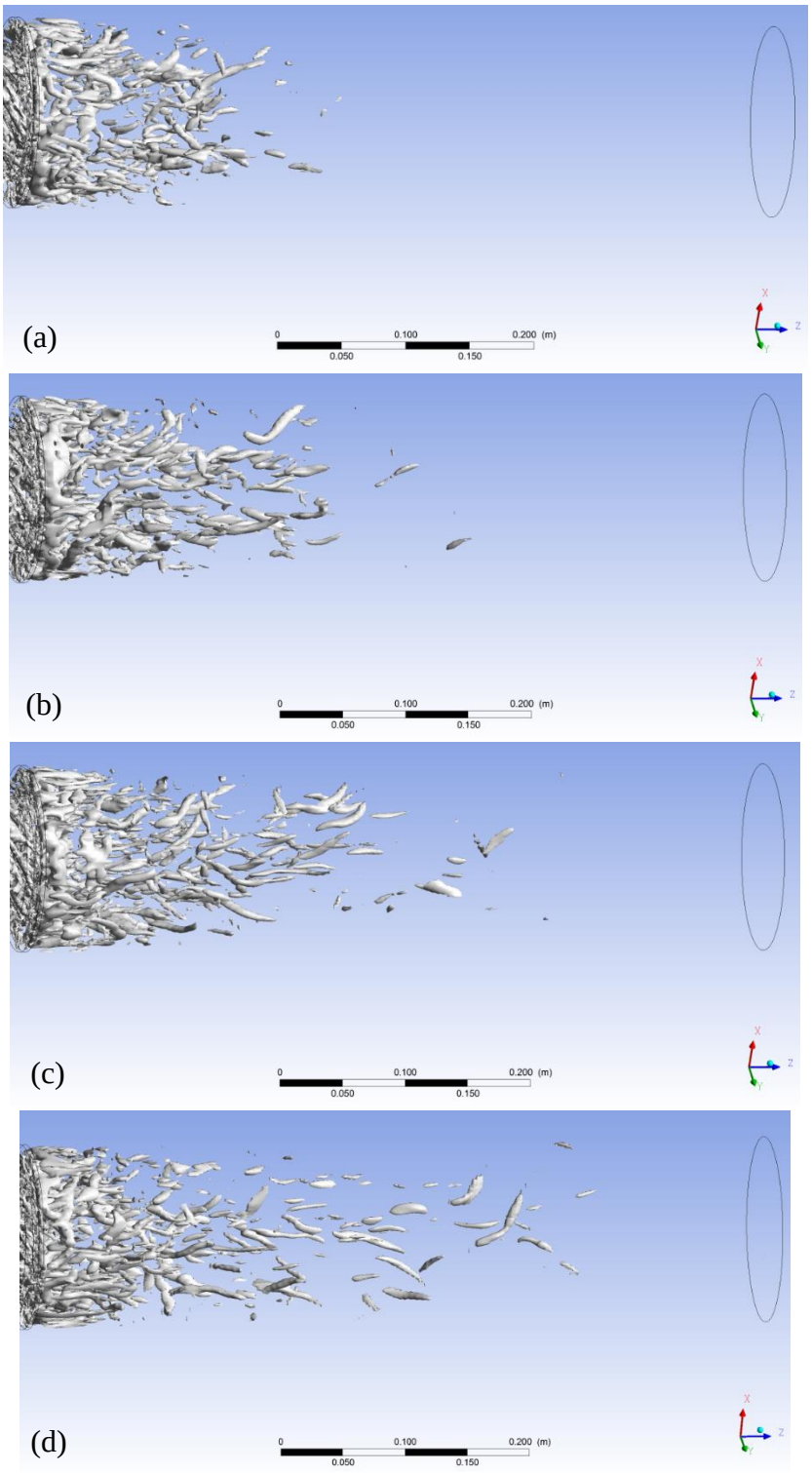

Fig. 25. Snapshot of the iso-surface based on Q-criterion (Q= *10000* s^{-2}) when *SN* is *1.4* at flow time of (a) *300* ms, (b) *400* ms, (c) *500* ms, and (d) *600* ms

4.3. Fuel droplet distribution in combustion chamber

4.3.1. Validation of fuel droplet distribution in combustion chamber

In this study, a combustion chamber where liquid hydrocarbon fuel is introduced via a fuel nozzle has been chosen for simulation and analysis. In convectional arrangements, the liquid fuel exits the injector in the form of a thin sheet and then breaks up into droplets. The distribution of droplets depends on the fuel properties, type of atomizer, and the turbulence of the surrounding gas phase.

In order to validate the numerical algorithm described in Chapters 2 and 3 for fuel droplet distribution with swirl promoted flow, an experimental data set based on the fuel droplet distribution of kerosene by Jones et al. [66] was used for validation purposes.

The experimental setup used by Jones et al. [66] is shown in Fig. 26. It consists of a guiding pipe, a swirl generator, a pressure jet atomizer, and a sudden expansion chamber. The inlet bulk velocity is *15.6* m/s. The swirling flow is generated by the swirler with *20* equally spaced vanes, and the discharge or inclination angle set at *30°* with respect to the axis.

The fuel injector is located in an annular duct *50* mm downstream of the front plate of the swirler, and the diameter of atomizer is *0.25* mm. The fuel flow rate is *0.000951* g/s and the air-to-fuel ratio is *27.88*. The kerosene droplets are injected into the chamber at a spray angle of *74°*.

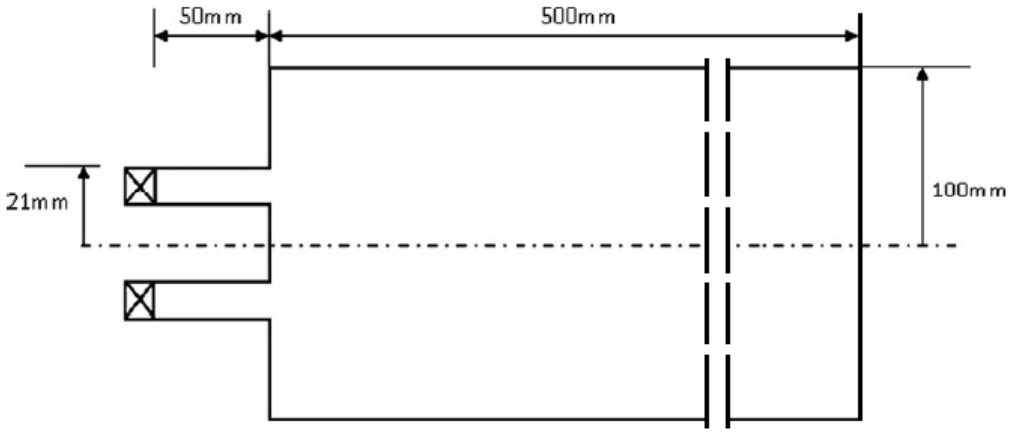

Fig. 26. Schematic of the combustor chamber by Jones et al. [66]

A computational mesh for the combustion chamber used by Jones et al. [66] was generated by ANSYS ICEM CFD following the same approach as explained above using a combination mesh, as shown in Fig 27. The numerical solution was obtained using ANSYS Fluent 15.0. The turbulent flow simulation procedure is the same as described in section 4.1. The Discrete Phase model was used to generate the fuel droplet when the LES model was applied. The Stochastic and TAB models were used to take into account the dispersion and breakup of droplets. For the computational solution methods, the PRESTO scheme was used for taking into account and solving pressure-velocity coupling, using a second order upwind scheme. Spatial discretization of pressure, momentum, energy, and species were undertaken as prescribed by the algorithm. The time interval was 10^{-6} s, and simulation data were collected for 20×10^{-3} s.

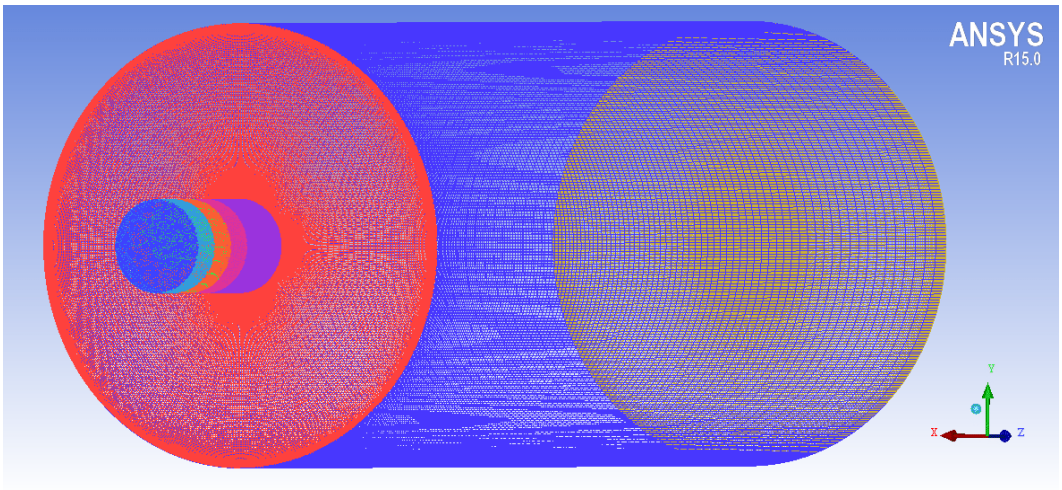

Fig. 27. Computational mesh for droplet spray validation

Fig. 28 shows the simulation and experimental results of droplet size-velocity correlation at the crossing surface *z* of 5*0* mm in the combustion chamber based on Jones et al. study [66]. The shaded region represents the area where all the experimental data points of Jones et al. [66] can be found. The simulation results, which were obtained following the steps outlined above, show a good agreement with the experimental data. Therefore, the numerical approach can be applied to simulate the behavior of fuel droplets in a combustion chamber.

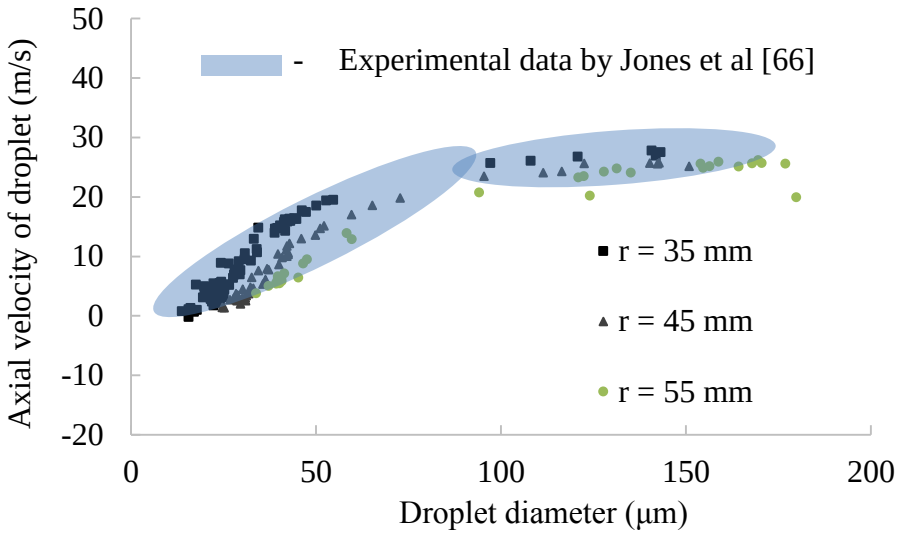

Fig. 28. Droplet axial velocity for different droplet sizes at three radial positions (r) at an axial position (x) of 50 mm [66]

4.3.2. Emulsified canola oil droplet distribution within swirl-promoted turbulent cold flow in combustion chamber

In order to understand the combustion process and emissions of emulsified canola oil, the effects of swirl-promoted turbulent flow on fuel droplet distribution needs to be studied carefully. In this section, the numerical results for the effects of swirl number and equivalence ratio (ϕ) on droplet distribution are analyzed by taking into account droplet size, spatial and velocity distribution in the combustion chamber, respectively.

For the numerical studies, the simulation domain is shown in Fig. 2. The flow condition has been shown in Table 1 with ϕ of *0.81* and *0.97* on *SN* of *1.0* and *1.4*, respectively. The thermophysical properties of emulsified canola oil are shown in Table

3. The computational mesh as shown in Fig. 16, was generated by ANSYS ICEM CFD. The numerical approach for simulation is the same approach as explained above.

Fig. 29(a)-(c) shows fuel droplets spatial distribution for *SN* of *1.4* and ϕ of *0.81* at time of *40* ms to *60* ms, respectively. It can be observed that the shape of droplets distribution at different time is similar. When time increases, the droplets become more dispersed downstream in the combustion chamber. The distribution of fuel droplets highly depends on the distribution of vortices, which is also observed by Jones et al. [39]. In Fig. 24 and 25, the distribution of vortices show an asymmetrical profile in the downstream side, which leads to the fuel droplets spatial distribution in Fig. 29.

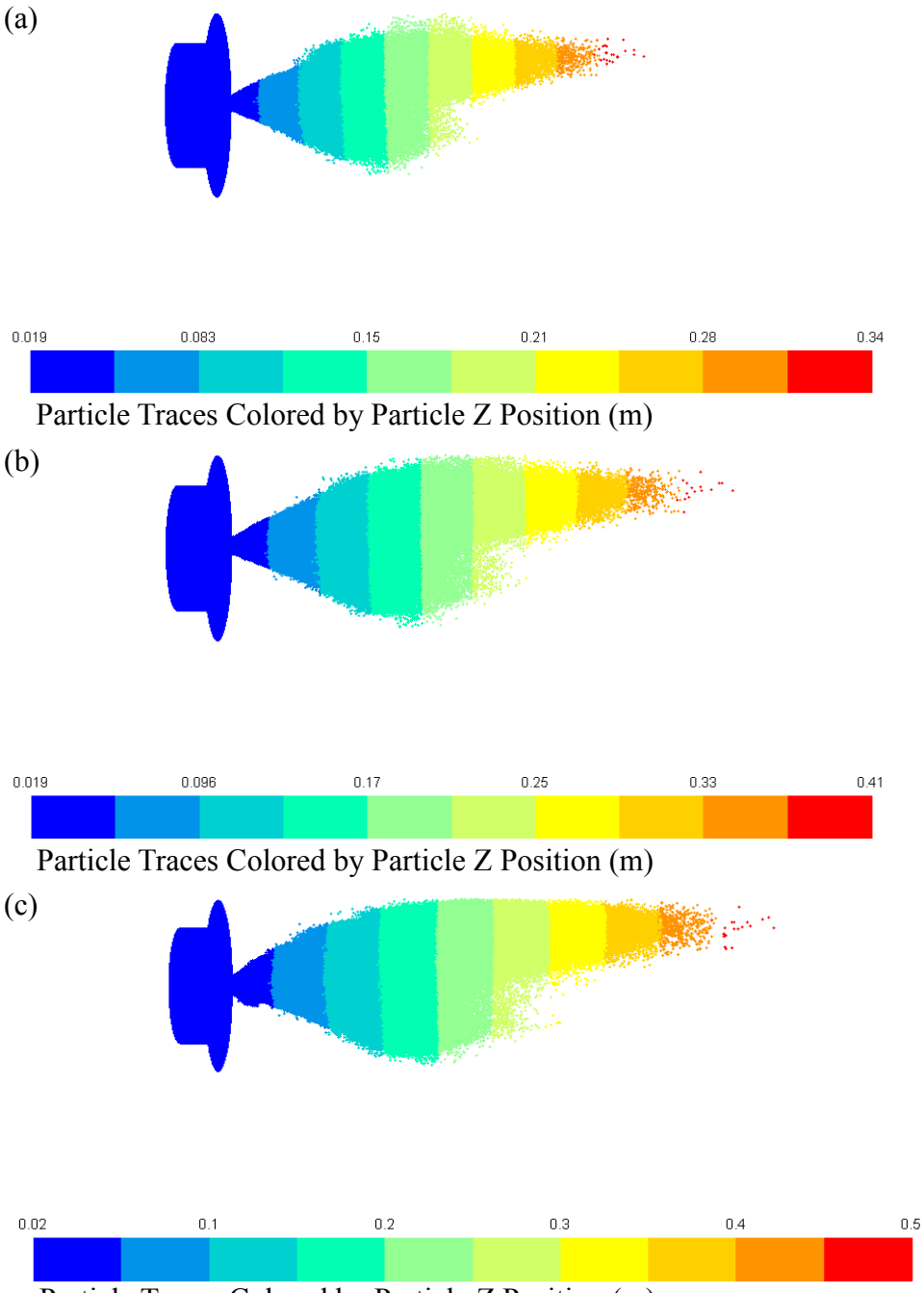

Fig. 29. Fuel droplets spatial distribution for *SN* of *1.4* and ϕ of *0.81* at time of (a) *40* ms, (b) *50* ms, (c) *60* ms

As explained in Fig. 20, the vortices breakdown on the downstream side of the combustion chamber. According to the study of P. Billant et al. [71], the instabilities of breakdown may result from the streamwise shear stress (Kelvin-Helmholtz-like instabilities) or from centrifugal instabilities due to the azimuthal motion, or more probably from a combination of both. Kelvin-Helmholtz-like instabilities induce roll-up of the helix in the streamwise direction, thereby leading to a disorganization of the whole pattern farther downstream [71]. Moreover, since the swirl-promoted flow in the combustion chamber is rotating, it is also subjected to centrifugal instabilities. This azimuthal motion can be viewed as a loss of symmetry. Based on the Rayleigh's criterion, centrifugal flow can become unstable if $1+C_\theta<0$, where $C_\theta=\frac{r}{u_\theta}\frac{du_\theta}{dr}$.

Therefore, centrifugal flows are expected to become unstable when the tangential velocity decreases with respect to the radius of rotation [72]. As shown in Fig. 17(b), the tangential velocity profile shows this trend in the outside region of the core area of the combustion chamber. Therefore, the combination or competition between Kelvin–Helmholtz-like instability and the generalized centrifugal instability leads to the asymmetrical distribution of vortices and the corresponding droplets distribution.

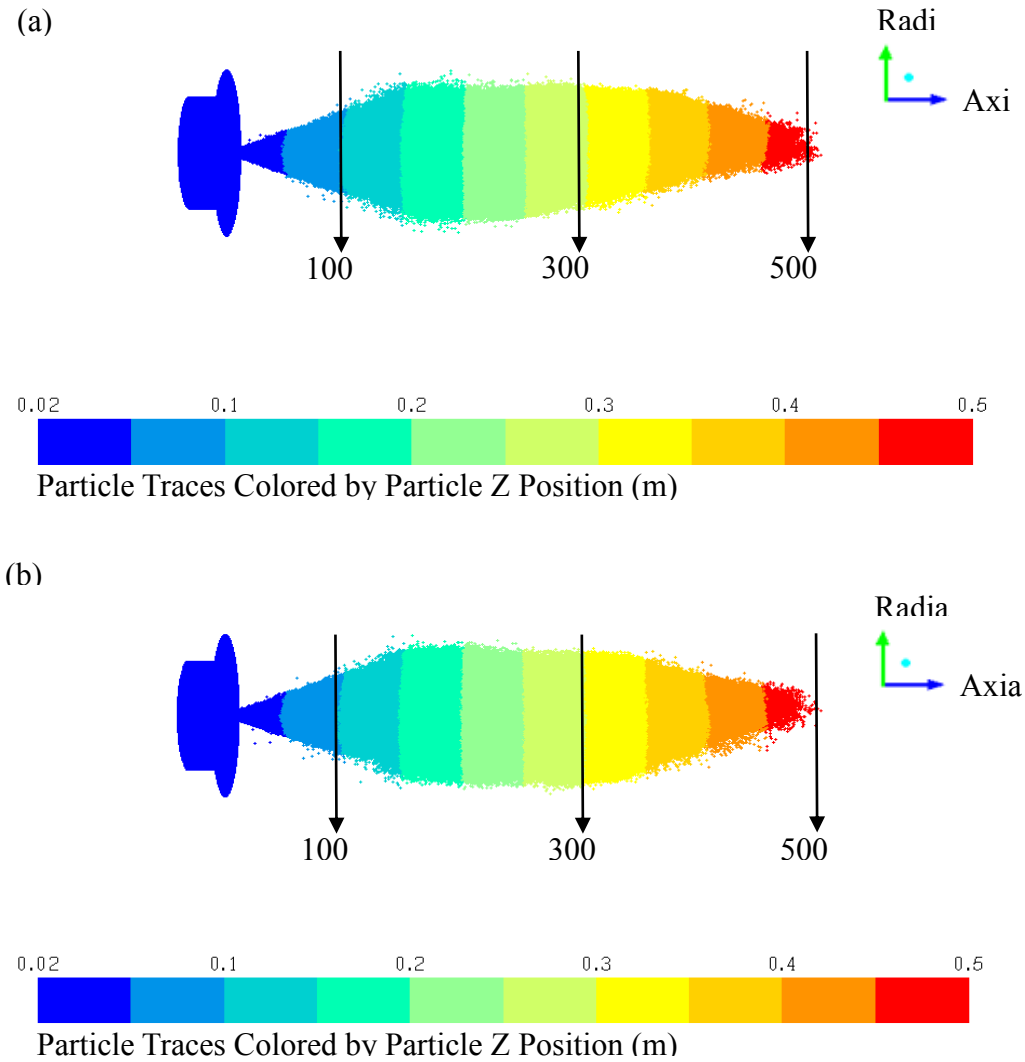

Fig. 30. Fuel droplets spatial distribution on *SN* of *1.0* in *60* ms (a) ϕ of *0.81*, (b) ϕ of *0.97*

Fig. 30(a) and (b) shows the numerical results of fuel droplet spatial distribution for ϕ of *0.81* and *0.97* for *SN* of *1.0* after *60* ms without combustion, respectively. When the droplet particles were injected out of nozzle, the shape of the spray shows a cone-like distribution in the upstream side of the chamber. Then, the fuel droplets tend to

accumulate in the upper layer on the downstream side of the chamber. According to Table 1, the equivalence ratio is based on air and fuel flow rates, but since the fuel flow rate is fixed, lower equivalence ratios represent higher air flow rate. Therefore, lower equivalence ratios imply greater turbulence within the combustion chamber. Due to the greater intensity of turbulence when equivalence ratio is *0.81*, more fuel droplets accumulated in the upper layer of chamber at that equivalence ratio. In Fig. 30, the scale illustrates the axial location of fuel droplet. By comparing the value of axial location in Fig. 30(a) and (b), it can be found that the effects of equivalence ratio on droplet distribution in the streamwise direction is not significant when *SN* is *1.0*.

Fig. 31 shows the fuel droplet spatial distribution for ϕ of *0.81* and *0.97* for *SN* of *1.4* after 60 ms without combustion. The effects of equivalence ratio on droplet spatial distribution is more significant when *SN* is *1.4*. Due to the greater angular momentum at ϕ of *0.81*, the sprays in the streamwise direction is shorter than when the equivalence ratio is set at *0.97*, and most of the fuel droplets tend to accumulate in the upper layer of the chamber. Moreover, the effects of swirl number on fuel droplets spatial distribution can be studied by comparing Fig. 30(a) and Fig. 31(a). In Fig. 31(a), the maximum scale is *460* mm, but the maximum scale is *510* mm as shown in Fig. 30(a). This implies that the droplets are less dispersed in the streamwise directions when *SN* is *1.4*. In section 4.2.3, it is concluded that the fluid flow when *SN* is set at *1.4* generates more reverse flow from downstream side to upstream side. Hence, droplets in the downstream side have a higher probability of getting sucked back into the upstream side, which makes the spatial distribution of fuel droplets more concentrated at *SN* of *1.4*.

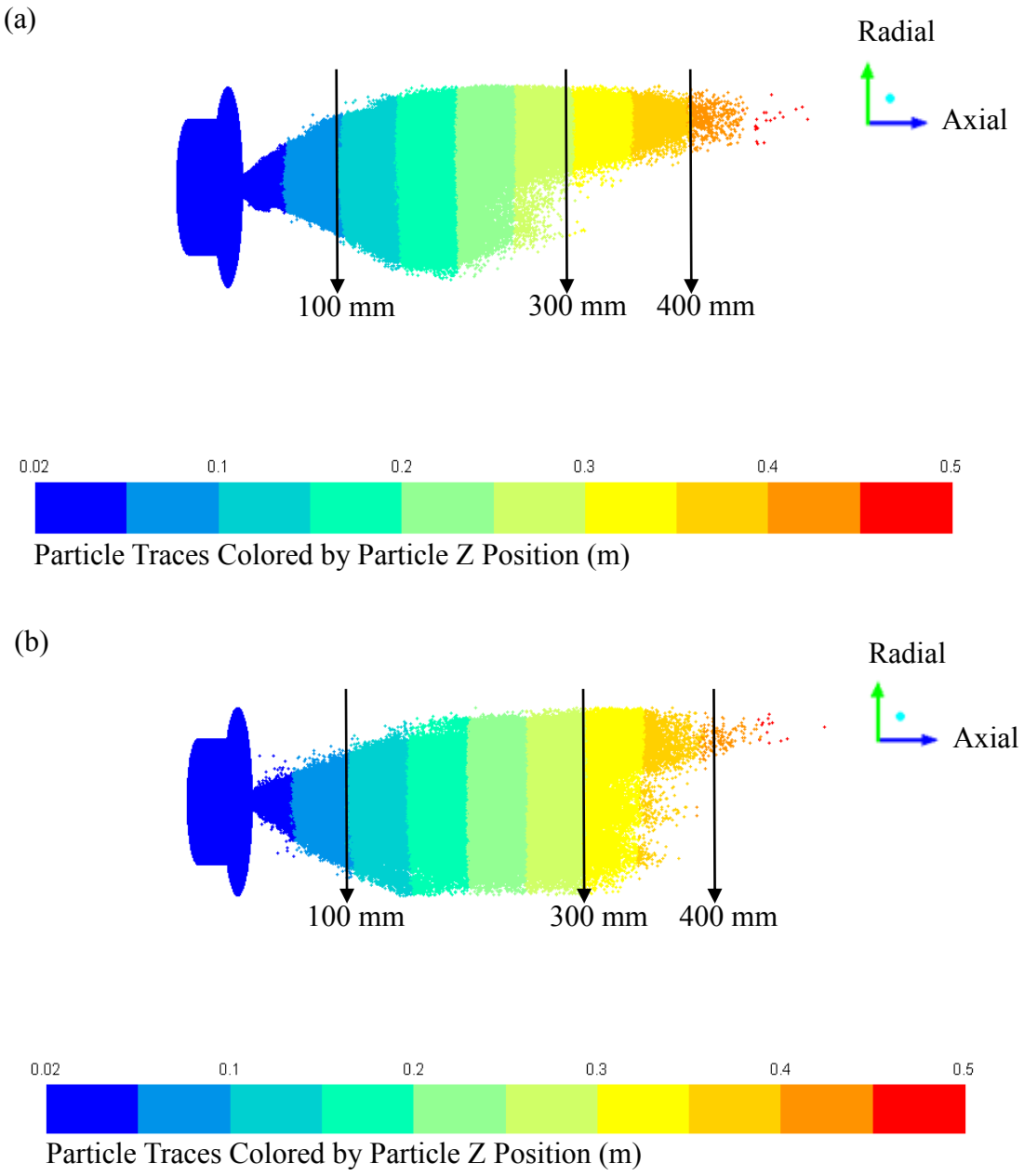

Fig. 31. Fuel droplets spatial distribution on *SN* of *1.4* in *60* ms (a) ϕ of *0.81*, (b) ϕ of *0.97*

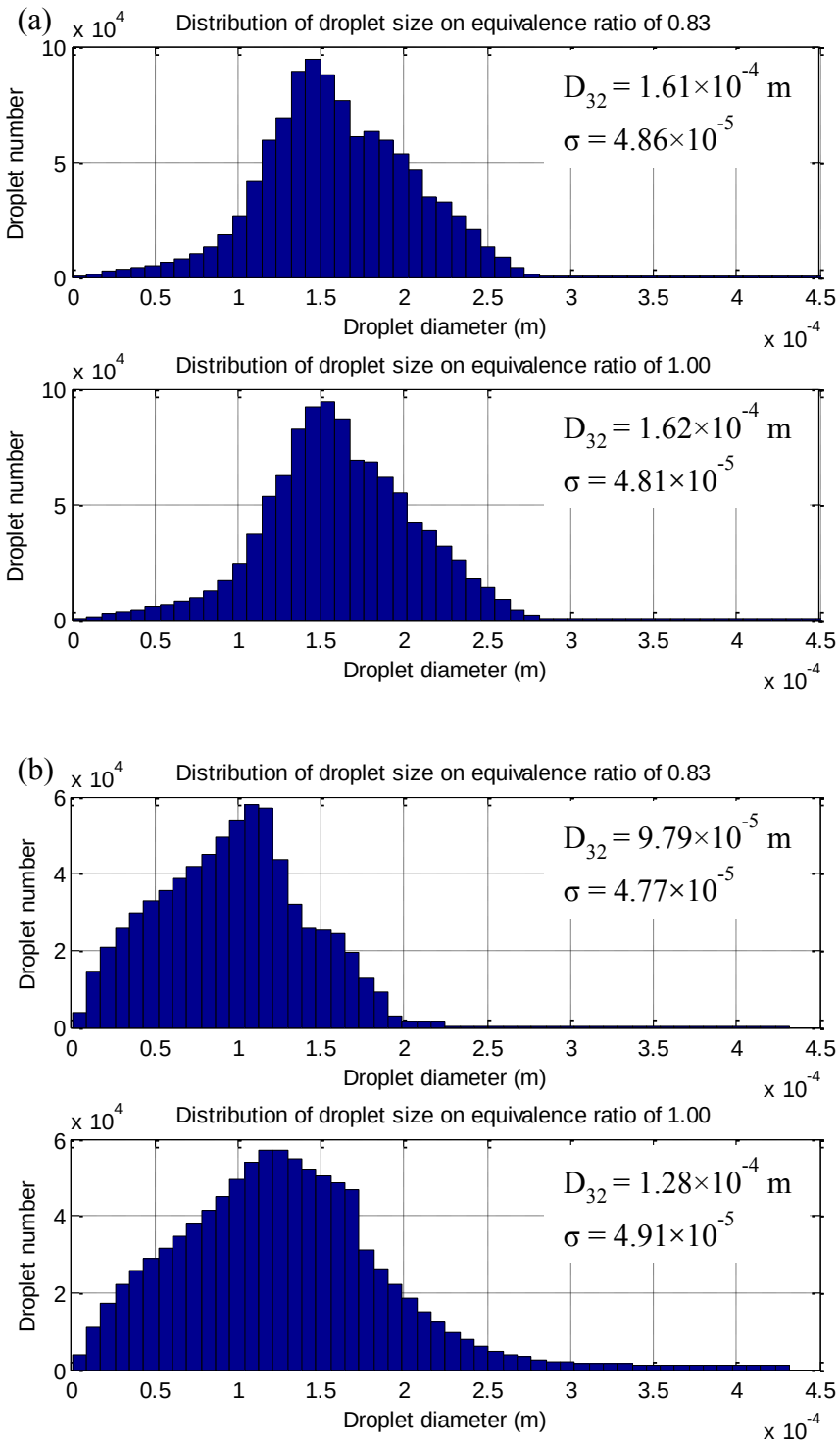

Fig. 32. Histogram of droplet size distribution on ϕ of *0.81* and *0.97* when (a) swirl number is *1.0*, (b) swirl number is *1.4*

Fig. 32(a) and (b) display the histograms of droplets size distribution for ϕ of *0.81* and *0.97* when *SN* of *1.0* and *1.4*, respectively. Fig. 32(a) and (b) show that the air flow at ϕ of *0.81* is capable of generating smaller size of fuel droplets when *SN* is *1.0* and *1.4*, but the effect of equivalence ratio on droplets size distribution is not significant. As shown in Fig. 32(a) and (b), the size of droplets for *SN* of *1.4* is smaller than that on *SN* of *1.0*, and the distribution of droplets size for *SN* of *1.4* is more concentrated than that for *SN* of *1.0.* According to the discussion in the section 4.2.3, the intensity of turbulence for *SN* of *1.4* is greater than for *SN* of *1.0*. Hence, the forces which act on the fuel droplet are greater when *SN* is *1.4* than the forces when *SN* is *1.0*. The greater forces, specifically drag force, facilitate the breakup of big droplets into small droplets easily, which leads to a finer droplet size distribution at *SN* of 1.4.

Fig. 33(a) and (b) illustrate the time-averaged droplet axial velocity profiles for ϕ of *0.81* and *0.97* for *SN* of *1.0* at axial locations of *100* mm, *300* mm, and *500* mm, respectively. The axial locations have been shown in Fig. 30. Fig. 33(a) and (b) show that the droplet axial velocity for an equivalence ratio of *0.81* is not as stable as for a ϕ of *0.97*. The high flow rate of air at ϕ of 0.81 leads to variations in the axial velocity of fuel droplets due to greater intensity of turbulence flow as seen in Fig. 33(a). Moreover, the droplets distribution in the spanwise direction is wider for ϕ of *0.81* than that for an equivalence ratio of *0.97*.

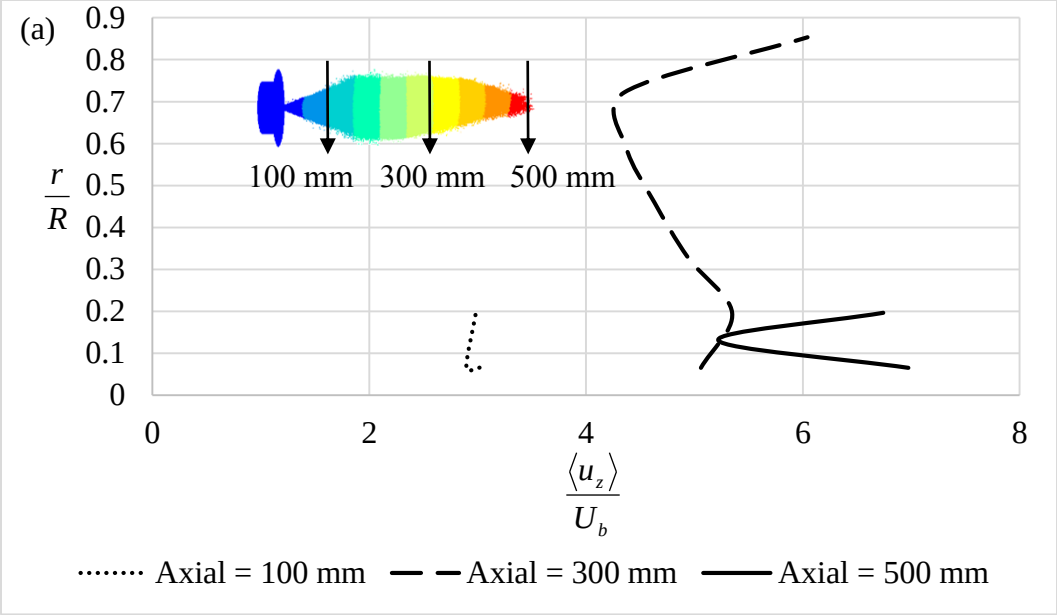

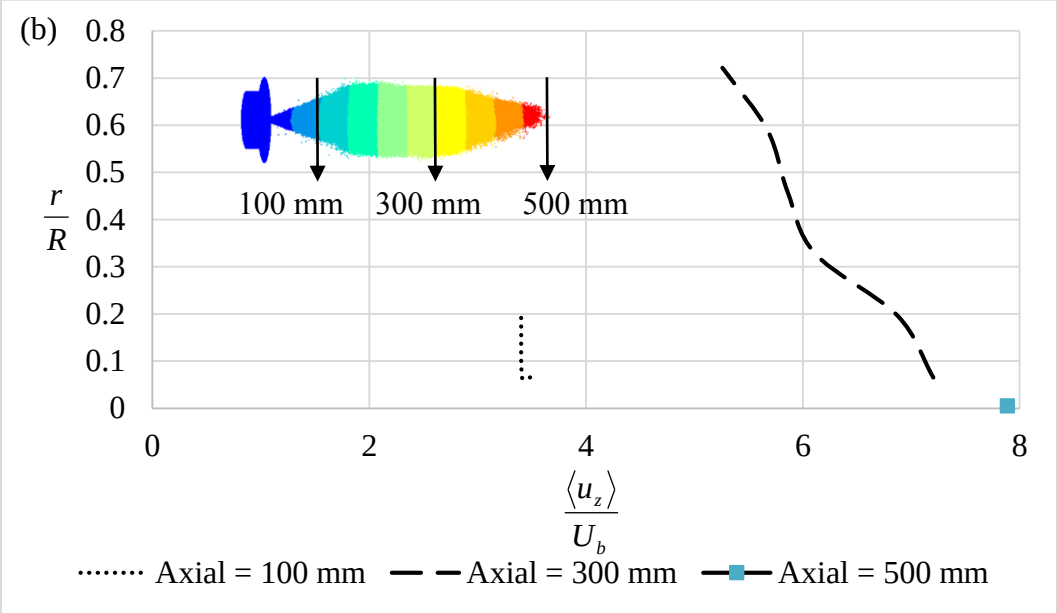

Fig. 33. Time-averaged droplet axial velocity profiles of *SN* of *1.0* at three axial locations for (a) ϕ of *0.81*, (b) ϕ of *0.97*

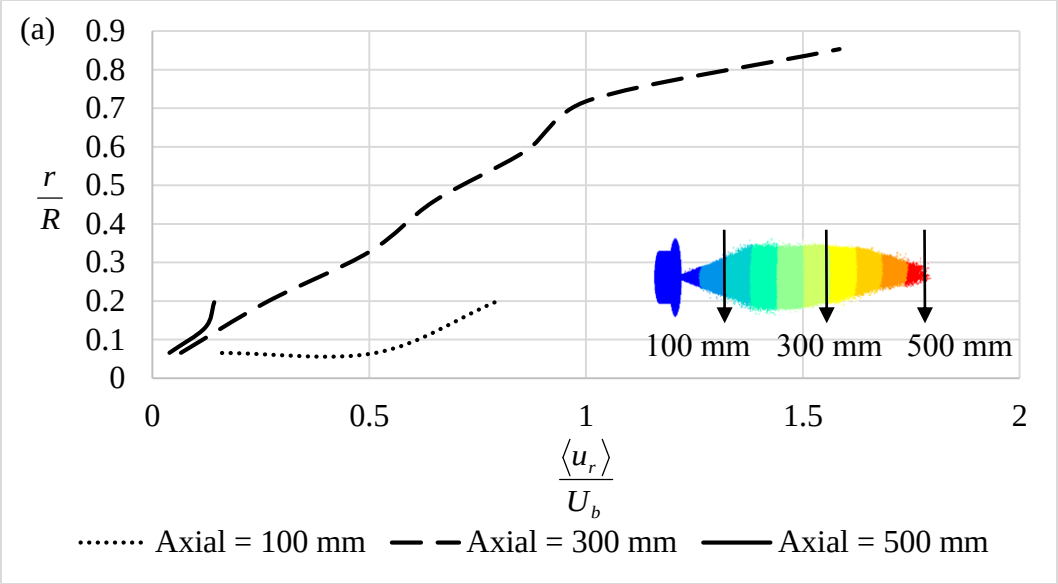

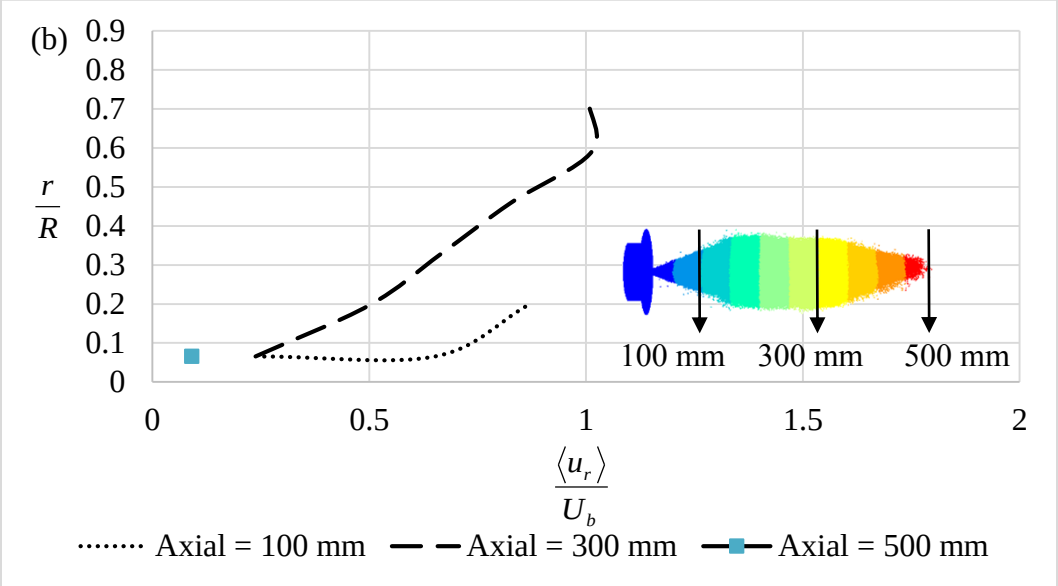

Fig. 34. Time-averaged droplet radial velocity profiles of *SN* of *1.0* at three axial locations on (a) ϕ of *0.81*, (b) ϕ of *0.97*

Fig. 34(a) and (b) display the time-averaged droplet radial velocity profiles for ϕ of *0.81* and *0.97* at a *SN* of *1.0* at three axial locations, respectively. It shows that the droplets at a ϕ of *0.81* exhibit much higher radial velocity in the middle of combustion

chamber, and the distribution of droplet is wider when equivalence ratio is *0.81*. This suggests that at higher flow rate, there is a tendency for droplets to flow radially, which lead to a stronger reverse flow within the combustion chamber.

Fig. 35 and 36 show the time-averaged droplet axial and radial velocity profiles for *SN* of *1.0* and *1.4* at a ϕ of *0.81* at three axial locations of *100* mm, *300* mm, and *400* mm, respectively. The axial locations have been shown in Fig. 30 and 31. As shown in the figures, the time-averaged axial and radial velocity of droplets at *SN* of *1.4* is smaller than that for *SN* of *1.0*, especially in the radial direction. This can be explained by the fact that the droplet sizes at *SN* of *1.4* are smaller than at *SN* of *1.0*. Conceptually, small droplets lose their momentum more rapidly than larger droplets in a turbulence flow field [65], which should lead to low droplet velocity at *SN* of *1.4*. Furthermore, fuel droplets at *SN* of *1.4* shows a stronger tendency to accumulate in the upper layer on the downstream side of the chamber, which can be observed at the axial location of *400* mm. Also, the velocity fluctuation at *SN* of *1.4* is greater than that at *SN* of *1.0*.

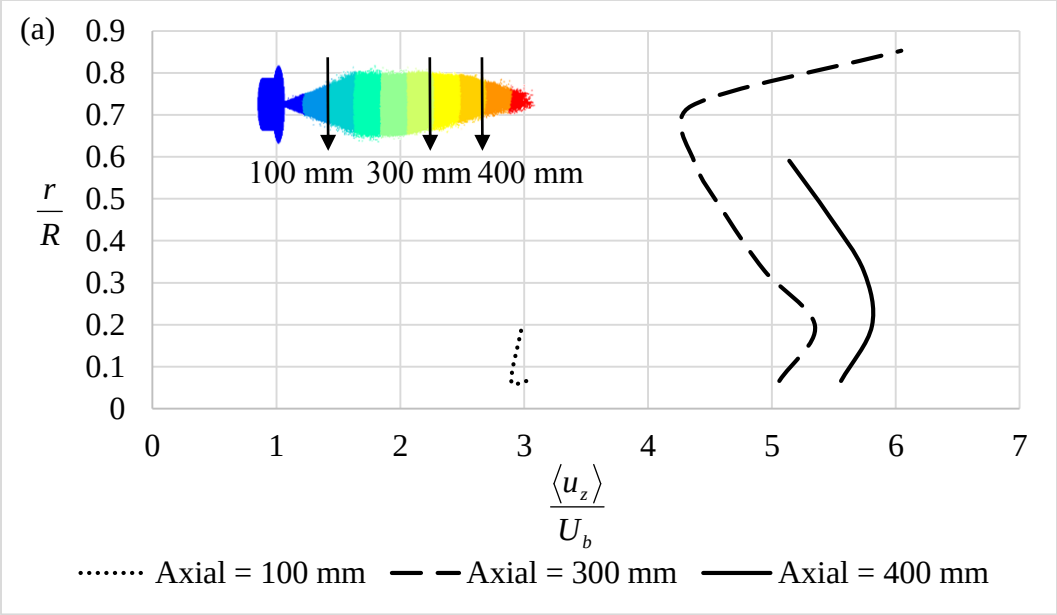

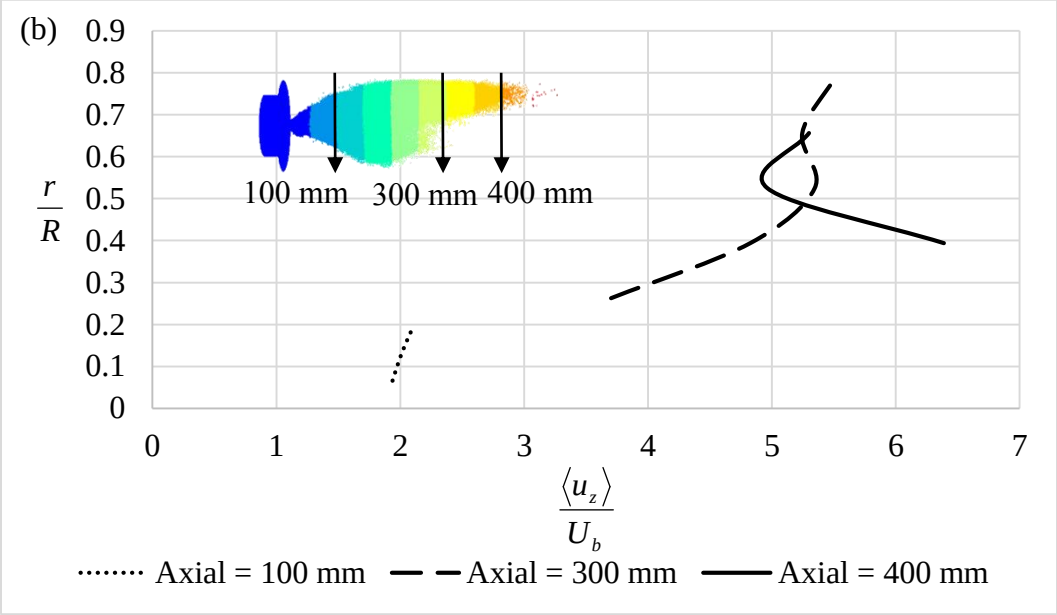

Fig. 35. Time-averaged droplet axial velocity profiles of ϕ of *0.81* at three axial locations on (a) *SN* of *1.0*, (b) *SN* of *1.4*

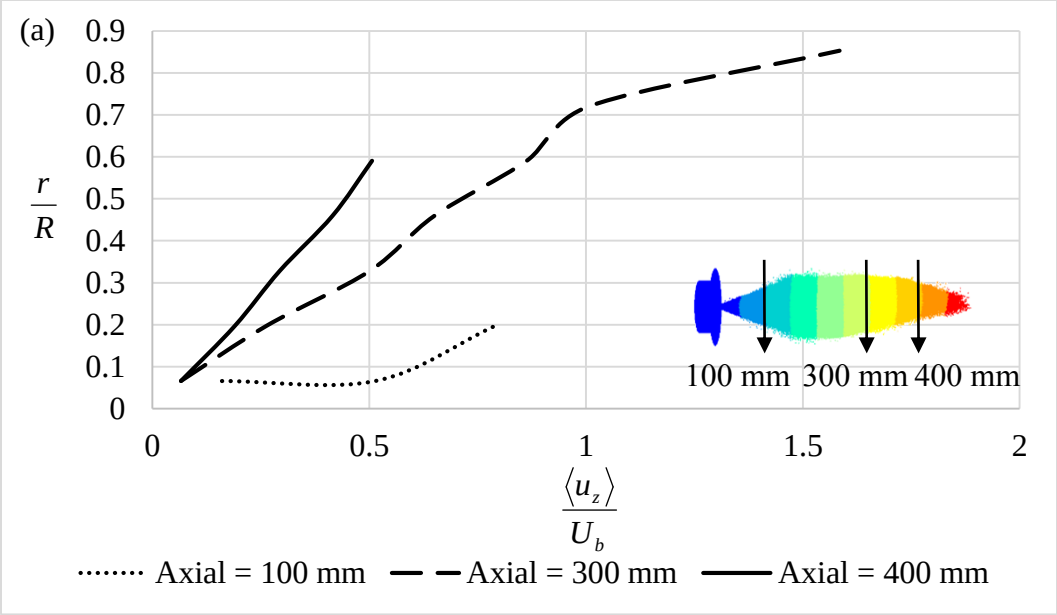

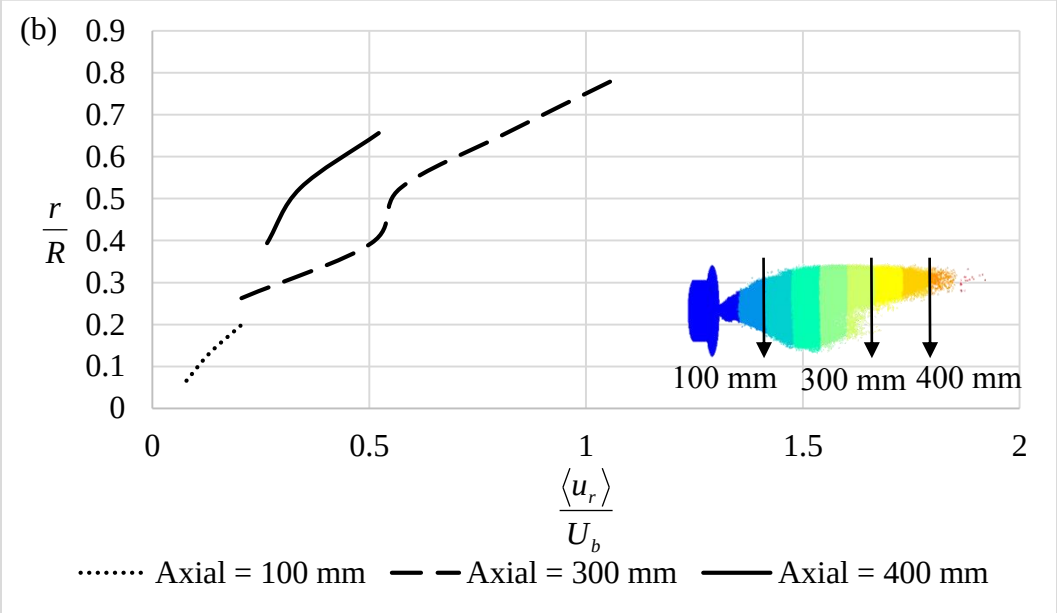

Fig. 36. Time-averaged droplet radial velocity profiles of ϕ of *0.81* at three axial locations on (a) *SN* of *1.0*, (b) *SN* of *1.4*

5. FLOW AND COMBUSTION OF SWIRL-PROMOTED FLOW OF EMULSIFIED CANOLA OIL USING LES-BASED NUMERICAL SCHEME

When combustion takes place in a combustion chamber, the chemical reactions will generate different types of emissions, including *CO* and NO_x. Furthermore, the chemical reactions lead to high velocity of combustion products, which affects the profile of turbulent flow field significantly. Therefore, the structure of the turbulent flow field and the corresponding vortices profile during the combustion should be analyzed to understand the effects of both physical mechanisms on the generation and distribution of emissions within the combustion chamber. In this chapter, the chosen numerical approach for combustion simulation was validated using experimental results from Jones et al. [47]. The turbulence kinetic energy and vortices profiles during the combustion process are discussed by considering *SN* of *1.0* and *1.4* and the corresponding ϕ of *0.81* and *0.97*. The profiles of temperature and emissions are discussed by taking into account the effects of turbulent vortex flow.

5.1. Validation of numerically-based combustion scheme

In this study, the experimental work by Jones et al. [43] was selected to validate the numerical algorithm used to simulate liquid fuel combustion. The simulation results are compared with experimental results in terms of temperature and CO_2 profiles at a crossing plane with a fixed axial location.

The domain for the numerical approach is shown in Fig. 37, which is the same experimental setup used for the validation of droplet distribution, as described in the previous chapter. The fuel flow rate of kerosene was set at *0.000951* g/s and the equivalence ratio was *0.64*. The inlet air temperature in combustion chamber was maintained at *1000* K.

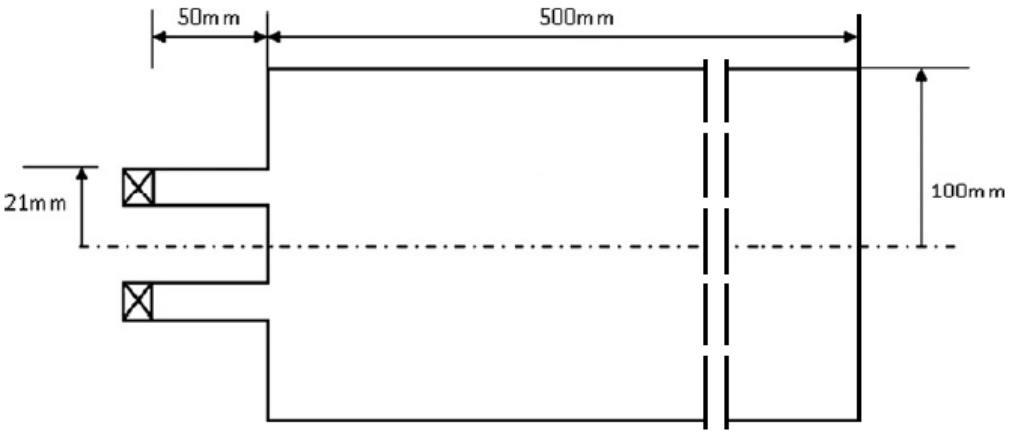

Fig. 37. Jones et al. experimental setup [43]

The computational mesh for the domain is shown in Fig, 38, which is based on the combination meshing technique explained in Chapter 3. The solution was solved using ANSYS Fluent 15.0. The numerical algorithms for turbulent flow and fuel droplet injection are the same as described in section 4.1 and 4.3, respectively. The mixture was ignited using a constant power of *0.1* W at the center of nozzle outlet for 5×10^{-5} s (0.05 ms), which combined with the initial combustion chamber temperature of 1000 K ensures complete ignition of the fuel mixture. The eddy dissipation model was used to

take into account the interaction between the chemical reaction of kerosene and the turbulent air flow. The global kinetic reaction mechanism was applied to simulate the chemical reaction in the combustion chamber. The chemical reaction is as follows:

$$C_{12}H_{23} + 17.75O_2 \Rightarrow 12CO_2 + 11.5H_2O$$

The pre-exponential constant A is 2.587×10^9, and the activation energy E is 1.257×10^5 J/kg-mole [62], which are used in the combustion simulation as explained in Chapter 3.

Spatial discretization of pressure, momentum, energy, and species were undertaken as prescribed in Chapter 3. The interval of each time step was set at 10^{-6} s (1 μs), and the simulation data were collected within 200×10^{-3} s (200 ms).

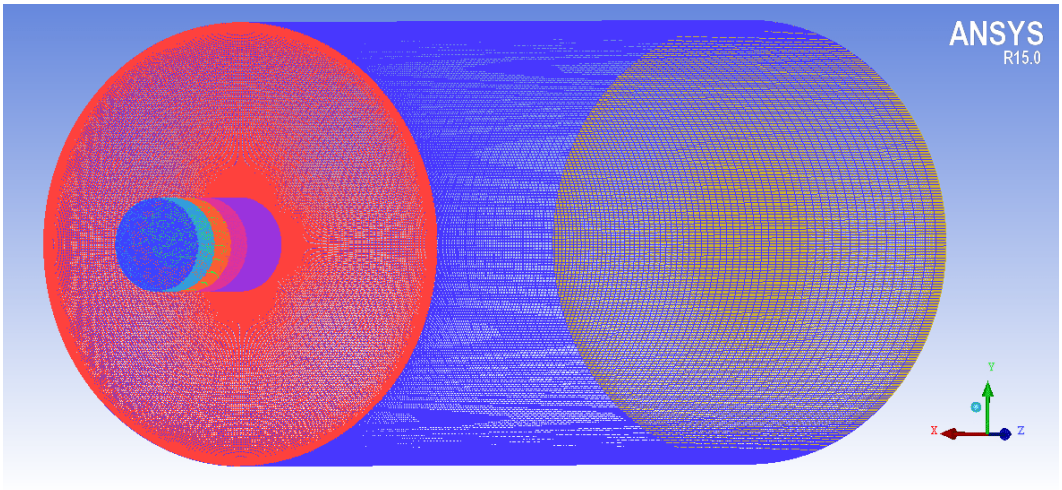

Fig. 38. Computational mesh used for combustion validation

Fig. 39 and 40 show the time-averaged temperature and CO_2 profiles of the simulation and experimental results at the axial location of *200* mm in the combustion chamber, respectively. In the experiments of Jones et al. [43], heat losses led to lower temperature profiles when compared with the simulation results, as shown in Fig. 39. Furthermore, Jones et al. [43] used a 4-step chemical reaction mechanism, while the current study was based on a global (1-step) chemical reaction mechanism. The simplified approach contributes somewhat to the difference between the simulation results of Jones et al. [43] with the current study, as shown in Fig.40. However, the simulation results show a reasonable agreement with the trend of the experimental and simulation data of Jones et al. [43]. Therefore, the numerical approach described above can be applied to simulate the combustion process of biofuels in the described combustion chamber.

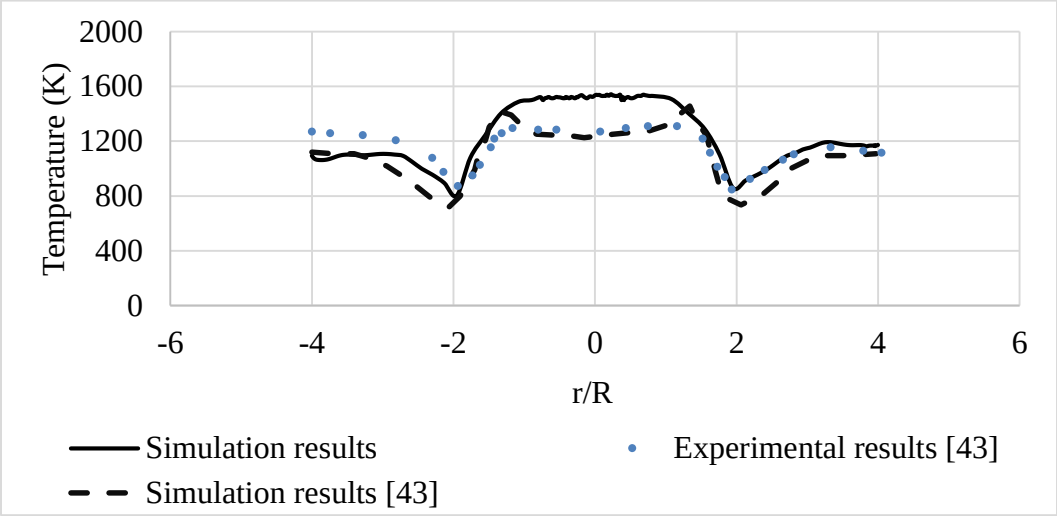

Fig. 39. Comparison of simulation results and experimental data [43] of the time-averaged temperature at an axial location of *z/R=2.0*

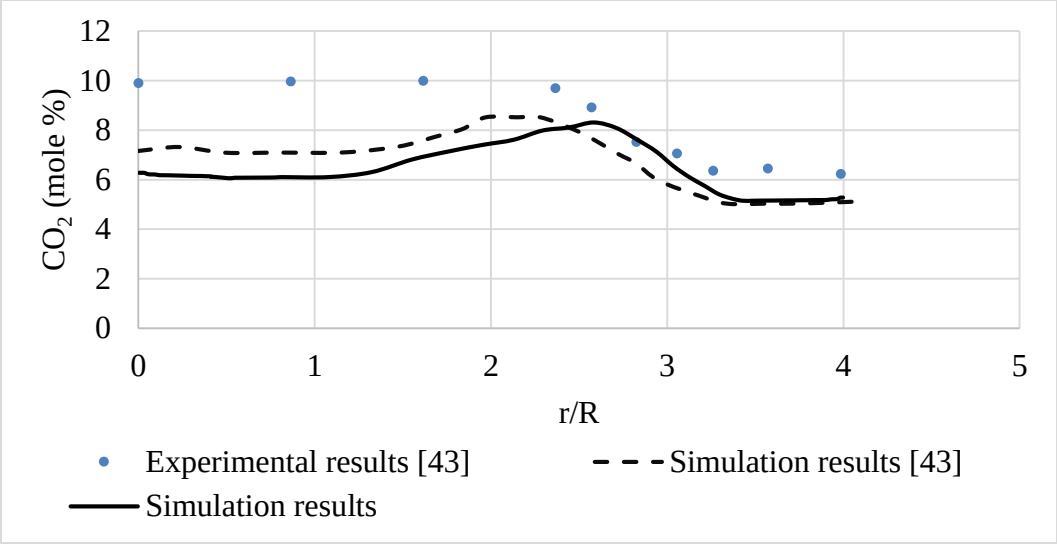

Fig. 40. Comparison of simulation results and experimental data [43] of time-averaged CO_2 concentration at an axial location of $z/R=2.0$

5.2. Swirl-promoted turbulent combustion of emulsified canola oil

In order to study the emission characteristics of emulsified canola oil, understanding the effects of swirl number and equivalence ratio on the profile of turbulent vortices and temperature, is necessary establish relationships between operating parameters and emission generation. In this section, simulated swirl-promoted turbulent flow during the combustion is discussed and analyzed in terms of the frequency spectrum of pressure oscillations, turbulent kinetic energy, and the shape of recirculation zone. The temperature profile in the combustion chamber was studied by comparing it with the distribution of vortices with high intensity. The profiles of emissions for *CO* and thermal NO_x were analyzed by comparing their concentration to corresponding temperature profiles. The simulated overall concentrations of *CO* and NO_x were compared with Bhimani's [4] experimental data as well.

The time interval for the simulation was set at 1×10^{-6} s (1 μs). Simulation data were collected for about *3* flow-through times (60×10^{-3} s or 60 ms) to obtain statistically meaningful turbulent properties. The numerical models used for combustion simulation are shown in Table 5 in Chapter 3, and have been validated as explain above.

5.2.1. Swirl-promoted turbulent flow during combustion

Due to the chemical reaction between air and emulsified canola oil, a high temperature zone is produced by the flame, which leads to intensified turbulent flow field within the combustion chamber. Therefore, it is important to understand the effects of swirl number and equivalent ratio on the turbulent flow field during the combustion process. In this section, the effects of swirl number and equivalent ratio on the turbulent flow field with combustion are discussed in terms of frequency spectrum of pressure oscillations, the profile of turbulent kinetic energy, and the shape of recirculation zone in the combustion chamber.

According to the statistical approach used to describe turbulence, the frequency spectrum of pressure oscillation can be used to estimate the size of vortices in the flow field. The high value of frequency indicates small size of vortex, and vice versa [25]. In order to obtain the distribution of turbulent eddies during the combustion process, four simulation probes were used to register pressure oscillation within the simulated combustion chamber. In the discussion of cold flow, a corner recirculation flow was observed, hence the simulation probe, *P1* at the axial location (z/H) of *0.01* was selected in the corner of the combustion chamber. Furthermore, the most intense turbulent flow is

produced near the outlet region of swiler. Therefore, two simulation probes, namely *P2* and *P3* were selected within this region at axial locations (z/H) of *0.38* and *1*. In order to understand the effects of chemical reaction on pressure oscillation, *P4* near the center line of the combustion chamber was also selected at an axial location (z/H) of *4*. The locations of four probes are shown in Fig. 41.

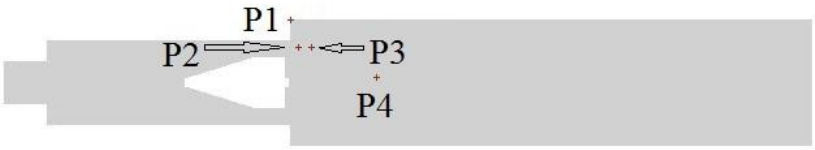

Fig. 41. Simulation pressure probes within the simulation domain

The collected data in time domain form has been converted to the frequency domain using by Fast Fourier Transform (FFT). Fig 42 (a-d) and (e-h) show the frequency spectrum for ϕ of *0.81* and *0.97* at a *SN* of *1.0*, respectively. Fig 42(a-d) and (e-h) show the frequency spectrum for *SN* values of *1.0* and *1.4* at ϕ of *0.81*, respectively. As shown in Fig. 42 and 43, the locations of peak values (i.e. frequencies) for all the four probe points are the same, however, the peak values (i.e. amplitudes) are different. It can be concluded that the turbulent structure or turbulent mode is dominated by the specific conditions given by swirl number and equivalence ratio. The imposed conditions affect the turbulent structure significantly, especially when considering different swirl number.

Fig. 42(a-d) and (e-h) show the effect of equivalence ratio on the size distribution of vortices. In Fig. 43(a-d), the highest peak or amplitude can be observed when the frequency is very small. This peak represents the helical vortex generated by swirler, which indicates that the swirl-promoted flow is prevalent in the flow structure within an axial distance (*z/H*) range from 0 to 4.0. When the frequency is between *0* and 4×10^4 Hz, several peaks can be found, and there is no peak when the frequency is larger than 4×10^4 Hz. This means that the flow for *SN* of *1.0* and ϕ of *0.81* is dominated by large size vortices. In Fig. 42(e-h), the low-frequency peak can be observed as well, but the value of peak is lower than the value seen in Fig. 42(a-d), which indicates that the magnitude of helical vortex generated by the flow for ϕ of *0.97* is smaller than the flow for ϕ of *0.81*. Moreover, two peaks can be found when the frequency is larger than 4×10^4 Hz, and the value of those peaks are much larger than the peaks between *0* and 4×10^4 Hz. This indicates that the flow for *SN* of *1.0* and ϕ of *0.97* is able to produce more small size vortices in the combustion chamber.

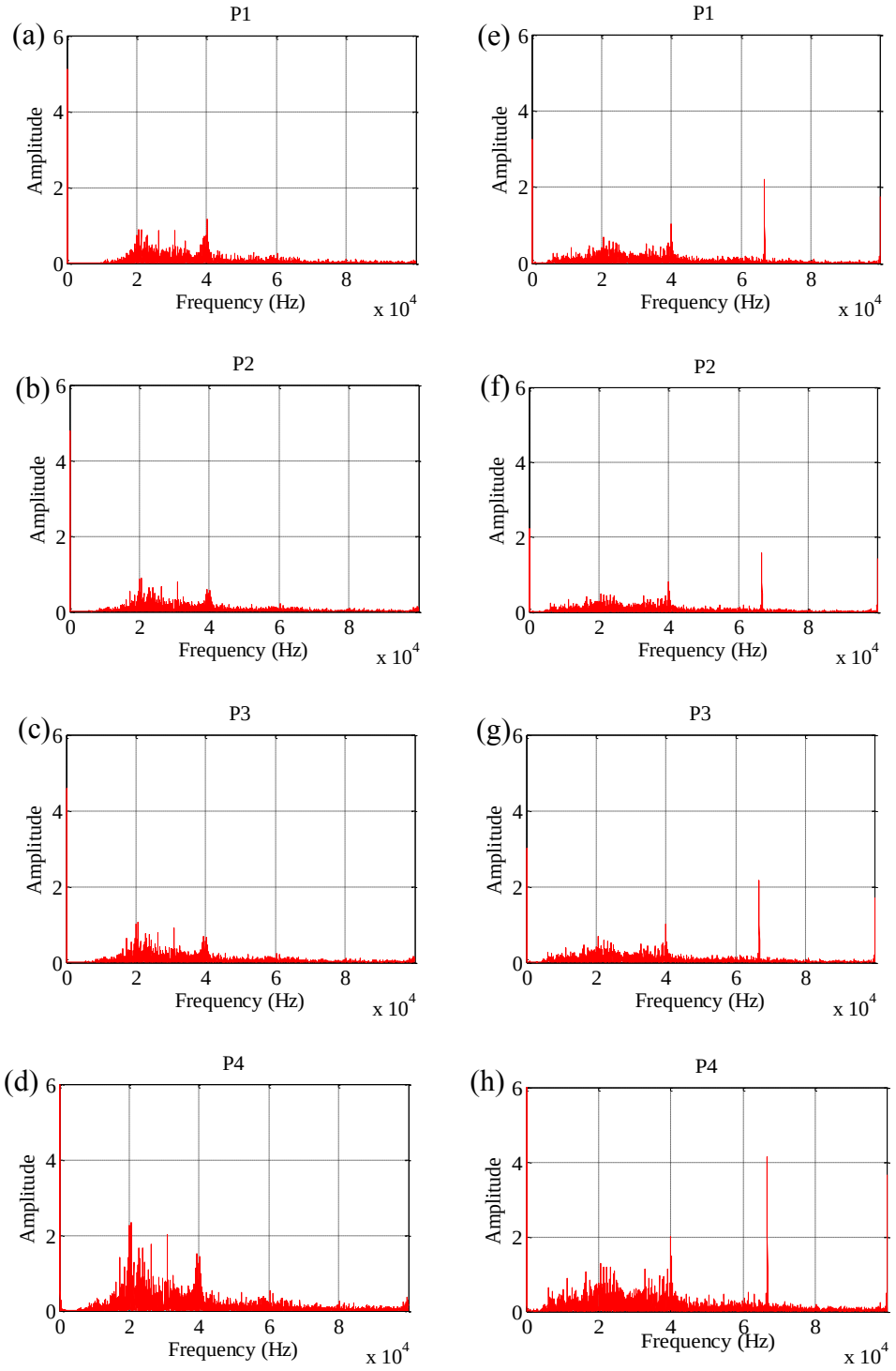

Fig. 42. Frequency spectrum of pressure oscillation at locations of *P1*, *P2*, *P3*, and *P4* for *SN* of *1.0* at (a)–(d) ϕ of *0.81*, (e)-(h) ϕ of *0.97*

Fig. 43(a-d) and (e-h) shows the effect of swirl number on the size distribution of vortices. By comparing the value of the low-frequency peak in Fig. 43(a-d) and (e-h), the peak value for *SN* of *1.4* in Fig. 43(e-h) is much greater than the value for *SN* of *1.0* in Fig. 43(a-d), which means that the intensity of helical flow at high swirl number is much greater. In Fig. 43(e-h), two peaks can be observed clearly, including the low-frequency peak and the peak near the 4×10^4 Hz. However, it is hard to identify another dominant peaks in Fig. 43(a-d) except the low-frequency peak. As discussed in Chapter 4, there are two types of vortex flow in the combustion chamber, including the helical flow and the wake flow, which is generated by the swirler and vane, respectively. Therefore, it can be concluded that the low-frequency peak is induced by the helical flow as generated by swirler, and peak near the 4×10^4 Hz is induced by wake flow caused by the vanes. When the *SN* is *1.4*, the turbulent flow is dominated by these two types of flow, and leads to a strong center of recirculation zone. When *SN* is *1.0*, the two types of vortex flow in the combustion chamber are close to each other as shown in Fig. 21(a), which leads to a strong interaction between the helical and wake flows. This process is able to generate different sizes of vortices and reduces the size and intensity of the center of the recirculation zone.

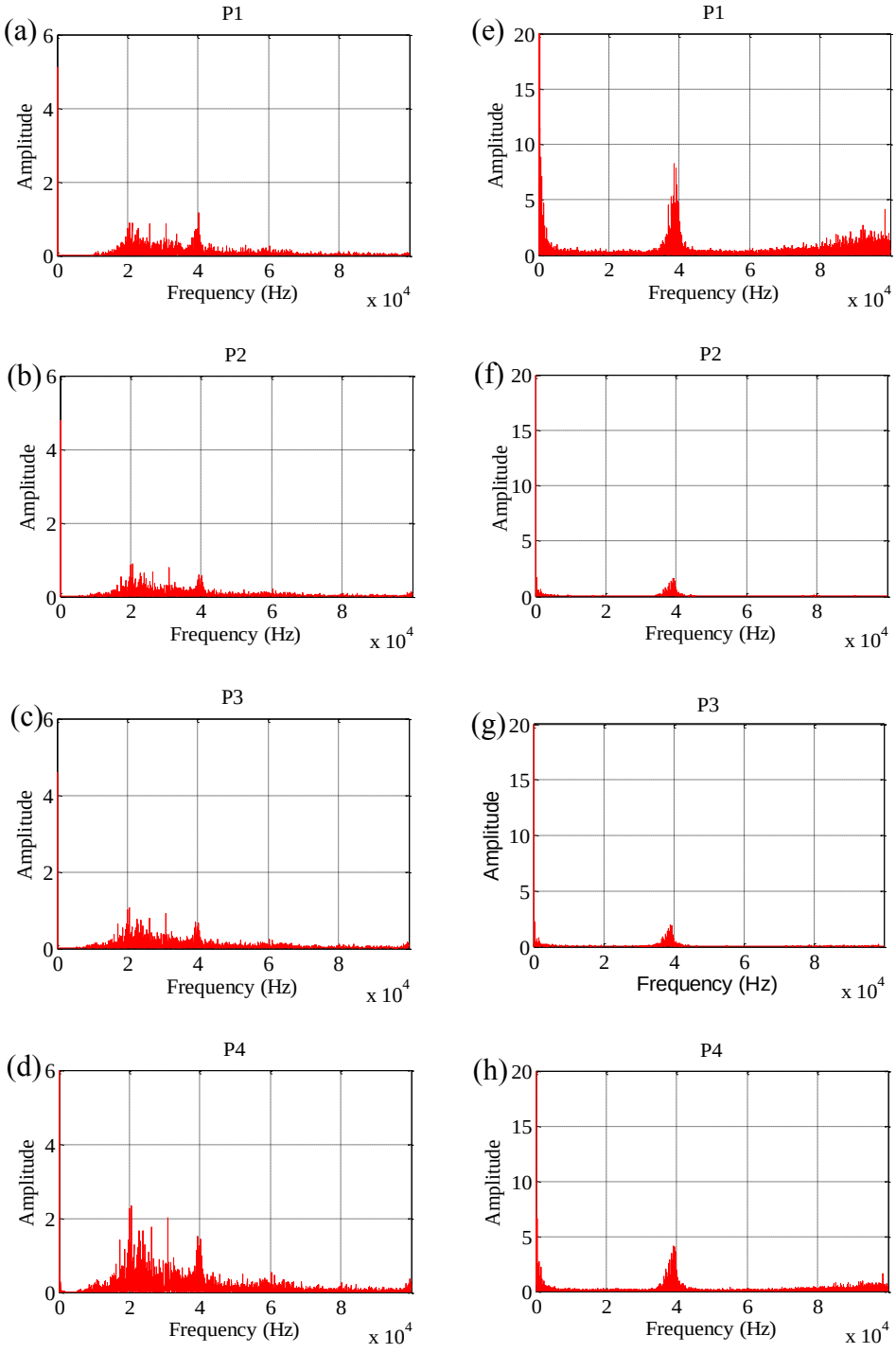

Fig. 43. Frequency spectrum of pressure oscillation at locations of *P1*, *P2*, *P3*, and *P4* for ϕ of *0.81* at (a)-(d) *SN* of *1.0*, (e)-(h) *SN* of *1.4*

Fig. 44 shows the axial locations of three crossing plane, including *z/H=0.38*, *z/H=1*, and *z/H=4*, respectively. The three locations are important in the analysis of combustion and turbulent flow. Fig. 45(a) and (b) shows the mean temperature profile when the mean temperature is set at *2000* K for *SN* of *1.0* and *1.4*, respectively, which represents the location of the flame within the combustion chamber. As Fig 45 shows, swirl number has a direct effect on the extent of the flame within the combustion chamber. For *SN* of *1.0*, the flame can extend to a *z/H* of *6*, while for *SN* of *1.4*, it only extends to *z/H* of *3.25*.

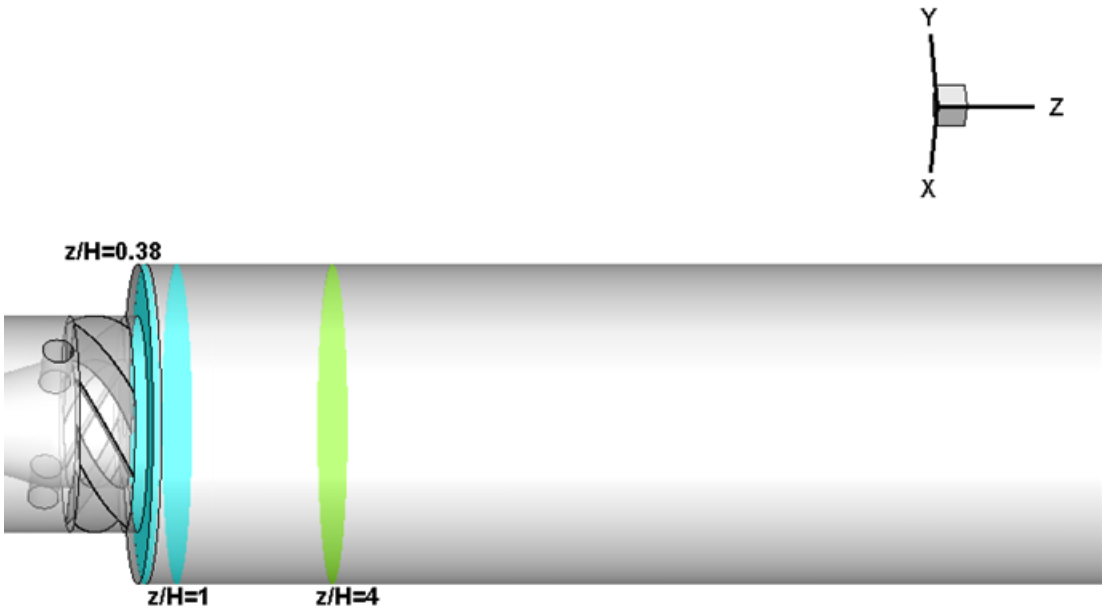

Fig. 44. Schematic diagram of three axial locations within the combustion chamber

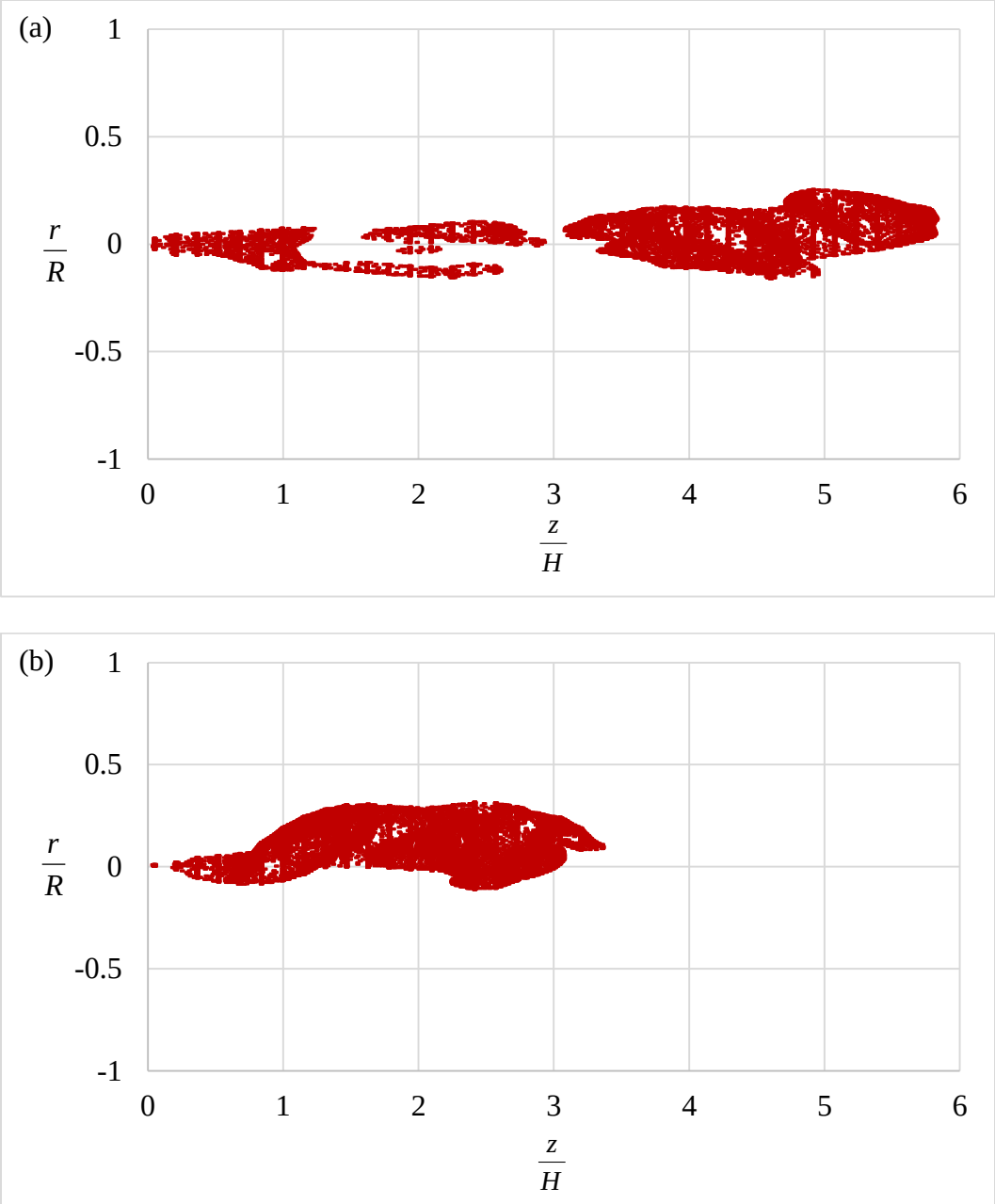

Fig. 45. The mean temperature profile at *2000* K for (a) *SN* of *1.0*, (b) *SN* of *1.4*

When the fuel droplets are injected into the combustion chamber, the fuel droplets respond to the imposed high temperature of the combustion chamber by

absorbing energy, which leads to partial to full evaporation of the droplets. As a result, a rich fuel/air mixture is produced in the vicinity of the nozzle [47]. This process leads to combustion, where a flame is generated within the center of chamber. Fig. 46 shows the mean temperature profile for *SN* of *1.0* and ϕ of *0.81* at the crossing plane (z/H) of *4*. In Fig. 46, the highest temperature is in the center of chamber. According to the study by Menon and Sankaran [73], the turbulence fluctuation peak is also near the center line of the combustion chamber, where heat is released due to combustion reactions taking place. Hence, it significantly contributes to the generation of turbulent kinetic energy at the center of the chamber.

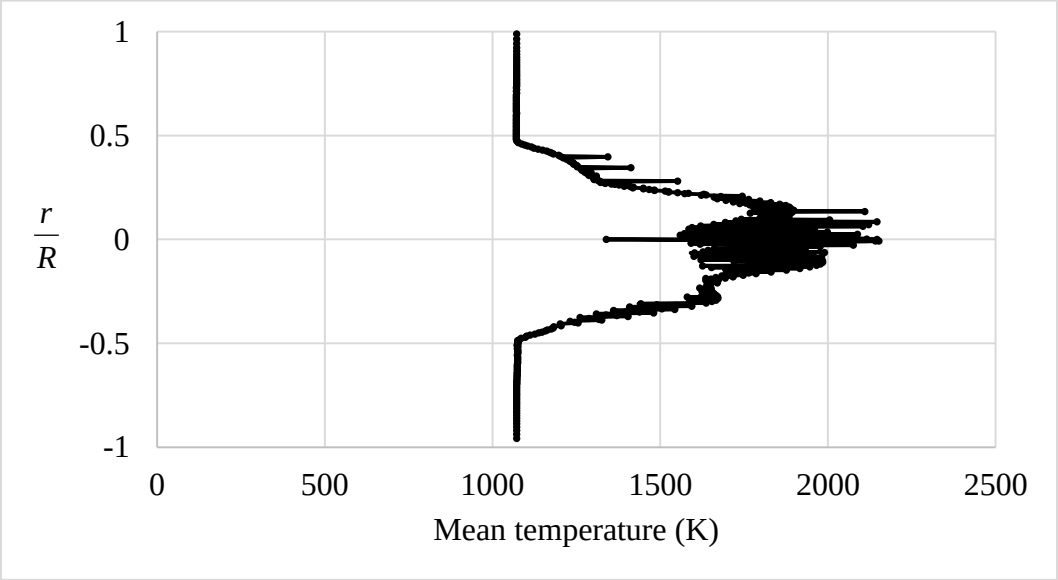

Fig. 46. Mean temperature profile for *SN* of *1.0* and ϕ of *0.81* at the crossing plane of *z/H=4*

Fig. 47(a) and (b) show the time-averaged normalized turbulent kinetic energy (TKE) for ϕ of *0.81* and *0.97* for *SN* of *1.0* at three axial locations, respectively. As explained above, the peak value of TKE can be observed in the center line of the combustion chamber. Due to the great concentration of fuel droplets and the reaction between air and the fuel, the time-averaged normalized TKE increases in the region of the nozzle outlet, which leads to a maximum value at a *z/H* of *1*. When the combustion spreads downstream of the chamber, the fuel droplets and reaction products lose their initial mass and momentum. Therefore, the time-averaged normalized TKE decreases at a location of *z/H* of *4*.

By comparing the Fig. 18 and Fig.47 (a), it is obvious that the combustion of the fuel leads to much greater total kinetic energy under the same flow conditions (i.e. flowrate). Fig. 47(a) and (b) shows that the intensity of turbulence for ϕ of *0.97* is greater than that for ϕ of *0.81* in the vicinity of nozzle outlet ($0< z/H < 1.0$); however, the turbulent intensity for ϕ of *0.97* reduces rapidly in the downstream direction. It should be kept in mind that the flowrate of air associated with ϕ of *0.81* is 18% greater than when ϕ is *0.97,* so a decay in the turbulence intensity at lower air flowrate is expected. Nevertheless, the adiabatic flame temperature within the nozzle outlet region ($0< z/H < 1.0$) is greater for ϕ of *0.97* than for ϕ of *0.87.* This is consistent with previous findings that show that the adiabatic flame temperature reaches its greatest value near stoichiometric conditions, which leads to higher turbulent intensity [74]. As discussed in Chapter 4, the angular momentum is able to make turbulent flow stronger and wider.

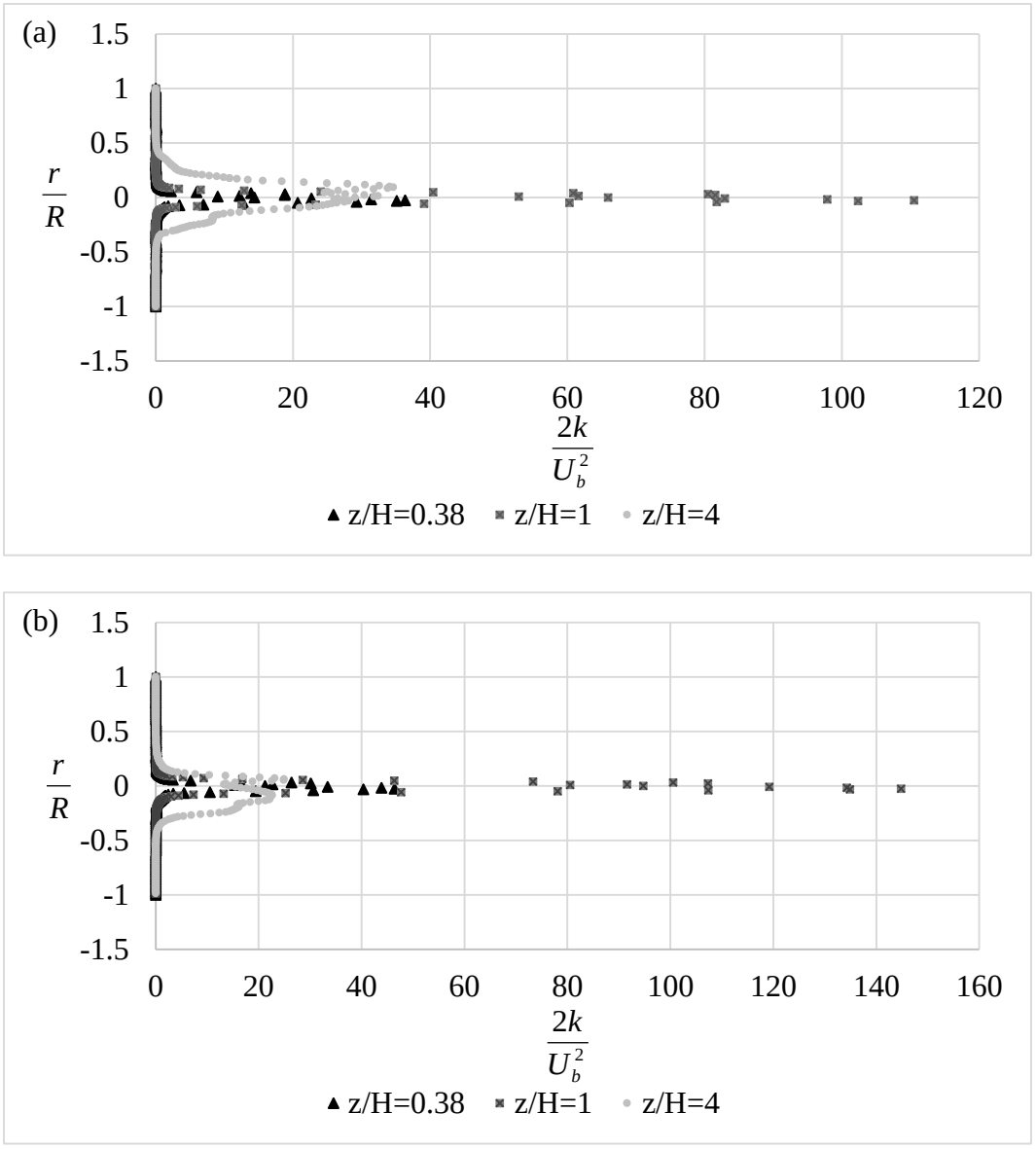

Fig. 47. Time-averaged normalized turbulent kinetic energy (TKE) for *SN* of *1*.0 at three axial locations at (a) ϕ of *0.81*, (b) ϕ of *0.97*

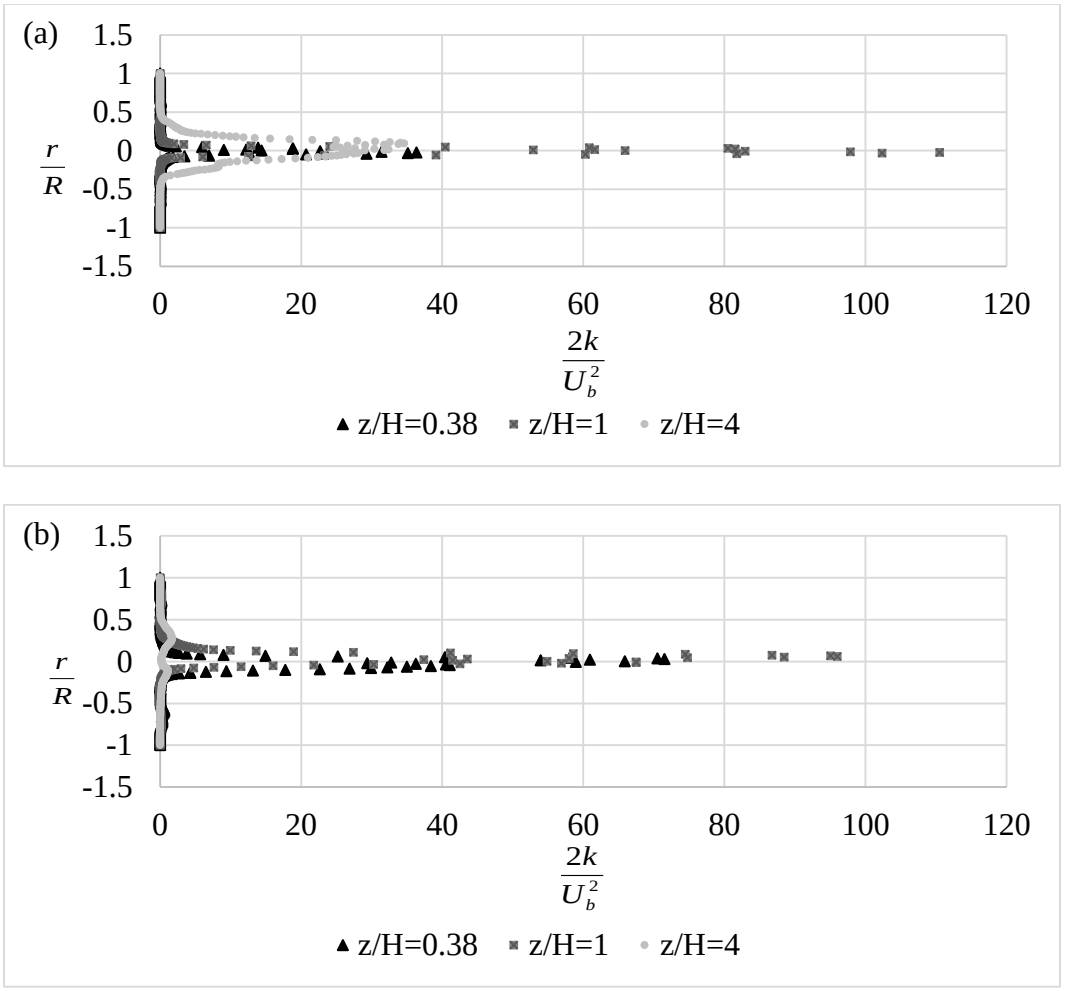

Fig. 48. Time-averaged normalized turbulent kinetic energy (TKE) for ϕ of *0.81* at three axial locations when (a) *SN* is *1.0*, (b) *SN* is *1.4*

Fig. 48(a) and (b) show the time-averaged normalized turbulent kinetic energy (TKE) for *SN* of *1.0* and *1.4* when ϕ is *0.81* at three axial locations, respectively. In the flame region (between *z/H=0.38* and *z/H=1*), the TKE values for *SN* of *1.4* are generally higher than those at *SN* of *1.0*. At a location of *z/H=0.38*, it is evident that TKE is considerably greater at SN = 1.4. On the other hand, the difference between TKE values at *z/H=0.38* and *z/H=1.0* for *SN* of 1.4 is much smaller than that for *SN* of *1.0*. This

implies that the turbulence flow field is relatively stable within a certain axial distance on the upstream side when the *SN* is set at *1.4*, which in turn is able to enhance the stability of flame. At the location of *z/H=4*, TKE for *SN* of *1.4* is very small, which is consistent with Fig. 45, since it is outside of the region of the flame.

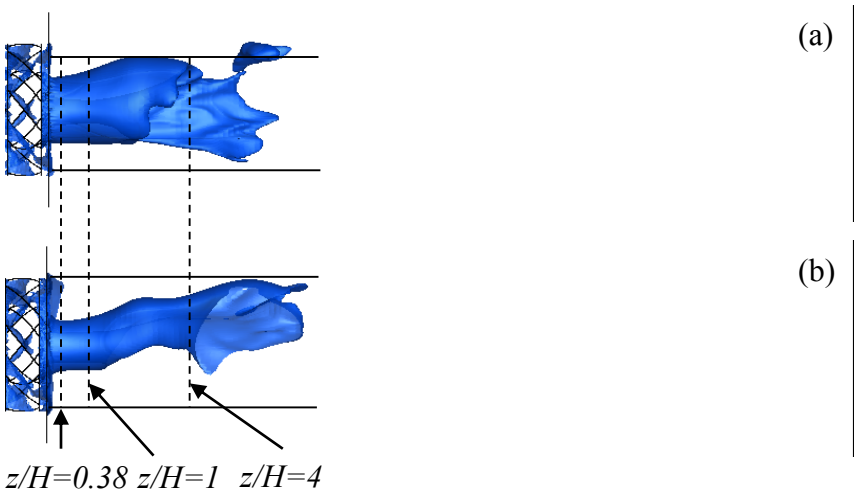

Fig. 49. Center recirculation zones for *SN* of *1.0* (a) when ϕ is *0.81*, (b) when ϕ is *0.97*

Fig. 49(a) and (b) show the shape of center of the recirculation zones using iso-surface of time-averaged axial velocity ($<u_z> = 0$) for ϕ of *0.81* and *0.97* at *SN* of *1.0*, respectively. By comparing Fig. 49 with Fig. 19, it is evident that the center recirculation zones (CRZ) with combustion are not completely enclosed by the iso-surfaces seen in Fig. 19. The shape of the recirculation zones on the upstream side is similar to the shape in the cold flow case. However, the recirculation zone on the downstream side is not enclosed, since the shape of the zone is affected by the interaction between the swirl-

promoted air flow and the flame itself. This can explain the shift of the distribution of *CRZ* in the spanwise direction, as seen in Fig. 49. However, when the swirl number is kept the same, the effect of equivalence ratio on the shape of the recirculation zone is not significant.

Fig. 50 (a) and (b) illustrate the shape of the center recirculation zones using iso-surface of time-averaged axial velocity ($<u_z> = 0$) for *SN* of *1.0* and *1.4*, when ϕ is *0.81*, respectively. It shows that the center recirculation zone at *SN* of *1.4* is wider and longer than that at *SN* of *1.0*. It implies that the fluid flow at *SN* of *1.4* has a stronger recirculation zone when combustion takes place.

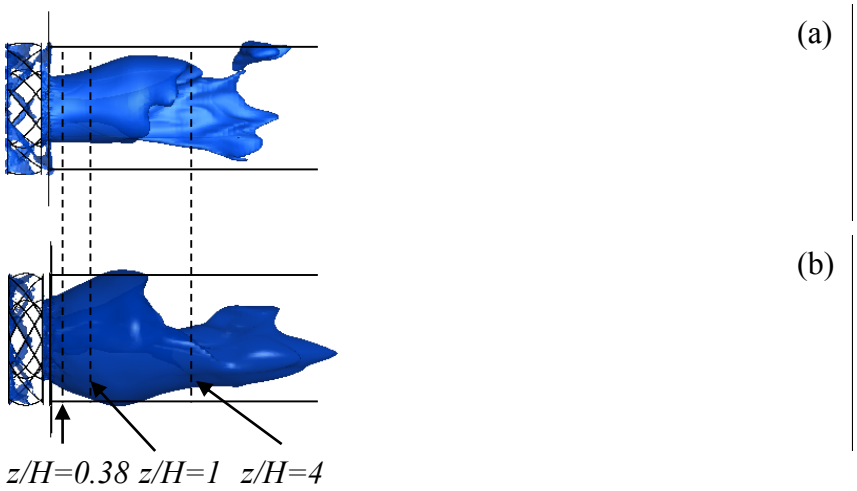

Fig. 50. Center recirculation zones for ϕ of *0.81* (a) when *SN* is *1.0*, (b) when *SN* is *1.4*

5.2.2. Effects of swirl number and equivalence ratio on combustion characteristics

In this section, the effects of swirl number and equivalence ratio on the profiles of temperature, *CO*, and NO_x emissions in the combustion chamber are discussed. The relationship between the turbulent flow and the combustion characteristics are discussed and analyzed.

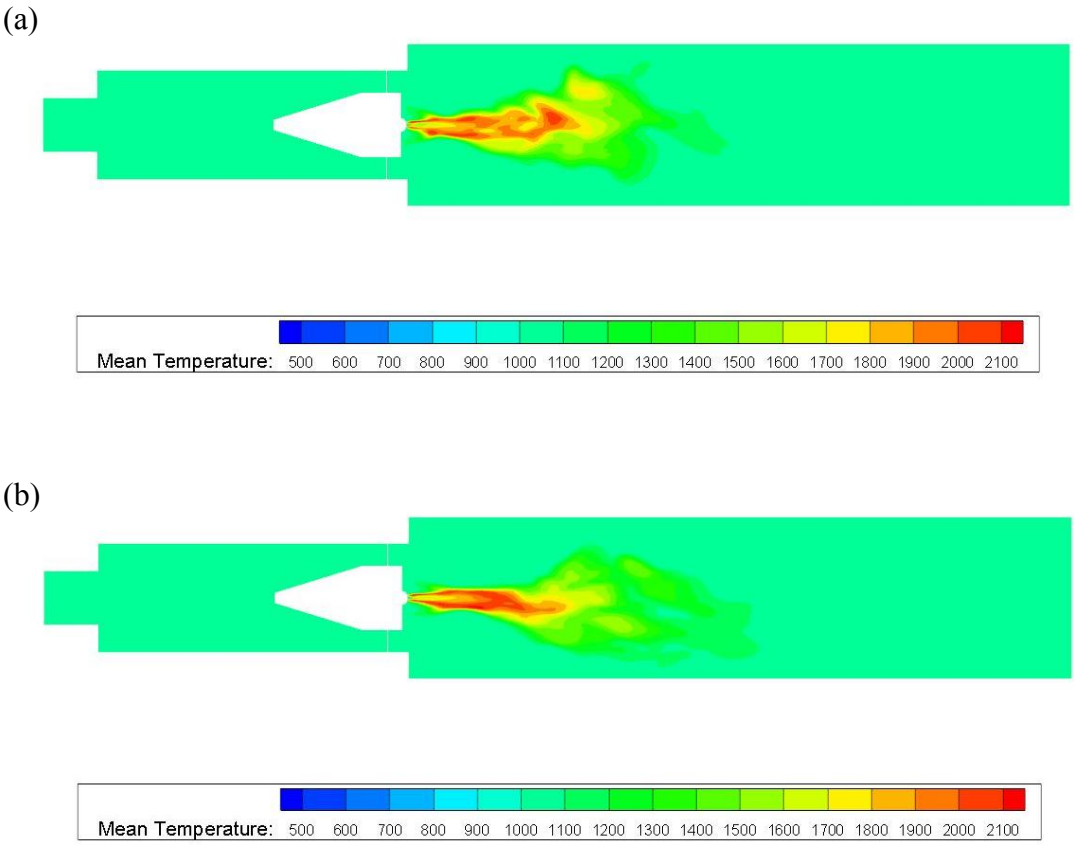

Fig. 51. Mean temperature profile for *SN* of *1.0* when (a) ϕ is *0.81*, (b) ϕ is *0.97*

Fig. 51(a) and (b) show the mean temperature profile for *SN* of *1.0* when ϕ is *0.81* and *0.97*, respectively. When the liquid fuel droplets are injected into the combustion chamber at a temperature of *1000* K, the droplets start to evaporate and a fuel vapor is created. The air surrounds the droplets spray, and mix with the fuel vapor which is at the front of the spray. When air-to-fuel ratio is nearly the stoichiometric ratio at the chamber temperature of *1000* K, the flame is generated. In Fig. 51, the temperature profile for ϕ of *0.97* shows to be a more concentrated distribution when compared with the temperature profile for ϕ of *0.81*. As explained above, the swirler is able to create a center recirculation zone. The reverse flow present in the *CRZ* helps to deliver oxygen to the flame, which enhances the combustion inside the fuel spray. This leads to the dispersion of the temperature profile at ϕ of *0.81*. However, the effect of equivalence ratio on flame length is not significant when the swirl number is the same.

Fig. 52(a) and (b) illustrates the mean temperature profiles for ϕ of *0.81* when *SN* is *1.0* and *1.4*, respectively. It can be observed that the length of the flame for *SN* of *1.4* is much shorter than that for *SN* of *1.0*. In Fig. 50, a wider and longer recirculation zone is generated by the flow when *SN* is *1.4* when compared with the flow at a *SN* of *1.0*. As the figure shows, higher swirl number leads to greater confinement of the flame region caused by the recirculation zone. It is well know that the recirculation zone constitutes a well-mixed region, where vigorous heat and mass transfers take place. Furthermore, it helps to recirculate fresh combustible mixture of air and fuel [75] from the downstream region. Therefore, the combustion at *SN* of *1.4* is more intense, which leads to the formation of a concentrated high temperature region as shown in Fig. 52(b).

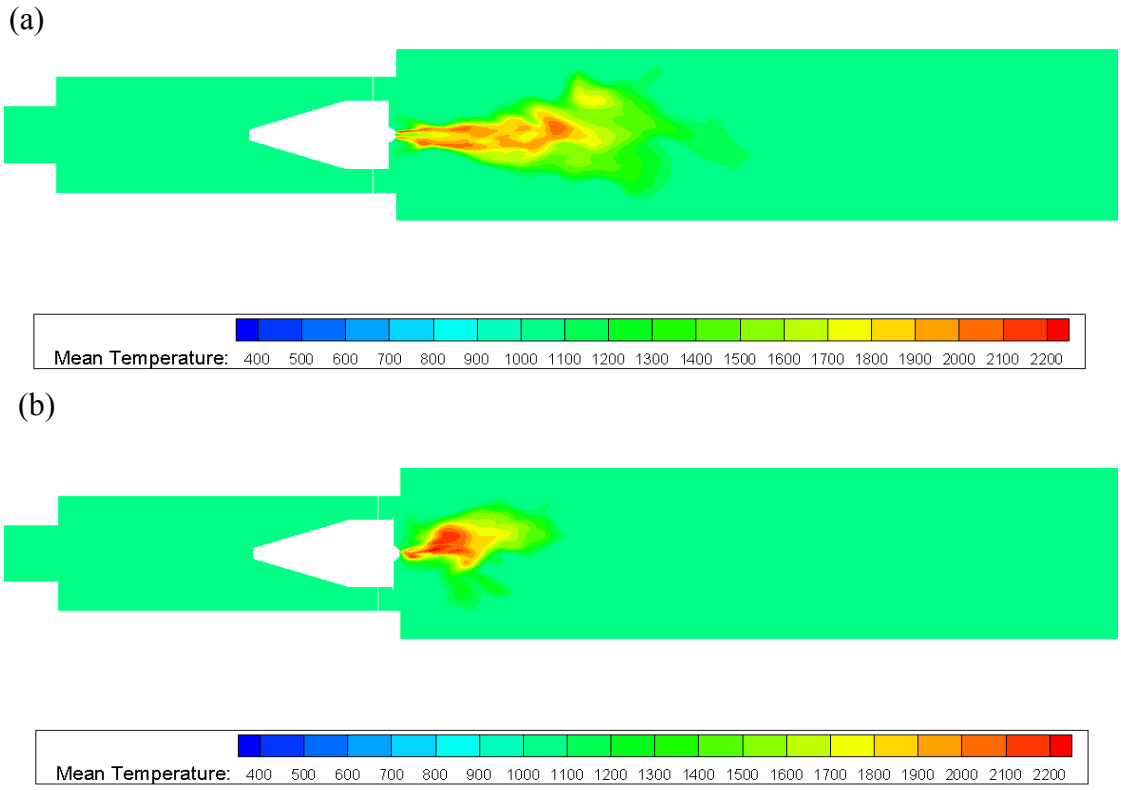

Fig. 52. Mean temperature profile for ϕ of *0.81* when (a) *SN* is *1.0*, (b) *SN* is *1.4*

Fig. 53(a) and (b) show the iso-surface of mean temperature of *2000* K after *60* ms for *SN* of *1.0* and *1.4* when ϕ is *0.81*, respectively. It illustrates the shape of flame in the combustion chamber. As shown in Fig. 53, the flame when *SN* is *1.4* concentrates in the upstream region of the combustion chamber. Moreover, a significant amount of reverse flow at *SN* of *1.4* leads to a backward motion of the flame in the vicinity of nozzle ($0 < z/H < 1.0$), which is characterized by a wider flame around the nozzle. When *SN* is *1.0*, the flame region increases gradually along the downstream direction as shown in Fig. 53(a). However, this process cannot be observed in Fig. 53(b). This implies that the

distribution of fuel vapor on the upstream side (*1.0* < *z/H* < *4.0*) is much wider in the spanwise direction and more concentrated in the streamwise direction when *SN* is *1.4*.

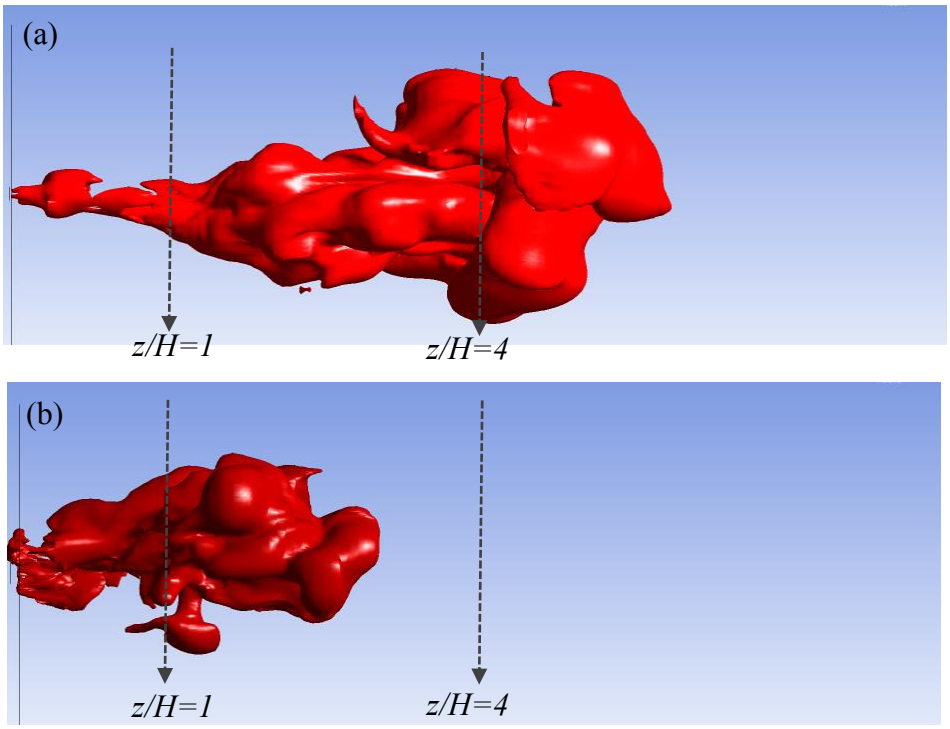

Fig. 53. Iso-surface of mean temperature of *2000* K at *60* ms for ϕ of *0.81* when (a) *SN* is *1.0*, (b) *SN* is *1.4*

Fig. 54(a) and (b) show the iso-surface of mean temperature of *2000* K combined with the surface representing a Q-criterion value of *40000* s^{-2} after *60* ms at ϕ of *0.81* when *SN* is *1.0* and *1.4*, respectively.

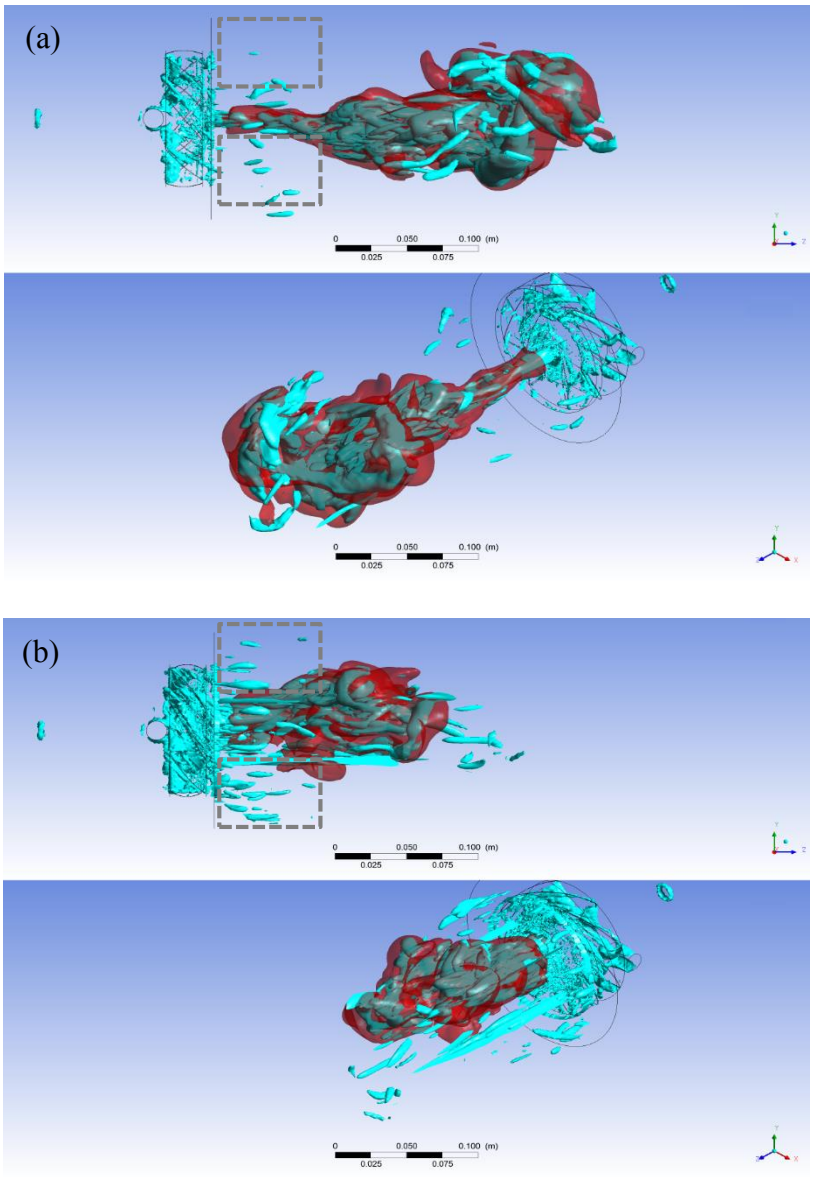

Fig. 54. Snapshot of iso-surface of mean temperature of *2000* K with Q-criteria value of *40000* s^{-2} at *60* ms for ϕ of *0.81* when (a) *SN* is *1.0*, (b) *SN* is *1.4*

It can be observed that the vortices profiles correspond to the shape of flame somewhat, and high intensity of vortices are generated at the front of flame for both swirl numbers. However, more vortices with high intensity are produced near the outlet

region of swirler when *SN* is *1.4* as shown in the black boxes of Fig. 54(a) and (b), and these vortices are outside of the high temperature region as illustrated by the red surface. In Fig. 39, the greatest amplitude of helical flow, wake flow, and corner recirculation flow are observed at the location of P_1 *(z/H=0.01)* for *SN* of *1.4* as shown in Fig. 43(e). This implies that the flow when *SN* is *1.4* induces the greatest level of turbulence, which leads to a great evaporation of fuel droplets in the vicinity of the nozzle. In Fig. 48(b), the TKE for *SN* of *1.4* at the location of *z/H=0.38* is much higher than that for *SN* of 1.0, which reflects the level of intense combustion near the nozzle region.

Fig. 55(a) and (b) show the distribution of emulsified canola oil on a mass fraction basis after *60* ms for ϕ of *0.81* when *SN* is *1.0* and *1.4*, respectively. According to the value of the scale in Fig. 55, the concentration of fuel in the vicinity of nozzle when *SN* is *1.4* is much higher than that when *SN* is *1.0*, which is attributed to high level of turbulent intensity and recirculation zone of *SN* of 1.4 as explained above.

(a)

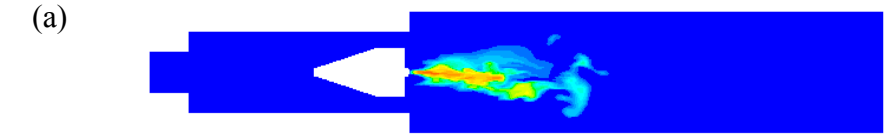

Contours of mass fraction of emulsified canola oil

(b)

Contours of mass fraction of emulsified canola oil

Fig. 55. Distribution of emulsified canola oil on a mass basis after 60 ms for ϕ of 0.81 when (a) SN is 1.0, (b) SN is 1.4

Fig. 56(a) and (b) show the distribution of *CO* after *60* ms for *SN* of *1.0* when ϕ is *0.83* and *1.00*, respectively. Comparing with the contour in Fig. 54(a) and Fig. 56(a), it can be observed that the distribution of *CO* corresponds with the distributions of temperature and vortices. This implies that the generation of *CO* depends on the corresponding temperature and vortices profiles significantly. Due to the small effect of

equivalence ratio on temperature and vortices as discussed above, the distribution of *CO* for both equivalence ratios has a similar range in the streamwise and spanwise directions, as shown in Fig. 56(a) and (b). On the downstream side of the combustion chamber, the temperature profile for ϕ of *0.97* is less dispersed as shown in Fig. 51(b). It implies that less fresh air flows into the flame region, which leads to a richer fuel/air condition when ϕ is *0.97*. Therefore, the combustion at ϕ of *0.97* generates more *CO* in the center of downstream side in the combustion chamber. Furthermore, Fig. 56 shows the overall *CO* emissions in the combustion chamber after 60 ms. As seen in Fig. 56, the combustion at ϕ of *0.97* produces more *CO* than that at ϕ of *0.81* due to the high equivalence ratio (less oxygen) and lower turbulent intensity.

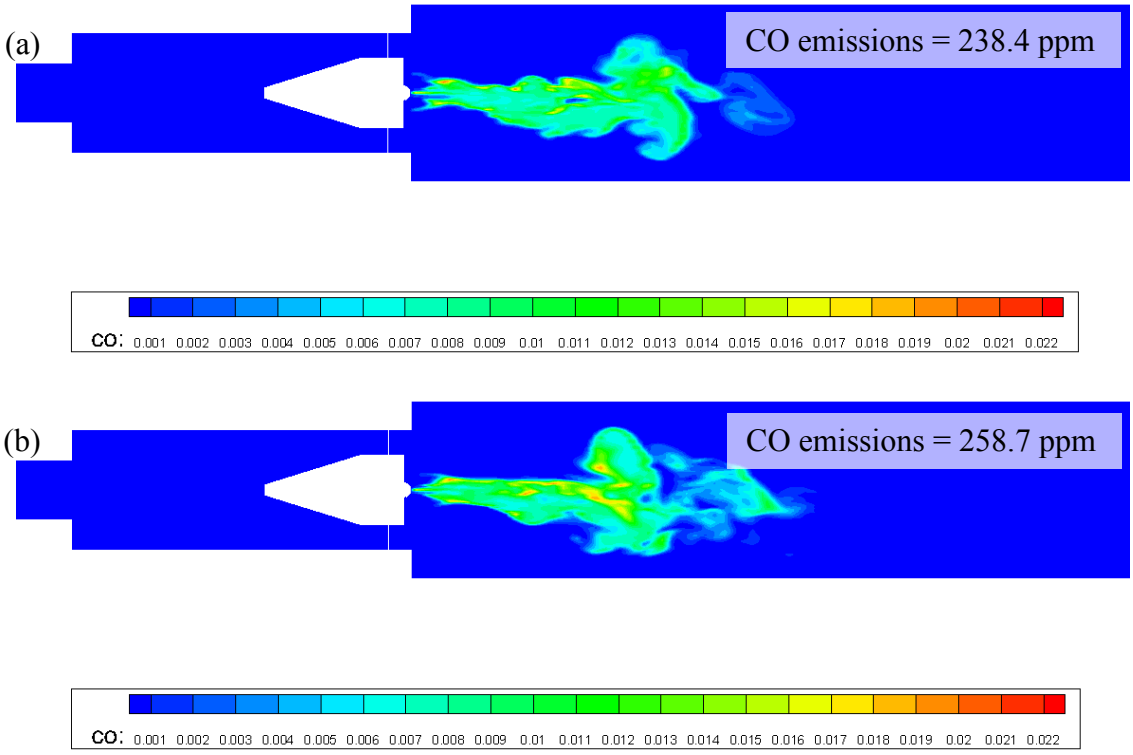

Fig. 56. Distribution of *CO* after *60* ms for *SN* of *1.0* when (a) ϕ is *0.81*, (b) ϕ is *0.97*

Fig. 57(a) and (b) show the distribution of *CO* after *60* ms for ϕ of *0.83* when *SN* is *1.0* and *1.4*, respectively. The effect of the swirl number on the distribution of *CO* in the combustion chamber is significant. As shown in Fig. 57(a) and (b), the distribution of *CO* for *SN* of *1.4* is much concentrated than that for *SN* of *1.0*. Most of *CO* at *SN* of *1.4* is produced on the upstream side of the combustion chamber, and the distribution of *CO* is accumulated in the upper layer of the combustion chamber as shown in Fig. 57(b). Moreover, high concentration of *CO* is generated near the center of the combustion chamber when *SN* is *1.4*. As shown in Fig. 58, a large area of *CRZ* is observed on the bottom side of the combustion chamber when *SN* is *1.4* as illustrated by the green

surface. The *CRZ* induces the backward motion of the air/fuel mixture and reaction products, which leads to a lower concentration of oxygen in this region as shown by contour in Fig. 58. Therefore, high concentration of *CO* is observed near the center of the combustion chamber. Furthermore, Fig. 57 shows the overall *CO* emissions in the combustion chamber after *60* ms. As seen in Fig. 57, the combustion process for *SN* of *1.0* produces more *CO* than that at *SN* of *1.4*. Although there are some relatively high concentration areas of CO that can be found in the combustion chamber when *SN* is *1.4*, the strong *CRZ* confines the combustion to a small region. This in part leads to small *CO* emissions in the combustion chamber when *SN* is *1.4*.

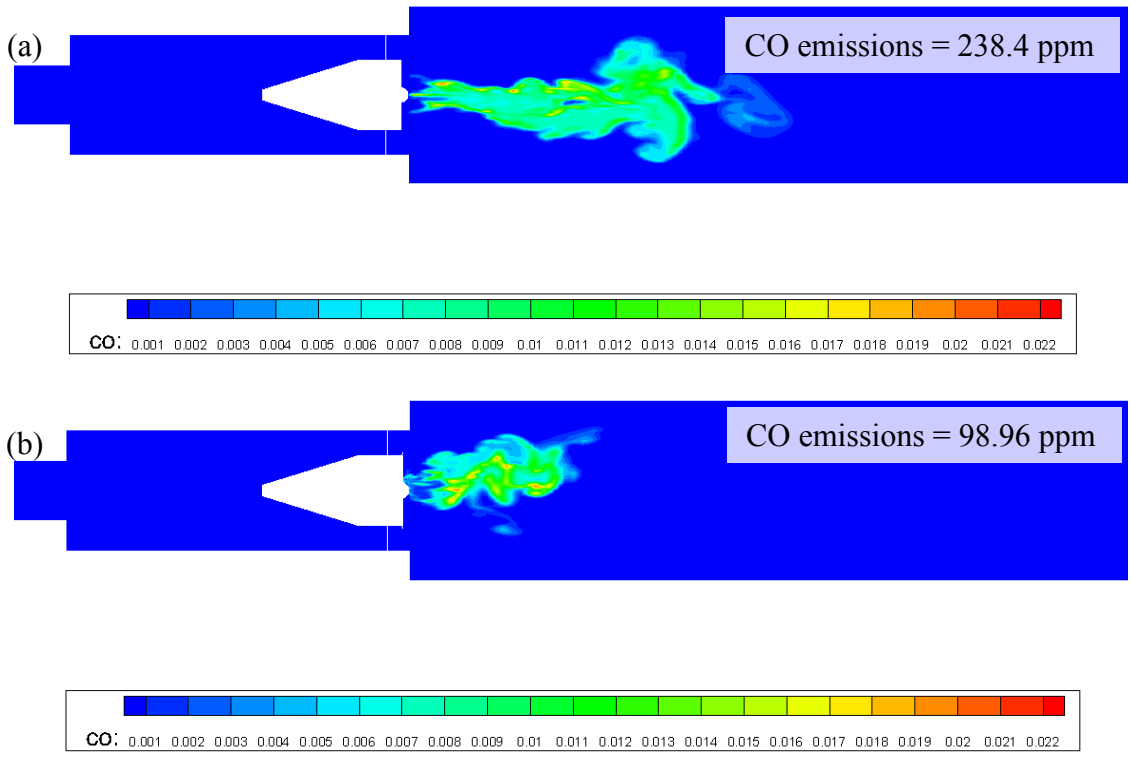

Fig. 57. Distribution of *CO* after *60* ms for ϕ of *0.81* when (a) *SN* is *1.0,* (b) *SN* is *1.4*

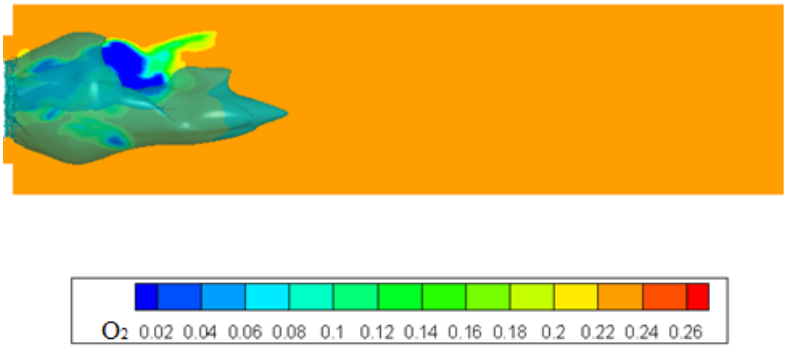

Fig. 58. Distribution of O_2 and center recirculation zone after *60* ms for ϕ of *0.81* and *SN* of *1.4*

Fig. 59(a) and (b) show the distribution of NO_x after *60* ms for *SN* of *1.0* when ϕ is *0.81* and *0.97*, respectively. It can be observed that most of the NO_x emissions are produced on the downstream side of the combustion chamber for both equivalence ratios at *SN* of *1.0*. Due to the high level of turbulent intensity when ϕ is *0.81*, the value and region of the temperature profile in the combustion chamber for ϕ of *0.81* is larger than that when ϕ is *0.97*, as seen in Fig. 51. Therefore, overall NO_x emissions at ϕ of *0.81* are higher, as expected.

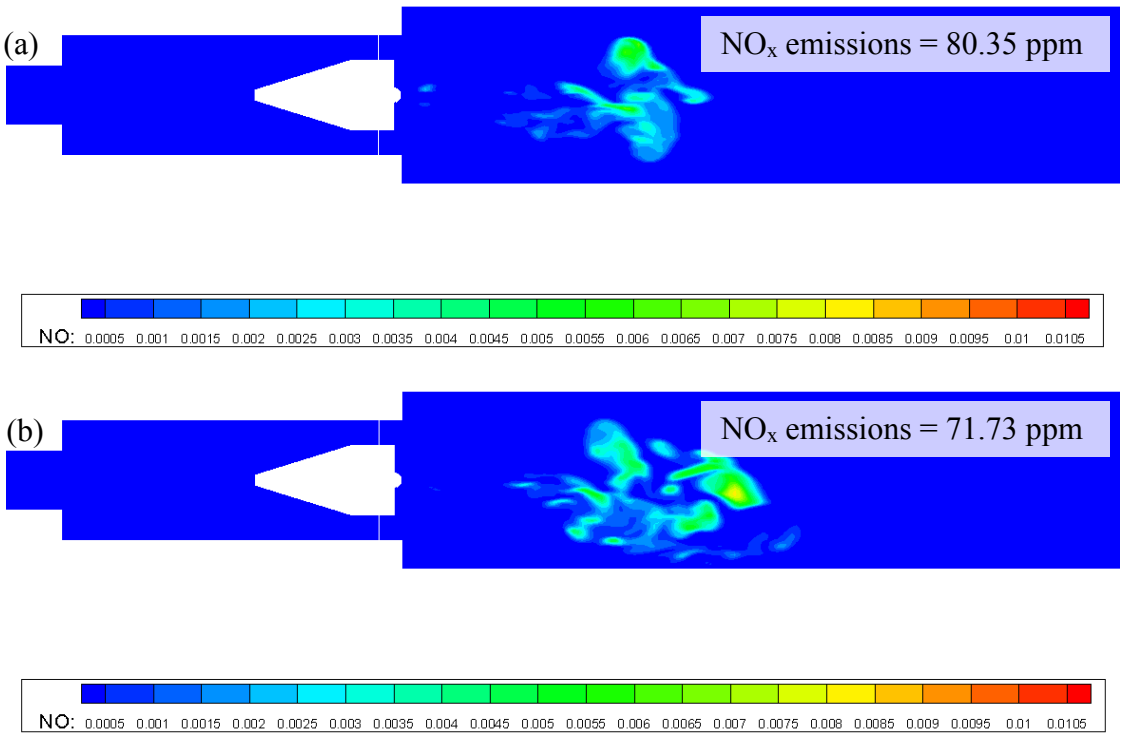

Fig. 59. Distribution of NO_x after *60* ms for *SN* of *1.0* when (a) ϕ is *0.81*, (b) ϕ is *0.97*

Fig. 60(a) and (b) show the distribution of NO_x after *60* ms for ϕ of *0.81* when *SN* is *1.0* and *1.4*, respectively. Due to the strong effect of *CRZ* at *SN* of *1.4*, the distribution of NO_x emissions is located mainly on the upstream side of the combustion chamber. It indicates that the recirculation size volume is directly related to reductions in NO_x levels. On the other hand, the distribution of NO_x at *SN* of *1.0* can be found father downstream into the chamber, as shown in Fig. 60(a). Another key observation in the size of the NO_x distribution region, which is smaller when *SN* of *1.4*.

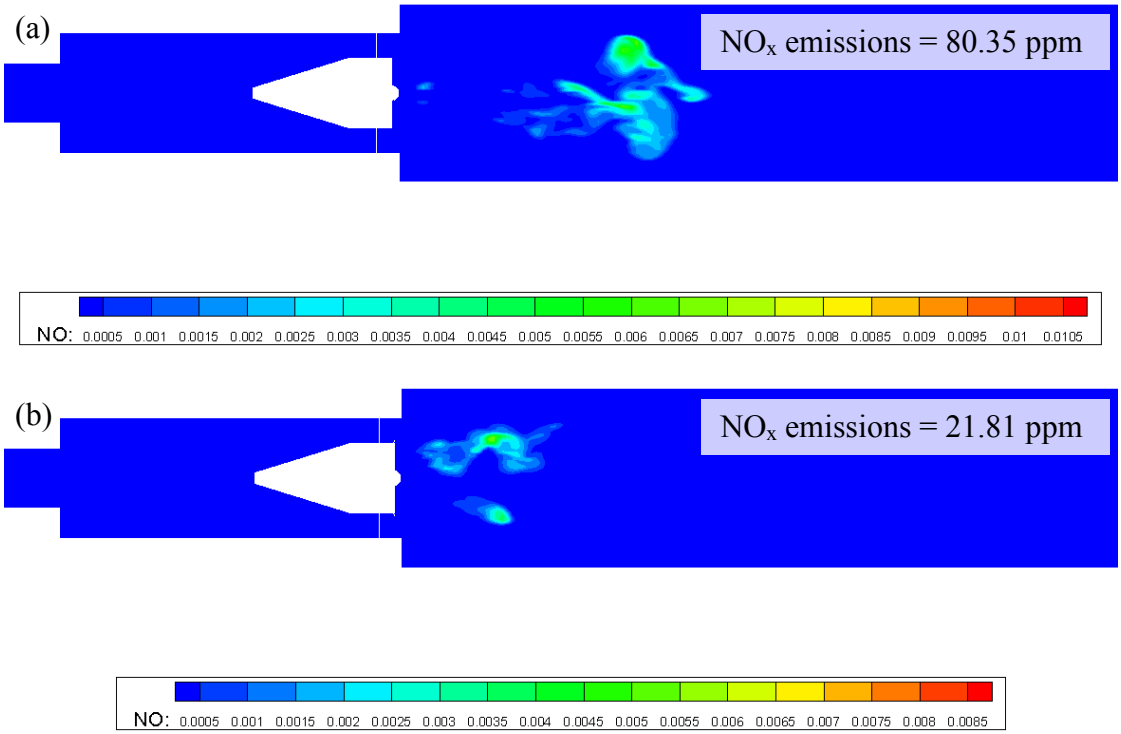

Fig. 60. Distribution of NO_x after *60* ms for ϕ of *0.81* when (a) *SN* is *1.0*, (b) *SN* is *1.4*

To further understand the distribution and levels of NO_x present at different swirl numbers and equivalence ratios, the distributions of NO_x with respect to temperature should be evaluated. Fig. 61(a-d) show the distribution of NO_x after *60* ms for *SN* of *1.0* and *1.4* at ϕ of *0.81* and *0.97*, respectively. Fig. 61(a-d) also show the iso-surface of temperature at *2400* K as depicted by the red surface. It illustrates that the regions of temperature with the highest value can be found on the downstream side of the combustion chamber as well. As explained in Chapter 3, this study considers the thermal NO_x mechanism only. Therefore, the emissions of NO_x are dominated by the size and value of the high temperature region in the combustion chamber, which correspond fairly well with the distribution of NO_x as shown in Fig. 61(a-d).

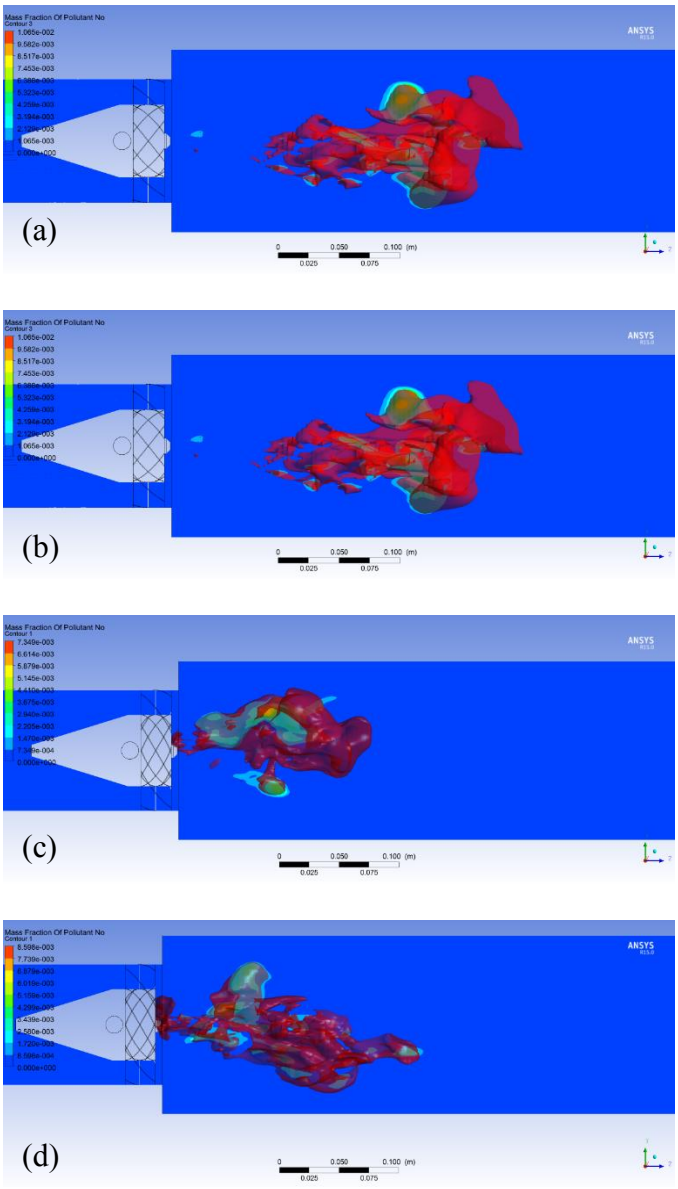

Fig. 61. Distribution of thermal NO_x after *60* ms coupled with iso-surface of temperature at *2400* K for (a) *SN* of *1.0* and ϕ of *0.81*, (b) *SN* of *1.0* and ϕ of *0.97*, (c) *SN* of *1.4* and ϕ of *0.81*, (d) *SN* of *1.4* and ϕ of *0.97*

Looking closer at the relationship between temperature and NO_x emission levels, it can be observed that even though the flame temperature at *SN* of *1.4* is a little higher than that at *SN* of *1.0* as seen in Fig. 52, the flame still is confined in a small region by

CRZ when *SN* is *1.4*. As the results show, NO_x emissions at *SN* of *1.4* are much smaller than that at *SN* of *1.0*, which suggests that flame confinement through a strong *CRZ* can lead to lower NO_x level overall.

Fig. 62 shows the comparison between the simulation work and the experimental work [4] in terms of *CO* emissions based on the same combustion chamber. The solid and dashed lines represent the simulation work and the experimental work of Bhimani et al. [4], respectively. According to the experimental results work, there were no *CO* emissions when the equivalence ratio was equal or smaller than *1.0*. However, the simulations show *CO* emissions for different stoichiometric ratio. The major reason for the difference in the level of CO emissions is due to the location of the exhaust gas analyzer. In the experiments by Bhimani et al. [4], the gas analyzer was connected to the combustion chamber at a sample port located *1.85* m below the nozzle tip, and the temperature in the combustion chamber was higher than *1000* K. These conditions allow *CO* enough time and energy to react with O_2, which could lead to no *CO* emissions flowing into the exhaust gas analyzer. However, the average droplet size considered in the simulation was about 3 times as large as the calculated value reported by Bhimani et al. [4]. The effect of emulsified canola oil droplet size on *CO* level emissions should be investigated in the future.

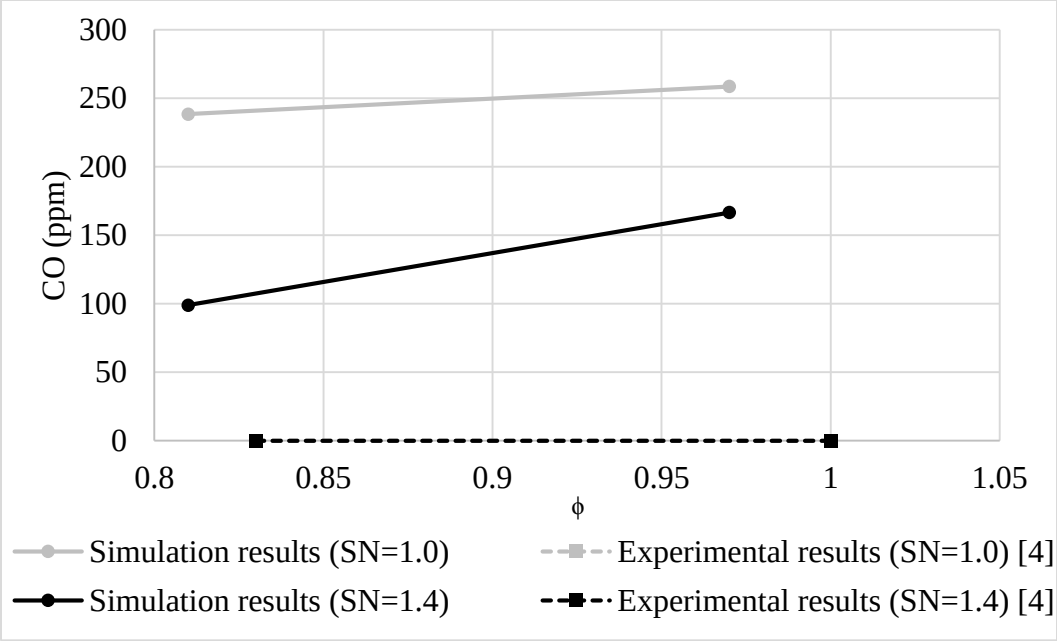

Fig. 62. Comparison between simulation work and experimental work [4] in terms of *CO* emissions

Fig. 63 shows the comparison between the simulation work and experimental work [4] in terms of NO_x emissions based on the same combustion chamber. The solid and dashed lines represent the simulation work and the experimental work of Bhimani et al. [4], respectively. In Fig. 59, the simulation results show the same trends as the experimental work, and the simulation results are close to the experimental results when *SN* is *1.0*. However, the combustion simulations under-estimate the emission levels when compared with the experimental results. This is also discussed in the section of combustion validation in Chapter 5, Section 5.1.

As shown in Fig. 63, due to the lower level of turbulent intensity of *SN* of *1.0*, the combustion process is not as complex as the combustion at *SN* of *1.4*. The numerical

scheme and the simplified reaction mechanisms are able to approach the real combustion behavior. Therefore, the errors of simulations are relatively small, especially in the case of *SN* of *1.0* and ϕ of *0.97*. When *SN* is *1.4*, the greater level of turbulent intensity makes the flow field very complicated, and leads to a complex turbulent combustion process. Moreover, only thermal NO_x was considered in this study. The absence of prompt NO_x in the chemical mechanism may lead to a slightly significant difference from experimental results of NO_x. However, the application of the numerical models and simplified reaction mechanism could lead to a slight difference between the simulated combustion process and the real combustion behavior.

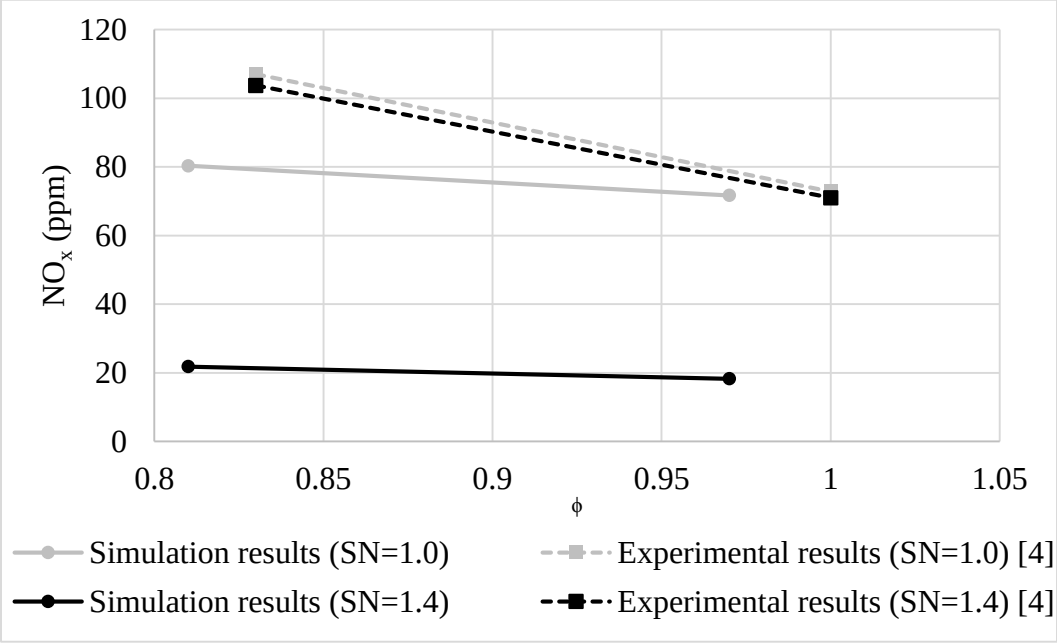

Fig. 63. Comparison between simulation work and experimental work [4] in terms of the concentration of NOx in the combustion chamber

The effects of external boundary conditions should also be considered when comparing the numerical simulations with the experimental results. In the current study, adiabatic conditions were assumed at the wall of the combustion chamber. However, the experiments were conducted in a chamber that experienced heat losses as shown in Table 7. Furthermore, all the measured experimental emission levels were between 800 and 1000 °C [4], which are much lower than the temperatures seen in the combustion simulation. Therefore, the effect of temperature on emission generation should be studied in the detail in the future.

Table 7. Experimental data of Adiabatic Flame and Furnace Temperature [4]

Equivalence Ratio	Adiabatic Flame Temperature (K)	Experimental Furnace Temperature at z/H of 10 for SN of 1.4 (K)	Experimental Furnace Temperature at z/H of 10 for SN of 1.0 (K)
0.83	2166	1218	1208
1.00	2435	1240	1227

In summary, the results shown in the chapter highlight the importance of swirl number on emission levels, which confirm many of the experimental observations done with emulsified canola oil as combustion chamber fuel [4].

6. CONCLUSIONS

The primary objective of this study is to understand the effects of swirl number and equivalence ratio on the turbulent flow field, fuel droplets distribution, temperature profiles and combustion emissions of emulsified canola oil in a *30* kW furnace at CBEL by using a comprehensive numerical approach. To study the combustion phenomena of emulsified canola oil, a proper numerical approach has been chosen and validated. The numerical models including LES, DPM, Stochastics model, TAB, and Eddy-Dissipation model have been used to understand the swirl promoted turbulence flow, the fuel droplets distribution, and combustion. Based on the results of this study, the major conclusions of this research work are presented below.

6.1. Large eddy simulations of swirl-promoted turbulent cold flow in combustion chamber – Conclusions

From the simulation results of swirl-promoted turbulent cold flow, it can be said that,

- The combination between RANS and LES can be used successfully to capture the fluid structure of swirl-promoted turbulence based on validated experimental results
- The swirler is able to generate a center recirculation zone in the combustion chamber.

- The swirl-promoted cold flow at high swirl number produces a greater velocity in axial, radial and tangential direction, and the effect of swirl number diminishes along the axial direction in the combustion chamber.
- The swirl-promoted cold flow at high swirl number produces intense turbulence and a wider and stronger center of recirculation zone in the combustion chamber.
- Two types of processing vortex cores are generated by swirler, including spiral flow and double-helix wake flow.
- The flow at high swirl number enhances the range and intensity of the vortices distribution, and produces a significant reverse flow in the combustion chamber.

6.2. Fuel droplet distribution in combustion chamber – Conclusions

From the simulation results of droplet distribution in the cold flow, it can be said that,

- The used of LES, DPM, Stochastics and TAB models can be used successfully to capture the droplet dispersion within the fluid structure based on validated experimental results
- The effects of equivalence ratio on droplet distribution is not significant when swirl number is the same.
- The fuel droplets in the flow with high swirl number disperses less in the streamwise direction, and the droplets on the downstream side have a higher

probability of getting sucked back into flowstream, which makes the spatial distribution of fuel droplets more concentrated at high swirl number.

- The flow with high swirl number produces smaller sizes of droplets, and makes the distribution of droplets size more concentrated.

6.3. Swirl-promoted turbulent combustion of emulsified canola oil – Conclusions

From the simulation results of swirl-promoted turbulent combustion of emulsified canola oil, it can be said that,

- The flow at high equivalence ratio is able to produce more small sized vortices in the combustion chamber when the swirl number is the same.
- The flow at low swirl number produces a strong interaction between the helical flow and wake flow, which leads to different sizes of vortices and reduces the size and intensity of the center recirculation zone.
- The helical flow and wake flow dominate the turbulent flow in the combustion chamber at high swirl number, which leads to a strong center recirculation zone in the combustion chamber.
- The turbulent kinetic energy in the combustion chamber depends on the temperature of chemical reaction when combustion takes place.
- The effect of equivalence ratio on the distribution of temperature is not significant at the same swirl number.
- The combustion at high swirl number produces an intense and concentrated high temperature region.

- The distribution of temperature highly depends on the distribution of fuel concentration.
- The combustion at high swirl number produces a great concentration of evaporated fuel in the vicinity of nozzle.
- The combustion under lean condition produces high turbulent intensity and greater dispersion of combustion on the downstream side when the swirl number is the same, which leads to lower *CO* emissions.
- The effects of swirl number on *CO* emissions is significant. *CO* emissions at high swirl number are reduced sharply due to the confinement of the combustion region by the center recirculation zone.
- The combustion under lean condition produces more NO_x emissions on the downstream side of the combustion chamber due to the high turbulent intensity in that region.
- The effects of swirl number on NO_x emissions is significant. NO_x emissions at high swirl number are reduced due to the confinement of the combustion region by the center recirculation zone.
- The simulation results show the same trends as the experimental work. The error associated with simulations increases when higher levels of turbulence intensity is considered.

7. FUTURE WORK

This study was attempted to simulate and identify the key features of swirl-promoted turbulent combustion when using emulsified canola oil as fuel. According to the findings from the simulation results, the effects of fuel viscosity and droplets size on the combustion characteristics should be studied further to understand the complex reaction mechanism that could lead to differences between simulation and experimental results. The following recommendations should be considered for further work in the near future:

1. Due to the lack of experimental of information regarding the size distribution of droplets generated by a twin-fluid atomizer, future simulations should consider a wide range of droplet size distributions, especially for droplets sizes below than *100* μm. Moreover, the applicability of direct droplet injection should be studied by comparing with an air-blasted atomizer.
2. In this study, one type of emulsified canola oil was considered. In order to understand the effect of fuel viscosity on the combustion characteristics, a conventional fuel should also be considered to understand the effects of fuel properties on combustion.
3. Since the simulation error can be considerable when the turbulent intensity is high, a complex reaction mechanism is needed to reduce the associated error between the simulation and the experiments.
4. This study found that the size of the center of the recirculation zone affects the combustion characteristics significantly. However, there is a lack of an appropriate

methodology to evaluate the size of the center of the recirculation zone. Therefore, an analytical based approach should be formulated to precisely predict the size of recirculation zone in a myriad of applications. Furthermore, different combustion chamber configurations should be considered that could enhance *CRZ*.

REFERENCES

[1]. IEA, *Key World Energy Statistics 2014*, Retrieved from http://www.iea.org/publications/freepublications/publication/keyworld2014.pdf, 2014.

[2]. J.G. Speight, K. Singh, Environmental management of energy from biofuels and biofeedstocks, 1st, Scrivener Publishing, Salem, Massachusetts, 2014.

[3]. G.S. Savant, J.L. Alvarado, K. Annamalai, and S. Capareda, Characterization and combustion performance of corn oil-based biofuel blends, *IMECE2012*, pp. 985-991, 2012.

[4]. S. Bhimani, J.L. Alvarado, Emission characteristics of methanol-in-canola oil emulsions in a combustion chamber, *Fuel*, vol. 113, pp. 97-106, 2013.

[5]. H.K. Nayak, Experimental study of combustion of soybean oil in a diesel engine, *International Journal of Advanced Research in Engineering and Applied Sciences*, vol. 1, No. 5, 2012.

[6]. R. Strayer, J. Blake, W. Craig, Canola and high erucic rapeseed oil as substitutes for diesel fuel: Preliminary tests, *Journal of the American Oil Chemists' Society*, vol. 60, pp. 1587-1592, 1983.

[7]. S.P. Krumdieck, J.W. Daily, Evaluating the feasibility of biomass pyrolysis oil for spray combustion applications, *Combustion Science and Technology*, vol. 134, pp. 351-365, 1998.

[8]. S. Nettles-Anderson, D.B. Olsen, J.J. Johnson, and J.N. Enjalbert, Performance of a direct injection IC engine on SVO and biodiesel from multiple feedstocks, *Journal of Power and Energy Engineering*, vol. 2, pp. 1-13, 2014.

[9]. R. Chellini, Fuel/water emulsion: A low NOx alternative to water or steam injection, 1990.

[10]. F. Chiariello, C. Allouis, F. Reale, and P. Massoli, Gaseous and particulate emissions of a micro gas turbine fuelled by straight vegetable oil–kerosene blends, *Experimental Thermal and Fluid Science*, vol. 56, pp. 16-22, 2014.

[11]. M. A. Al-Shudeifat and A.B. Donaldson, Combustion of waste trap grease oil in gas turbine generator, *Fuel*, vol. 89, pp. 549–53, 2010.

[12]. C.F. Kaminski, X.S. Bai, J. Hult, A. Dreizler, L. Fuchs, Flame growth and wrinkling in a turbulent flow, *Applied Physics B (Lasers and Optics)*, vol. 71, pp. 711–716, 2000.

[13]. C.F. Kaminski, J. Hult, M. Aldén, et al. Spark ignition of turbulent methane/air mixtures revealed by time-resolved planar laser-induced fluorescence and direct numerical simulations, *Proceedings of the Combustion Institute*, vol. 28, pp. 399–405, 2000.

[14]. J. Hult, G. Josefsson, M. Aldén, C.F. Kaminski, Flame front tracking and simultaneous flow field visualization in turbulent combustion, *Proceedings of the 10th International Symposium on Applications of Laser Techniques to Fluid Mechanics*, No. 26-2, Lisbon, 2000.

[15]. Y.C. Chen, S.M. Mohy, Simultaneous Rayleigh scattering and laser induced CH fluorescence for reaction zone imaging in high-speed premixed hydrocarbon flames, *Applied Physics B*, vol. 64, pp. 599–605, 1997.

[16]. A. Cavarzere, M. Morini, M. Pinelli, P. R. Spina, A. Vaccari, and M. Venturini, Experimental analysis of a micro gas turbine fuelled with vegetable oils from energy crops, *Energy Procedia*, vol. 45, pp. 91-100, 2014.

[17]. Y. Huang, V. Yang, Dynamics and stability of lean-premixed swirl-stabilized combustion, *Progress in Energy and Combustion Science*, vol. 35, pp. 293-364, 2009.

[18]. W.P. Jones, B.E. Launder, The prediction of laminarization with a two-equation model of turbulence, *Int. J. of Heat and Mass Transfer*, vol. 15, pp. 301–314, 1972.

[19]. B.E. Launder, B.L. Sharma, Application of the energy dissipation model of turbulence to the calculation of flow near a spinning disc, *Letters in Heat and Mass Transfer*, vol. 1, no. 2, pp. 131–138, 1974.

[20]. R.S. Amano, Turbulence effect on the impinging jet on a flat plate, *Bull JSME*, vol. 26 (221), pp. 1891–1899, 1983.

[21]. K.K. Zin, A. Hansske, F. Ziegler, Modeling and optimization of the vortex tube with computational fluid dynamic analysis, *Energy Research Journal*, vol. 1 (2), pp. 193-196, 2010.

[22]. P. Moin, K. Mahesh, Direct numerical simulation: a tool in turbulence research, *Annu. Rev. Fluid Mech.*, vol. 30, pp. 539-578, 1998.

[23]. K. Luo, H. Pitsch, M.G. Pai, O. Desjardins, Direct numerical simulations and analysis of three-dimensional n-heptane spray flames in a model swirl combustor, *Proceedings of the Combustion Institute*, vol. 33, pp. 2143–2152, 2011.

[24]. S. Tanaka, M. Shimura, N. Fukushima, M. Tanahashi, and T. Miyauchi, DNS of turbulent swirling premixed flame in a micro gas turbine combustor, *Proceedings of the Combustion Institute*, vol. 33, pp. 3293–3300, 2011.

[25]. S. Pope, Turbulent Flows 1st edition. Cambridge University Press, Cambridge, UK, 2000.

[26]. Y. Huang and V. Yang, Dynamics and stability of lean-premixed swirl-stabilized combustion, *Progress in Energy and Combustion Science*, vol. 35, pp. 293-364, 2009.

[27]. S. Wang, V. Yang, G. Hsiao, S Hsieh, et al., Large-eddy simulations of gas-turbine swirl injector flow dynamics, *J. Fluid Mech.*, vol. 583, pp. 99–122, 2007.

[28]. S. Wang, S.Y. Hsieh, and V. Yang, Unsteady flow evolution in swirl injector with radial entry. I. Stationary conditions, *Physical of Fluid*, vol. 17, 045106, 2005.

[29]. W.W. Kim, S. Menon, and J.A. Miller, Large eddy simulation of a gas turbine combustor flow, *Combustion Science and Technology*, vol.143, pp.25-62, 1999.

[30]. F.F. Grinstein, T.R. Yong, G. Li, E.J. Gutmark, G. Hsiao, and H.C. Mongia, Computational and experimental analysis of the flow dynamics in a multi-swirler combustor, *AIAA Paper*, 2002-1006, 2002.

[31]. X. Lu, S. Wang, H. Sung, et al., Large-eddy simulations of turbulent swirling flows injected into a dump chamber, *J. Fluid Mech.*, vol. 527, pp. 171–195, 2005.

[32]. Y. Huang, H. Sung, S. Hsieh, et al., Large eddy simulation of combustion dynamics of lean-premixed swirl-stabilized combustor, *Journal of Propulsion and Power*, vol. 19, No. 5, September–October, 2003.

[33]. M. Wu, Y. Wang, V. Yang, and R.A. Yetter, Combustion in meso-scale vortex chambers, *Proceedings of the Combustion Institute*, vol. 31, pp. 3235–3242, 2007.

[34]. C. Stone and S. Menon, Swirl control of combustion instabilities in a gas turbine combustor. *Proceedings of the Combustion Institute*, vol. 29, pp. 155–60, 2002.

[35]. C. Stone and S. Menon, Open-loop control of combustion instabilities in a model gas turbine combustor. *Journal of Turbulence*, vol. 4, No. 020, 2003.

[36]. V. Yang, W. Anderson, Liquid Rocket Engine Combustion Instability, *Progress in Astronautics and Aeronautics*, vol. 169, American Institue of Aeronautics and Astronautics, Inc., Washington, DC., 1995.

[37]. H.F. Liu, X. Gong, W.F. Li, F.C Wang, Z.H. Yu, Prediction of droplet size distribution in sprays of prefilming air-blast atomizers, *Chem. Eng. Sci.*, vol. 61, pp. 1741–1747, 2006.

[38]. W. Xu, H Jin, K. Sun, and J. Fan, Numerical investigation of droplet evaporation and transport in a turbulent spray with LES/VSJFDF model, *Chemical Engineering Science*, vol. 119, pp. 251-260, 2014.

[39]. S.V. Apte, M. Gorokhovski, P. Moin, Les of atomizing spray with stochastic modeling of secondary breakup, *Int. J. Multiphase Flow*, vol. 29, pp. 1503–1522, 2003.

[40]. V. Sankaran and S. Menon, LES of spray combustion in swirling flows, *Journal of Turbulence*, vol. 3, No, 011, 2002.

[41]. V. Sankaran and S. Menon, Vorticity-scalar alignments, and small-scale structures in swirling spray combustion, *Proceedings of the Combustion Institute*, vol. 29, pp. 577–84, 2002.

[42]. W.P. Jones, S. Lyra, S. Navarro-Martinez, Large eddy simulation of turbulent confined highly swirling annular flows, *Flow Turbulence Combust*, vol. 89, pp. 361–384, 2012.

[43]. W.P. Jones, S. Lyra, S. Navarro-Martinez, Numerical investigation of swirling kerosene spray flames using Large Eddy Simulation, *Combustion and Flame*, vol. 159, pp. 1539–1561, 2012.

[44]. M. Salewski and L. Fuchs, Dispersion of circular, non-circular, and swirling spray jets in crossflow, *Direct and Large-Eddy Simulation VI*, vol. 10, pp. 319-328, 2006.

[45]. W.P. Jones, A.J. Marquid, K. Vogiatzaki, Large-eddy simulation of spray combustion in a gas tubine combustor, *Combustion and Flame*, vol. 161, pp. 222-239, 2014.

[46]. L. Zhou, K.H. Luo, W. Qin, M. Jia, S.J. Shuai, Large eddy simulation of spray and combustion characteristics with realistic chemistry and high-order numerical scheme under diesel engine-like conditions, *Energy Conversion and Management*, vol. 93, pp. 377-387, 2015.

[47]. V. Sankaran and S. Menon, LES of spray combustion in swirling flows, *Journal of Turbulence*, vol. 3, No, 011, 2002.

[48]. W. Yuan, A.C. Hansen, Q. Zhang, Predicting the physical properties of biodiesel for combustion model, *Transactions of the ASAE*, vol. 46, pp. 1487-1493, 2003.

[49]. R. Ceriania, R. Gania, A.J.A. Meirellesb, Prediction of heat capacities and heats of vaporization of organic liquids by group contribution methods, *Fluid Phase Equilibria*, vol. 283, pp. 49-55, 2009.

[50]. P. Benjumea, J. Agudelo, A. Agudelo, Basic properties of palm oil biodiesel–diesel blends, *Fuel*, vol. 87, pp. 2069–2075, 2008.

[51]. C.K. Westbrook, Simplified reaction mechanisms for the oxidation of hydrocarbon fuels in flames, *Combustion Science and Technology*, vol. 27, pp. 31-43, 1981.

[52]. W. Yuan, A.C. Hansen, M.E. Tat, J.H. Van Gerpen, Z. Tan, Spray, ignition, and combustion modeling of biodiesel fuels for investigating NOx emissions, *Transactions of the ASAE*, vol. 48, pp. 933-939, 2005.

[53]. C.K. Westbrook and F.L. Dryer, Chemical kinetic modeling of hydrocarbon combustion, *Progress in Energy and Combustion Science*, vol. 10, pp. 1-57, 1984.

[54]. M.F. Yasina, R.S. Cant, C.T. Chong, S. Hochgreb, Discrete multicomponent model for biodiesel spray combustion simulation, *Fuel*, vol. 126, pp. 44-54, 2014.

[55]. A. Irannejad, A. Banaeizadeh, F. Jaberi, Large eddy simulation of turbulent spray combustion, *Combustion and Flame*, vol. 162, pp. 431-450, 2015.

[56]. S. Bhimani, Experimental characterization of canola oil emulsion combustion in a modified furnace, M.S. Thesis, Texas A&M University, College Station, 2011.

[57]. J.M. Beer, N.A. Chigier, Combustion Aerodynamics, John Wiley and Sons Inc, New York City, New York, 1972.

[58]. Canola Oil with Omega-3 DHA, http://www.crisco.com/products/canola-oil-with-omega-3-dha-15-801.

[59]. Physical Properties of Pure Methanol, http://www.methanol.org/Technical-Information/Resources/Technical-Information/Physical-Properties-of-Pure-Methanol.aspx.

[60]. R.C. Reid, J.M. Prausnitz, T.K. Sherwood, The properties of gases and liquids. 4th ed., McGraw-Hill, New York City, New York, 1987.

[61]. T. Ahmed, Hydrocarbon phase behavior, *Gulf Publishing Company*, Houston, Texas, 1989.

[62]. Ansys Inc, ANSYS Fluent Theory Guide, Release 15.0, 2013.

[63]. S.A. Morsi and A.J. Alexander. An Investigation of Particle Trajectories in Two-Phase Flow Systems, *J. Fluid Mech.*, vol. 55, pp. 193–208, 1972.

[64]. B.F. Magnussen and B.H. Hjertager. On mathematical models of turbulent combustion with special emphasis on soot formation and combustion, *16th Symp. (Int'l.) on Combustion*, 1976.

[65]. J.W. Cooley and J. W. Tukey, An algorithm for the machine computation of the complex fourier series, *Mathematics of Computation*, vol. 19, pp. 297-301, 1965.

[66]. W.P. Jones and D.H. Sheen, A probability density function method for modelling liquid fuel sprays, *Flow, Turbulence and Combustion*, vol. 63, pp. 379-394, 1999.

[67]. M. Wessman, Laser Doppler measurements of turbulent swirling flows in a circular tube with a sudden expansion followed by a sudden contraction, Licentiate thesis, Lund University, Sweden, Report ISRN LUTMDN/TMVK-7018-SE, 1995.

[68]. S.C. Favaloro, Experimental and computational investigation of isothermal swirling flow in an axisymmetric dump combustor, *J. Propulsion*, vol. 7, No. 3, 1989.

[69]. K.P. Judd, Z. Rusak, and A. Hirsa, Theoretical and experimental studies of swirling flows in diverging streamtubes, *Advances in Fluid Mechanics III, WIT press*, pp. 491-502, 2000.

[70]. P. Chakraborty, S. Balachandar, and R.J. Adrian, on the relationships between local vortex identification schemes, *J. Fluid Mech.*, vol. 535, pp. 189–214, 2005.

[71]. P. Billant, J.M. Chomaz, and P. Huerre, Experimental study of vortex breakdown in swirling jets, *J. Fluid Mech.*, vol. 376, pp. 183-219, 1998.

[72]. H. Liang and T. Maxworthy, An experimental investigation of swirling jets, *J. Fluid Mech.*, vol. 525, pp. 115-159, 2005.

[73]. V. Sankaran and S. Memon, LES of spray combustion in swirling flows, *Journal of Turbulence*, vol. 3, pp. 11-23, 2002.

[74]. V. Babrauskas, Temperature in flames and fires, *Fire Science and Technology Inc,* February 25, 2006.

[75]. A.K. Gupta, M.J. Lewis, and S. Qi, Effect of swirl on combustion characteristics of premixed flames, *J. Eng. Gas Turbine and Power*, vol. 120, pp. 488-494, 1998.

APPENDIX A

The following equation represents the stoichiometric combustion reaction equation of emulsified canola oil as shown in Table 3.

$$CH_{1.704}O_{0.128} + a\times(O_2 + 3.76N_2) \rightarrow CO_2 + b\times(H_2O) + c\times N_2$$

After balancing the stoichiometric combustion equation on both sides of the equation, the value of stoichiometric coefficients are as shown in Table A-1.

Table A-1. Stoichiometric coefficients for complete combustion of emulsified canola oil

Stoichiometric coefficient	Value
a	1.362
b	0.852
c	5.12112

Using the stoichiometric coefficients in Table A, the molar fraction of CO_2 for complete combustion of emulsified canola oil can be obtained as follows:

$$\chi_{CO_2} = \frac{1}{1+b+c} = \frac{1}{1+0.852+5.12112} = 0.14$$

Therefore, the molar fraction of CO_2 for complete combustion of emulsified canola oil is 14%.

Fig. A-1 (a)-(d) show the simulation results of molar fraction of CO_2 at the axial location (*z/H*) of *0.38*, *1*, and *4* at *60* ms for *SN* of *1.0* and ϕ of *0.81*, *SN* of *1.0* and ϕ of *0.97*, *SN* of *1.4* and ϕ of *0.81*, and *SN* of *1.4* and ϕ of *0.97*, respectively.

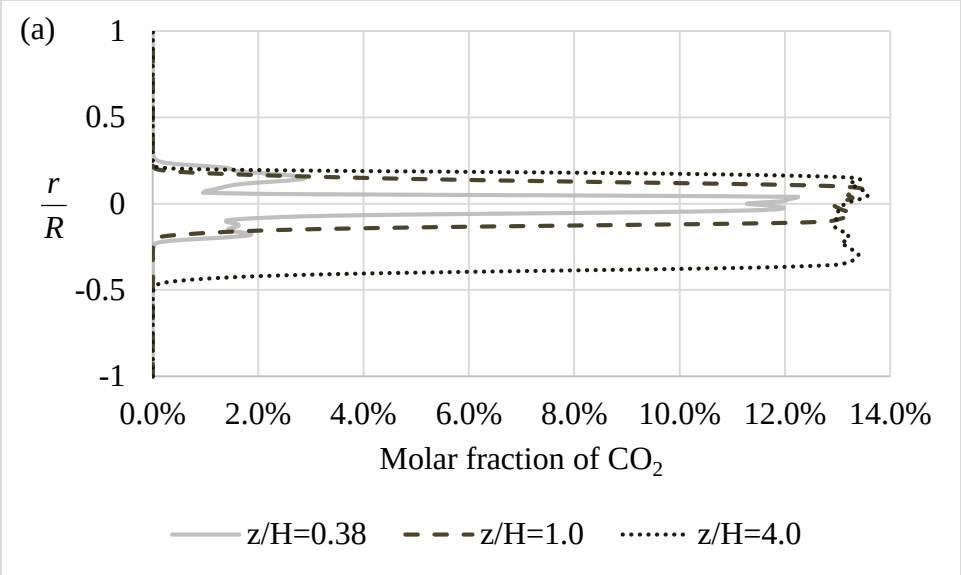
(a)
1
0.5
0
-0.5
-1
r/R
0.0% 2.0% 4.0% 6.0% 8.0% 10.0% 12.0% 14.0%
Molar fraction of CO2
z/H=0.38
z/H=1.0
z/H=4.0

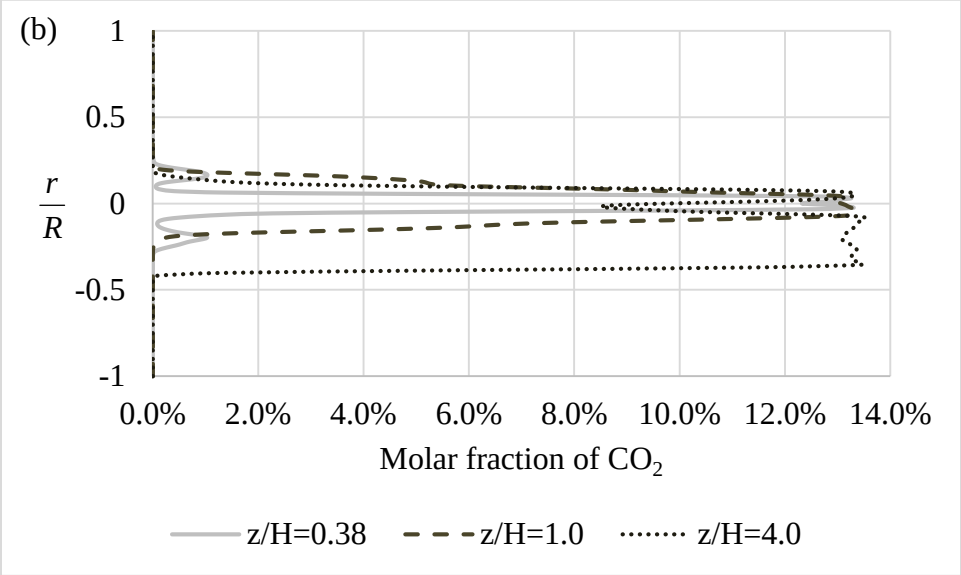
(b)
1
0.5
0
-0.5
-1
r/R
0.0% 2.0% 4.0% 6.0% 8.0% 10.0% 12.0% 14.0%
Molar fraction of CO2
z/H=0.38
z/H=1.0
z/H=4.0

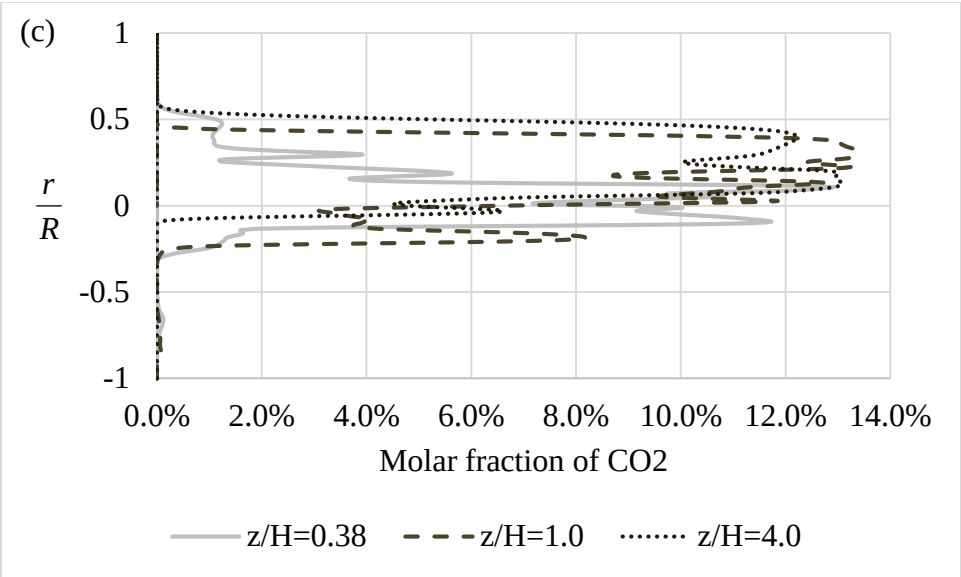

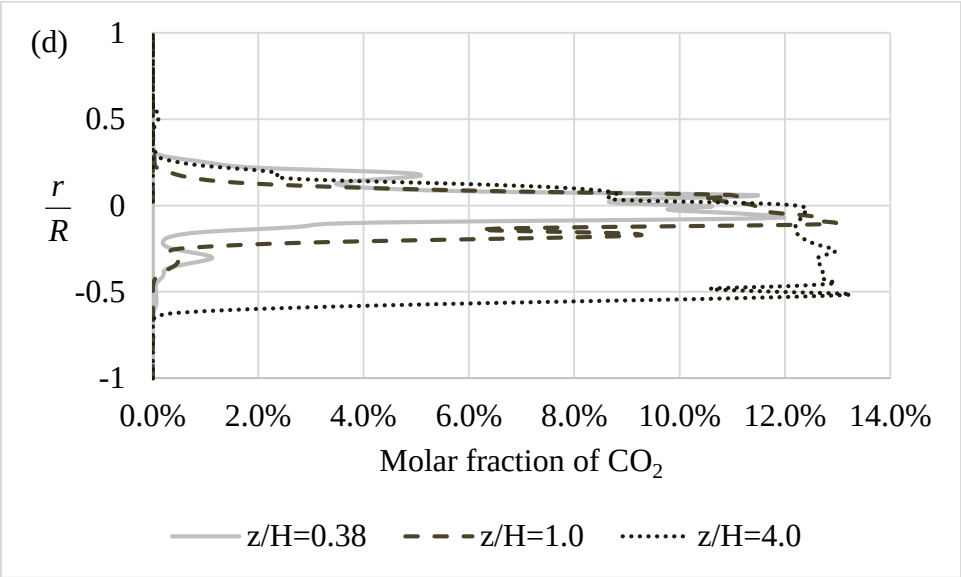

Fig. A-1. Simulation results of molar fraction of CO_2 at the axial location (*z/H*) of *0.38*, *1*, and *4* at *60* ms (a) *SN* of *1.0* and ϕ of *0.81*, (b) *SN* of *1.0* and ϕ of *0.97*, (c) *SN* of *1.4* and ϕ of *0.81*, and (d) *SN* of *1.4* and ϕ of *0.97*

As shown in Fig. A-1 (a)-(d), the simulation results of molar fraction of CO_2 are a little smaller than the value of *14%*. As shown in Table 4, a two-step chemical

reaction mechanism was used for this study. It considered the reaction from CO_2 to CO, which leads to a reduction of CO_2 in the simulation. However, Fig. A-1 (a)-(d) show that the CO_2 concentration or molar fraction reaches the values corresponding to complete combustion (14%) after *60* ms of simulation time. Therefore, a simulation time of *60* ms was long enough to ensure complete combustion.